Nuclear Magnetic Resonance Methods for Characterization of Mass Transport in Porous Materials

Dissertation

zur Erlangung des Doktorgrades der Naturwissenschaften
- Doctor rerum naturalium -

vorgelegt
dem Fachbereich 02 (Biologie/Chemie)
der Universität Bremen

von
Herrn Li Huang, Master of Science,
geboren am 22. September 1988 in Guangdong, China

Bremen, 2017

Gutachter/-innen:

Herr Priv.-Doz. Dr. Wolfgang Dreher
Universität Bremen

Herr Prof. Dr. Matthias Günther
Fraunhofer-Institut für Bildgestützte Medizin MEVIS

Weitere Mitglieder der Prüfungskommission:

Herr Prof. Dr. Marcus Bäumer
Universität Bremen

Herr Prof. Dr. Peter Spiteller
Universität Bremen

Herr Dr. Peter Erhard
Universität Bremen

Frau Marilena Hnida
Universität Bremen

Promotionskolloquium am 17. August 2017

Erklärung:
Hiermit erkläre ich, dass ich die vorliegende Dissertation selbstständig angefertigt und nur die angegebenen Quellen und Hilfsmittel verwendet habe. Diese Dissertation wurde nicht vorher an anderer Stelle eingereicht.

Zusammenfassung

Messverfahren der räumlich aufgelösten kernmagnetischen Resonanz (NMR, "*Nuclear Magnetic Resonance*") bzw. der NMR-Bildgebung (MRI, "*Magnetic Resonance Imaging*") ermöglichen die Messung von Transportprozessen, die z.B. bei Trocknungs- oder Flussprozessen in opaken porösen Materialien von Bedeutung sind. Solche NMR-Messverfahren können eine wichtige Rolle zum besseren Verständnis der Mechanismen spielen, die diesen dynamischen Prozessen zugrunde liegen und dadurch zur Verbesserung des Designs heterogener Systeme beitragen. Derartige Anwendungen ortsaufgelöster NMR-Messverfahren werden jedoch durch nicht-vernachlässigbare Magnetfeldinhomogenitäten in porösen Strukturen, den schnellen Abfall der transversalen Magnetisierung durch Relaxationsprozesse, die Forderung nach hoher räumlicher und angemessener zeitlicher Auflösung sowie anwendungsspezifische Nachteile wie z.B. die geringe NMR-Empfindlichkeit bei Messungen von Gasen erschwert. In der vorliegenden Arbeit wurden räumlich aufgelöste NMR-Messverfahren verbessert und optimiert, um diese Einschränkungen insbesondere in Studien von Trocknungsprozessen, Geschwindigkeitsmessungen langsam fließender Flüssigkeiten sowie fließender Gase in porösen Materialen zu reduzieren.

Für die Messung von Trocknungsprozessen wurde ein MRI-Verfahren mit ultrakurzer Echozeit eingesetzt, welches den dominierenden Spindichte-Kontrast und die vernachlässigbare transversale Relaxation ausnutzt. Die Untersuchung der beobachteten wellenartigen Bildartefakte ergab, dass diese durch unerwünschte Hintergrundsignale verwendeter Hardwarekomponenten, insbesondere der Hochfrequenzspule (HF-Spule), verursacht wurden. Eine wirkungsvolle Unterdrückung dieser Hintergrundsignale wurde sowohl durch den Einsatz von Sättigungsschichten als Präparation der Magnetisierung vor der Signalanregung als auch durch optimierte HF-Spulen aus ^1H-freiem Material erreicht.

Für die Messung der Geschwindigkeit langsam fließender Flüssigkeiten, insbesondere für Studien zur Tiefenfiltration, wurde ein optimiertes Multiecho-MRI-Messverfahren zur Beschleunigung der Messung vorgeschlagen, um eine

schnelle und genaue Messung der Geschwindigkeitsfelder in porösen Materialen zu ermöglichen. Dazu wurde eine dedizierte HF-Spule mit hohem Füllfaktor unter Beachtung der geometrischen Einschränkungen beim Betrieb einer vertikalen Filtrationszelle in einem Magneten mit horizontaler Bohrung entwickelt, wenngleich bei dieser HF-Spule die räumlichen Inhomogenitäten der HF-Felder nicht vernachlässigbar sind. Durch verschiedene Modifikationen der NMR-Pulssequenz sowie der Programme zur Datenverarbeitung und -analyse gelang es, systematische Fehler bei der Messung der Geschwindigkeitsfelder zu minimieren. Dies wurde insbesondere durch Korrekturen von Offsets, die durch nicht-perfekte Hardwarekomponenten verursacht werden, sowie die Kombination von ungeraden und geraden Echos im beschleunigten Akquisitionsschema erreicht.

Messungen an thermisch polarisierten, fließenden Gasen weisen den Nachteil einer geringen NMR-Empfindlichkeit infolge geringer Spindichte, schneller transversaler Relaxation und starker molekularer Diffusion auf. Daher wurden standardisierte Verfahren zur Optimierung des Messprotokolls für räumlich aufgelöste Geschwindigkeitsmessungen an Gasen vorgeschlagen (Kompromiss zwischen Messparametern und Einsatz eines geeigneten Phasenzyklus), um ein optimales Signal-zu-Rausch-Verhältnis zu erreichen. Dieses Vorgehen wurde durch Experimente an Methan in einem Gasreaktor validiert.

Die vorgeschlagenen Methoden, durch welche NMR-Bilder mit einem gewünschten Kontrast, insbesondere Spindichte oder Geschwindigkeit, gemessen werden können, werden verbesserte quantitative Untersuchungen des Massentransports in porösen Materialien ermöglichen und auch für andere Anwendungsgebiete von Interesse sein.

Abstract

Spatially resolved *Nuclear Magnetic Resonance* (NMR) or *Magnetic Resonance Imaging* (MRI) techniques can measure the mass transport processes including drying and flow in opaque porous materials, and thus may play an important role in better understanding the mechanisms underlying the corresponding dynamic processes. This might help improving the designs of heterogeneous systems. However, these applications are challenging due to the non-negligible magnetic field inhomogeneities in porous structures, the significant signal decay by transversal relaxation of magnetization, the demand for high spatial resolution and adequate temporal resolution, as well as additional drawbacks in specific applications like low NMR sensitivity in gas measurements. In this work, spatially resolved NMR methods were improved and optimized to mitigate these limitations for studies on drying, slow liquid flow, and gas flow in porous materials.

For drying studies, MRI with an ultrashort echo time was used exploiting its predominant spin density contrast and negligible signal decay by transversal relaxation of magnetization. Investigations on associated wave-pattern image artifacts indicated that these artifacts originate from background signals of NMR hardware, mainly the radio-frequency coil. An efficient suppression of such background signals was achieved by saturating slices in the outer volume for magnetization preparation as well as using an optimized coil made of ^1H-free material.

For slow liquid flow studies, particularly studies on deep bed filtration, an optimized spatially resolved NMR velocimetry method using multiple echoes for accelerating the measurement was proposed to achieve fast and accurate velocity mapping in porous materials. A dedicated coil with a high filling factor was constructed considering the limited space available for a vertical filtration cell in a horizontal NMR scanner, however, introducing non-negligible inhomogeneity of the radio-frequency magnetic field. Several modifications of the NMR pulse sequence and the data post-processing procedures were applied for suppressing systematic errors in the measured velocity fields, particularly correcting offsets due to hardware imperfection as well as combining

signals of odd and even echoes in the accelerated acquisition scheme.

Studies on thermally polarized gas flow exhibit the drawback of low NMR sensitivity due to low spin density, rapid transversal relaxation, and strong molecular diffusion. Therefore, standardized procedures for the adjustment of the measurement protocol, including finding a compromise between measurement parameters and employing an appropriate phase cycling scheme, were proposed to achieve an optimal signal-to-noise ratio in spatially resolved NMR velocimetry of gas flow. These procedures were validated in experiments on methane in a gas reactor.

The proposed methods, by which NMR images with a desired image contrast like spin density or velocity can be obtained, will support quantitative research on mass transport in porous materials and are also of interest for further applications.

Lebenslauf und Publikationsliste

Persönliche Daten

Name	Huang, Li
geboren	am 22. September 1988 in Guangdong, China

Bildungsweg

September 1994 - Juli 2006	Schulbildung (Oberschulabschluss) Huizhou, China
September 2006 - Juli 2011	Bachelorstudium der Physik (B.Sc.) Fakultät für Physikalische Wissenschaften Universität für Wissenschaft und Technik Chinas Hefei, China
Oktober 2011 - September 2013	Masterstudium der Physik (M.Sc.) Physikalisch-Astronomische Fakultät Friedrich-Schiller-Universität Jena Jena, Deutschland
Juni 2014 - Mai 2017	Promotionsstudium der Naturwissenschaften Fachbereich 02 (Biologie/Chemie) Universität Bremen Bremen, Deutschland

Berufserfahrung

Oktober 2013 - September 2016	Wissenschaftlicher Mitarbeiter DFG-Graduiertenkolleg MIMENIMA (GRK 1860) Fachbereich 02 (Biologie/Chemie) Universität Bremen Bremen, Deutschland
Oktober 2016 - Mai 2017	Gastwissenschaftler für Abschluss der Doktorarbeit Fachbereich 02 (Biologie/Chemie) Universität Bremen Bremen, Deutschland

Wissenschaftliche Veröffentlichungen

1. Wolfgang Dreher, Ingo Bardenhagen, Li Huang, and Marcus Bäumer. On the suppression of background signals originating from NMR hardware components. Application to zero echo time imaging and relaxation time analysis. *Magn. Reson. Imaging*, 34(3):264-270, 2016.

2. Li Huang and Wolfgang Dreher. Characterizing macroscopic mass transport in porous media by zero echo time MRI. In *Proceedings of 13th International Conference on Magnetic Resonance Microscopy: Materials, Molecular Processes and Engineering*, Munich, Germany, 2nd - 6th August 2015. P097.

3. Li Huang, Gerd Mikolajczyk, Ekkehard Küstermann, Michaela Wilhelm, Stefan Odenbach, and Wolfgang Dreher. Adapted MR velocimetry of slow liquid flow in porous media. *J. Magn. Reson.*, 276:103-112, 2017.

Contents

List of Figures

List of Tables

Preface

With the topic approved in June 2014 by the Dissertation Board of Faculty 02 (Biology/Chemistry), University of Bremen, this doctoral thesis entitled "Nuclear magnetic resonance methods for characterization of mass transport in porous materials" is a contribution describing my work from October 2013 to May 2017 within a research project of the same title (funded by the German Research Foundation from October 2013 to September 2016). The project aims at methodological improvements and optimization on spatially resolved *Nuclear Magnetic Resonance* (NMR) for characterizing the mass transport processes including drying and flow in opaque porous materials.

The project is divided into three subprojects, and the corresponding structure of the thesis is as follows:

1. Chapter 1 is the general introduction of the thesis, containing principles of NMR techniques, general challenges for studies on porous materials by spatially resolved NMR, and NMR facilities used in this work.

2. Described in Chapter 2, the first subproject for imaging drying in porous materials focuses on suppressing image artifacts originating from background signals of NMR hardware.

3. Summarized in Chapter 3, the second and the major subproject for measuring slow liquid flow in porous materials concentrates on developing fast and accurate velocimetry by NMR tolerant to magnetic field inhomogeneities.

4. Demonstrated in Chapter 4, the third and the last subproject for measuring gas flow in porous materials focuses on optimizing the signal-to-noise ratio in velocimetry by NMR.

5. Chapter 5 is the general conclusion of the thesis.

Chapter 1

General Introduction

1.1 Fundamentals of NMR

The NMR effect can be described by concepts of quantum physics, but many aspects of NMR can be conveniently considered in classical electromagnetic physics. The NMR phenomenon occurs in the case that certain atomic nuclei in a static magnetic field are radiated by an oscillating magnetic field. This section introduces briefly the fundamentals of NMR. Further detailed descriptions can be found in many NMR textbooks, *e.g.* [1, 2, 3, 4].

1.1.1 Nuclear Spin and Magnetic Moment

As an intrinsic basic property of elementary and composite particles, the *spin* exists with either positive or negative polarity, and can be described by a *spin quantum number*, which is an integer multiple of $\frac{1}{2}$. Every individual unpaired proton, neutron, and electron has a spin quantum number of $\frac{1}{2}$. An atomic nucleus has then a nuclear spin quantum number I determined by the coupling between the compositing protons and neutrons, and thus such a *nuclear spin* has an *angular momentum* $\boldsymbol{L}$ with the magnitude given by

$$L = \sqrt{I(I+1)}\hbar \tag{1.1}$$

with the *reduced Planck constant* $\hbar = 6.5821 \cdot 10^{-16}\, eV \cdot s$ and $I = 0, \frac{1}{2}, 1, \frac{3}{2}, \cdots$.

In a static magnetic field $\boldsymbol{B}_0$, which is often defined in the z-direction without losing generality, the nuclear spin has a preferred direction along the z-axis due to the torque exerted by $\boldsymbol{B}_0$, which causes *Larmor precession* of the nuclear spin about the z-axis. The nuclear spin has then a *magnetic moment* $\boldsymbol{\mu}$ defined by

$$\boldsymbol{\mu} = \gamma \boldsymbol{L} \tag{1.2}$$

with the *gyromagnetic ratio* γ, which is specific for each nucleus. The Larmor precession of the angular momentum $\boldsymbol{L}$ can be described by

$$\frac{d\boldsymbol{L}}{dt} = \boldsymbol{\mu} \times \boldsymbol{B}_0. \tag{1.3}$$

By substituting Equation 1.2 into 1.3, the Larmor precession of the magnetic moment can then be described by

$$\frac{d\boldsymbol{\mu}}{dt} = \gamma\boldsymbol{\mu} \times \boldsymbol{B}_0 = \boldsymbol{\mu} \times \boldsymbol{\omega}_0 \tag{1.4}$$

with the *angular resonance frequency* ω_0 given by

$$\omega_0 = \gamma B_0, \tag{1.5}$$

and is illustrated in Figure 1.1.

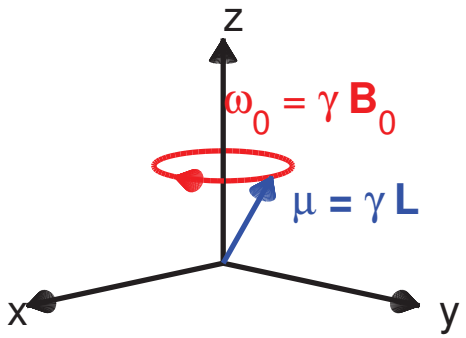

Figure 1.1: Larmor precession (red curve) of the magnetic moment $\boldsymbol{\mu}$ (blue vector) along $\boldsymbol{B}_0$ (parallel to the z-axis) with the angular resonance frequency ω_0 proportional to B_0.

L_z as the *azimuthal angular momentum* of a nuclear spin is given by

$$L_z = m\hbar \tag{1.6}$$

with a *magnetic quantum number* $m = -I, -I+1, \cdots, I-1, I$. This nuclear spin has an *azimuthal magnetic moment* μ_z defined by

$$\mu_z = \gamma L_z. \tag{1.7}$$

According to Equation 1.6 and 1.7, the nuclear spin's *magnetic energy* E is given by

$$E = -\boldsymbol{\mu} \cdot \boldsymbol{B}_0 = -\mu_z B_0 = -\gamma m\hbar B_0. \tag{1.8}$$

For simplicity, the following descriptions of the NMR effect focuses on the ^1H nucleus with one single proton, which is most widely used in NMR studies and was used in this work. A ^1H nucleus has a nuclear spin quantum number $I = \frac{1}{2}$ and only two possible azimuthal magnetic quantum numbers $m = \pm\frac{1}{2}$. Hence, it can be regarded as a simple two-energy-level system with the energy difference

$$\Delta E = \gamma \hbar B_0. \tag{1.9}$$

Transition between two energy levels can occur when the ^1H nucleus is radiated by photons, which have the *resonance frequency* ν_0 given by

$$\nu_0 = \frac{\Delta E}{2\pi\hbar} = \frac{\gamma}{2\pi} B_0 = \frac{\omega_0}{2\pi}. \tag{1.10}$$

For the ^1H nucleus, $\frac{\gamma}{2\pi} = 42.577\, MHz/T$. The NMR effect is a physical phenomenon, in which nuclear spins polarized by a static magnetic field $\boldsymbol{B}_0$ absorb and re-emit photons when radiated by an oscillating magnetic field $\boldsymbol{B}_1$ near the resonance frequency.

1.1.2 Magnetization

Under the thermal equilibrium of the nuclear spin polarization, the spin populations of these two energy levels N_- ($m = -\frac{1}{2}$, higher energy level) and N_+ ($m = \frac{1}{2}$, lower energy level) satisfy the *Maxwell-Boltzmann distribution*

$$\frac{N_-}{N_+} = e^{-\frac{\Delta E}{k_B T}} = e^{-\frac{\gamma\hbar B_0}{k_B T}} = e^{-\frac{h\nu_0}{k_B T}} \tag{1.11}$$

with the *Boltzmann constant* $k_B = 8.6173 \cdot 10^{-5}\, eV/K$ and the temperature T. In most situations, $\gamma\hbar B_0 \ll k_B T$, then

$$\frac{N_-}{N_+} \simeq 1 - \frac{\gamma\hbar B_0}{k_B T}, \tag{1.12}$$

and the population difference $\Delta N_\pm$ can be given by

$$\Delta N_\pm = N_+ - N_- = N_+ \cdot (1 - \frac{N_-}{N_+}) \propto \frac{\gamma\hbar B_0}{k_B T}. \tag{1.13}$$

Nuclear spins in a certain spatial position establish a *macroscopic magnetization* $\boldsymbol{M}$ with its magnitude proportional to $\Delta N_\pm$. Note that according to Equation 1.2 and 1.13, the macroscopic magnetization under the thermal equilibrium $\boldsymbol{M}_0$ is in the z-direction (*i.e.* parallel to $\boldsymbol{B}_0$), and its magnitude can be described by

$$M_0 = \Delta N_\pm \cdot \mu \propto \frac{\hbar L}{k_B T} \gamma^2 B_0. \tag{1.14}$$

The NMR effect can be elaborated by the precession of the macroscopic magnetization, which is positioned in the static magnetic field $\boldsymbol{B}_0$ and exposed to the oscillating magnetic field $\boldsymbol{B}_1$ near the resonance frequency. The description of this precession is often more convenient in the rotating frame of reference (x'-, y'-, and z'-axes), which is rotating lefthandedly about the z-axis in the laboratory frame of reference (x-, y-, and z-axes) with the angular resonance frequency ω_0.

In this work, only pulsed $\boldsymbol{B}_1$ was used, just as in most NMR studies nowadays. As a result of a transversal $\boldsymbol{B}_1$ (*i.e.* in the xy- or $x'y'$-plane), the macroscopic magnetization will flip lefthandedly about a transversal axis along the $\boldsymbol{B}_1$ direction. The *Flip Angle* (FA) α is given by

$$\alpha = \gamma \int_{t_p} B_1(t) dt \tag{1.15}$$

with the pulse duration t_p, which ranges from microseconds to seconds and is typically milliseconds. Such excitation of macroscopic magnetization by $\boldsymbol{B}_1$ pulse in the laboratory frame and rotating frame of reference is illustrated in Figure 1.2.

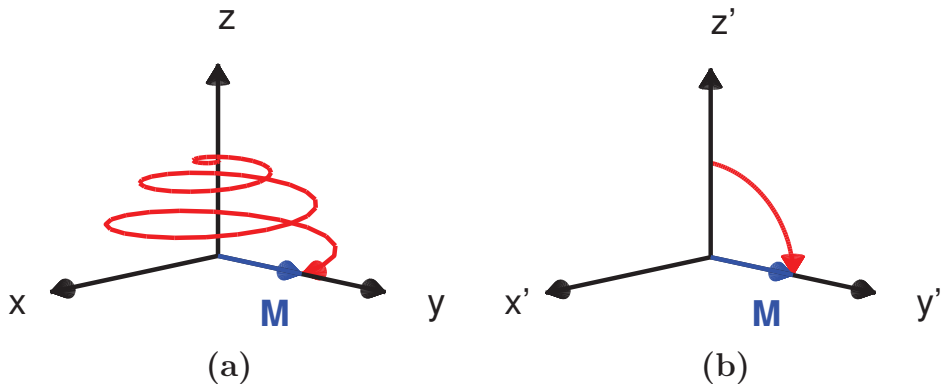

Figure 1.2: Macroscopic magnetization $\boldsymbol{M}$ (blue vector) excited by a $\boldsymbol{B}_1$ pulse ($\alpha = 90\,°$) in the laboratory frame (a) and rotating frame (b) of reference.

1.1.3 Bloch-Purcell Equation

In the rest of the thesis, nuclear spin and macroscopic magnetization are called *spin* and *magnetization* for short. As a vector sum of the magnetic moments of spins, the magnetization is described by the *Bloch-Purcell equation*

$$\frac{d\boldsymbol{M}}{dt} = \gamma \boldsymbol{M} \times \boldsymbol{B}_0 - \frac{\boldsymbol{M}_z - \boldsymbol{M}_0}{T_1} - \frac{\boldsymbol{M}_x + \boldsymbol{M}_y}{T_2}, \tag{1.16}$$

according to the Larmor precession and two additional relaxation mechanisms. The first relaxation is called *spin-lattice relaxation* with the characteristic time T_1, and represents energy transfer from spins to the surrounding lattice (usually condensed matter). The second relaxation is called *spin-spin relaxation* with the characteristic time T_2, and represents irreversible phase decoherence due to fluctuating microscopic magnetic fields in molecular interactions. According to Equation 1.16, the longitudinal component of the magnetization M_z can be described by

$$M_z(t) = M_z(0)e^{-t/T_1} + M_0(1 - e^{-t/T_1}), \tag{1.17}$$

and the transversal component of the magnetization M_{xy} as

$$M_{xy} = M_x + i \cdot M_y \tag{1.18}$$

can be described by

$$M_{xy}(t) = M_{xy}(0)e^{-t/T_2 - i2\pi\nu_0 t}. \tag{1.19}$$

T_1 relaxation of M_z and T_2 relaxation of M_{xy} are illustrated in Figure 1.3. The spin-lattice relaxation is not faster than the spin-spin relaxation, and thus $T_1 \geqslant T_2$. Typically T_1 and T_2 of different matter range from milliseconds to seconds, and are B_0-dependent in different ways.

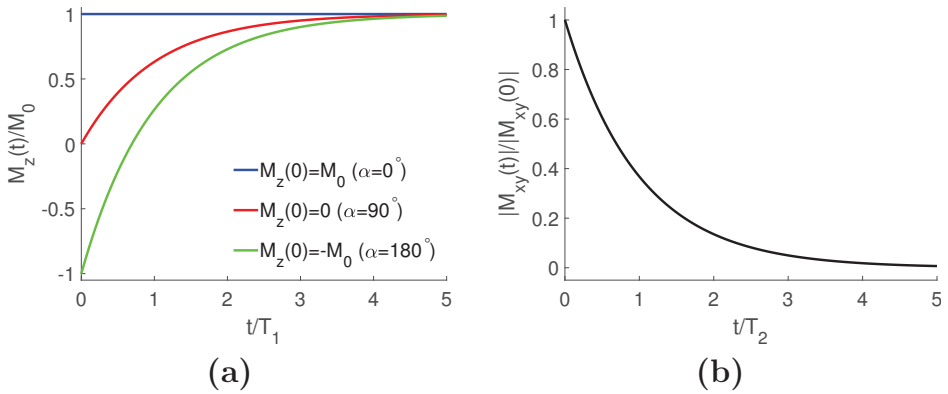

Figure 1.3: Relaxation of magnetization. (a) T_1 relaxation of M_z (*cf.* Equation 1.17). (b) T_2 relaxation of M_{xy} (*cf.* Equation 1.19).

1.1.4 NMR Signals

NMR signals can be received by detecting the voltages induced by the transversal component of the precessing magnetization M_{xy} into a resonator (coil),

e.g. as a *Free Induction Decay* (FID) after an *excitation pulse*. T_1 and T_2 spectra of the magnetization can be characterized by single- and multi-component exponential fitting of the FID signals and reveal microstructural and molecular information of the measured matter. This technique is referred to as *NMR Relaxometry*.

Additionally, further dephasing of magnetization will occur due to spatially inhomogeneous $\boldsymbol{B}_0$ and result in an additional signal decay with the characteristic time T_2'. In such cases, the *effective transversal relaxation time* T_2^* is given by

$$\frac{1}{T_2^*} = \frac{1}{T_2} + \frac{1}{T_2'}. \tag{1.20}$$

T_2^* can be slightly or severely shorter than T_2. A *refocusing pulse* can be used after the preceding excitation pulse for rephasing of the magnetization dephased by $\boldsymbol{B}_0$ inhomogeneity (*i.e.* related to T_2' relaxation), leading to the so-called *Spin Echo* (SE) signals (*cf.* Figure 1.4). The *Echo Time* (TE) is defined as the delay between the excitation pulse (typically the time point of the pulse peak) and the time point of the phase recoherence, and is twice the delay between the excitation pulse and the subsequent refocusing pulse τ (*i.e.* $TE = 2\tau$).

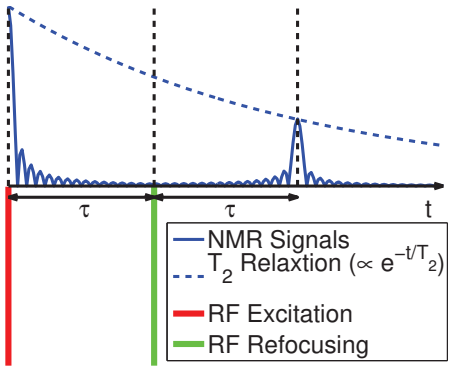

Figure 1.4: Formation of a single SE at $TE = 2\tau$ by an excitation pulse (red bar) and a subsequent refocusing pulse (green bar).

It is noteworthy that NMR signals can often be estimated based on the induction of M_{xy}. According to Equation 1.10 and 1.14, the estimated NMR signals are given by

$$S \propto 2\pi\nu_0 \cdot M_{xy} = \gamma B_0 \cdot M_0 sin\alpha \propto \frac{\hbar L}{k_B T}\gamma^3 B_0^2 sin\alpha. \tag{1.21}$$

This indicates the superiority of the ^1H nucleus to others because of its high gyromagnetic ratio γ and natural abundance 99.985 % (*cf.* Table 1.1).

On the other hand, NMR at higher B_0 is superior to lower B_0 regarding to the *Signal-to-Noise Ratio* (SNR), however with several drawbacks like more extensive image artifacts in some applications. With a range from $0.05\,mT$ (earth magnetic field strength) to $23.5\,T$ (which may still be higher in the future), the resonance frequency ν_0 of the ^1H nucleus varies from $2\,KHz$ to $1\,GHz$, and is most often in the *Radio-Frequency* (RF) range.

Table 1.1: Gyromagnetic ratios and natural abundances of some nuclei.

nucleus	$\frac{\gamma}{2\pi}\,[MHz/T]$	natural abundance [%]
^1H	42.577	99.985
^3He	−32.434	0.000137
^{13}C	10.705	1.11
^{19}F	40.052	100
^{23}Na	11.262	100
^{31}P	17.235	100
^{129}Xe	−11.777	26.401

A spin usually experiences mildly varied $\boldsymbol{B}_0$ since it is shielded by surrounding electron clouds in the molecules, and thus has the resulting resonance frequency shift called *Chemical Shift* (CS) σ. Therefore, its resonance frequency ν_0 is replaced by $(1-\sigma)\nu_0$. By *Fourier transform* of NMR signals, CS spectra of the magnetization can be gained for investigation of biochemical information about the measured matter. This technique is called *NMR Spectroscopy*, and is widely used in analytical chemistry.

Note that the Fourier spectrum of time-domain NMR signals

$$S(t) \propto M_{xy}(0)e^{-\frac{t}{T_2^*}-i2\pi\nu_0 t} \tag{1.22}$$

is a Lorentzian function with a linewidth LW_{signal} given by

$$LW_{signal} = \frac{1}{\pi T_2^*}, \tag{1.23}$$

as illustrated in Figure 1.5. For spatial resolution, the acquisition bandwidth BW_{acq} should satisfy

$$BW_{acq} \gg LW_{signal} = \frac{1}{\pi T_2^*} \tag{1.24}$$

and the *dwell time* t_d for signal sampling is then given by

$$t_d = \frac{1}{BW_{acq}} \ll \pi T_2^*. \tag{1.25}$$

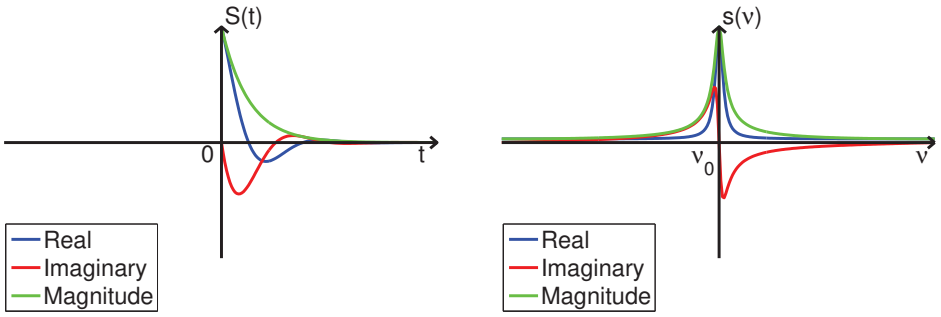

Figure 1.5: Fourier transform pair of exponential decay (a) and Lorentzian function (b).

In most NMR experiments, a certain *recovery delay* is used after the acquisition of NMR signals for magnetization recovering before the next excitation pulse is performed. The term *Repetition Time* (TR) describes the period length. With a sufficiently long TR, the magnetization will recover to the thermal equilibrium $\boldsymbol{M}_0$. Otherwise, with a shortened TR, it will reach a *steady state* after a number of TR-periods. In such cases, NMR signals within these initial periods before reaching the steady state are regarded as *dummies*, and are not considered for acquisition. When excitation pulses with a large FA are used (*e.g.* $\alpha = 90\,^\circ$), the total duration of the dummy periods t_{dummy} is typically

$$t_{dummy} = N_{dummy} TR > 5 \cdot T_1. \tag{1.26}$$

The total measurement can be repeated for a *Number of Averages* (NA) for averaging signals, and thus increasing the SNR. The backbone of an NMR method is the *NMR Pulse Sequence*, which describes the arrangement of all RF transmission and reception as well as pulsed magnetic field gradients (*cf.* Section 1.2) applied in the TR-periods during the NMR measurement.

1.1.5 RF Pulses and Coherence Pathways

The *pulse phase* θ is defined as the angle between the direction of the pulsed $\boldsymbol{B}_1$ field in the rotating frame of reference and the x'-axis. By an RF pulse with an FA of α and $\theta = 0\,^\circ$ without losing generality (*i.e.* along the x'-axis), the transversal and longitudinal components of the magnetization are changed to

$$M_{xy}^{(+)} = M_{xy}^{(-)} cos^2\frac{\alpha}{2} + M_{xy}^{*(-)} sin^2\frac{\alpha}{2} + iM_z^{(-)} sin\alpha \tag{1.27}$$

and

$$M_z^{(+)} = iM_{xy}^{(-)}\frac{1}{2}sin\alpha - iM_{xy}^{*(-)}\frac{1}{2}sin\alpha + M_z^{(-)}cos\alpha, \tag{1.28}$$

respectively, where $(-)$ and $(+)$ represent the time points just before and after the RF pulse, respectively.

Each RF pulse can then be considered as a combination of three parts: a $0\,^\circ$-part for conserving a magnetization component, a $90\,^\circ$-part for transferring a magnetization component to another orthogonal component, and a $180\,^\circ$-part for transferring the transversal component of the magnetization to its complex conjugation. The portions of these three parts in each RF pulse and their corresponding effects on magnetization can be derived according to Equation 1.27 and 1.28, and are illustrated in Table 1.2.

Table 1.2: Portions of $0\,^\circ$-, $90\,^\circ$-, and $180\,^\circ$-parts in an RF pulse and the corresponding effects on magnetization.

	$0\,^\circ$-part	$90\,^\circ$-part	$180\,^\circ$-part
$M_{xy}^{(-)}$	$cos^2\frac{\alpha}{2} \rightarrow M_{xy}^{(+)}$	$\frac{1}{2}sin\alpha \rightarrow M_z^{(+)}$	$sin^2\frac{\alpha}{2} \rightarrow M_{xy}^{*(+)}$
$M_{xy}^{*(-)}$	$cos^2\frac{\alpha}{2} \rightarrow M_{xy}^{*(+)}$	$\frac{1}{2}sin\alpha \rightarrow M_z^{(+)}$	$sin^2\frac{\alpha}{2} \rightarrow M_{xy}^{(+)}$
$M_z^{(-)}$	$cos\alpha \rightarrow M_z^{(+)}$	$sin\alpha \rightarrow M_{xy}^{(+)}$	

A *coherence pathway*, in which the magnetization evolves through a train of coherence orders by experiencing the corresponding parts of every RF pulse, can thus be denoted as a train of effective parts of the experiencing RF pulses. Phase coherence may be achieved in certain coherence pathways, thus forming an echo. Dephased M_{xy} can be rephased by identical dephasing of its complex conjugation, which can be gained by a $180\,^\circ$-part of an RF pulse, thus forming an SE. For instance, a single SE after two RF pulses originates from the coherence pathway of $90\,^\circ \sim 180\,^\circ$. Another type of echo, called *STimulated Echo* (STE), can be formed by at least three RF pulses. In such cases, the $90\,^\circ$-part of an RF pulse flips dephased M_{xy} to M_z, and the $90\,^\circ$-part of another RF pulse flips the preserved M_z back to M_{xy} for further rephasing. For example, the single STE after three RF pulses originates from the coherence pathway of $90\,^\circ \sim 90\,^\circ \sim 90\,^\circ$. Further detailed descriptions about coherence pathways can be found in [5, 6, 7, 8].

Coherence pathways can be selectively strengthened or weakened by *phase cycling*, in which RF pulses and signal acquisition have own phase cycles within TR periods and/or NA repetitions. A simple bipolar phase cycle for the refocusing pulse in a single SE pulse sequence can effectively suppress FID signals from the refocusing pulse. There are several useful phase cycles, like XY [9, 10] and MLEV [11].

1.2 NMR Techniques with Gradients

The *magnetic field gradient* or *gradient* in short, represents an additional magnetic field in the z-direction (B_g) with a certain duration t_g. Its magnitude varies in a linear manner in three orthogonal spatial directions, *i.e.* the gradient can be described by $\boldsymbol{G} = \nabla B_g = (G_x, G_y, G_z)$. During such a gradient, B_0 is replaced by $B_0 + B_g = B_0 + \boldsymbol{G} \cdot \boldsymbol{r}$ with $\boldsymbol{r} = (x, y, z)$. Therefore, the angular resonance frequency ω_0 is replaced by $\omega_0 + \gamma \boldsymbol{G} \cdot \boldsymbol{r}$. By applying gradients, information regarding to spatial position (distribution and displacements) can be encoded into the phase of spins, and thus tomographic imaging as well as measurement of displacements are enabled. This section introduces briefly the NMR techniques with pulsed gradients. Further detailed descriptions can be found in many NMR textbooks, *e.g.* [1, 2, 3, 4].

1.2.1 Gradient introduced Dephasing and Rephasing

If a gradient is applied, the magnetization will dephase more rapidly due to considerably higher $\boldsymbol{B}_0$ inhomogeneity. Rephasing of the magnetization can be achieved by applying a second gradient with opposite polarity. Fully rephasing occurs when the *gradient area* of the rephasing gradient is extinguished by the gradient area of the dephasing gradient. Here the gradient area is the integral of the gradient over time $\int_{t_g} \boldsymbol{G}(t)dt$. This phase recoherence leads to echo-like signals because of gradient introduced refocusing, or so-called *Gradient Recalled Echo* (GRE) signals. In such cases, the term TE is extended to the delay between the excitation pulse (typically the time point of the pulse peak) and the time point of phase recoherence.

Without the rephasing gradient, phase decoherence remains and the resulting NMR signals are spoiled. Thus, the dephasing gradient with the aim to suppress unwanted signals or coherence pathways is termed *spoiler gradient*.

1.2.2 Slice Selection

Magnetization in a slice with a finite thickness can be selectively excited by applying the *slice selection gradient* during the excitation pulse. With such a gradient, spins have linearly varying resonance frequencies in the *slice direction*. Only those spins which are in coincidence with the frequency band of the excitation pulse, *i.e.* in the selected slice, will be excited (*cf.* Figure 1.6).

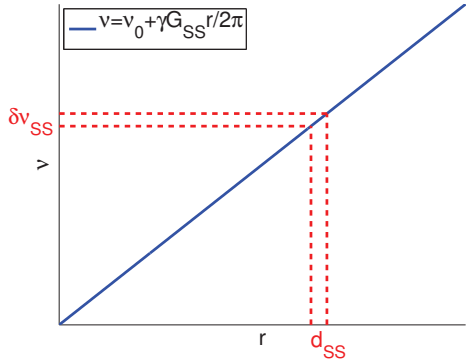

Figure 1.6: Magnetization in a slice is selectively excited by applying the slice selection gradient G_{SS} during the excitation pulse. Spins in coincidence (red dashed lines) with the frequency band (bandwidth $\delta\nu_{SS}$) of the excitation pulse, *i.e.* in the selected slice (slice thickness d_{SS}), will be excited.

Given a slice selection gradient in a certain direction with a magnitude G_{SS} and an RF pulse with a central frequency $\nu_0 + \Delta\nu_{SS}$ and a bandwidth $\delta\nu_{SS}$, the slice position r_{SS} and the *slice thickness* d_{SS} can be described by

$$r_{SS} = \frac{2\pi \cdot \Delta\nu_{SS}}{\gamma G_{SS}}, \tag{1.29}$$

and

$$d_{SS} = \frac{2\pi \cdot \delta\nu_{SS}}{\gamma G_{SS}}, \tag{1.30}$$

respectively.

Note that in-slice dephasing occurs during the slice-selective excitation due to gradient introduced off-resonance. After the excitation, the magnetization in the excited slice can be rephased by a subsequent *slice rephasing gradient*, which often has half the gradient area of the slice selection gradient when a symmetric RF pulse is used.

By applying multiple slice-selective RF pulses and spoiler gradients, phase recoherence can occur only for the magnetization in a chosen single volume. Such methods are called *Localized NMR*.

1.2.3 Basics of k-Space

The transversal component of a magnetization at certain spatial position $M_{xy}(\boldsymbol{r})$ will gain additional phase after experiencing a gradient $\boldsymbol{G}$, as follows

$$M_{xy}(\boldsymbol{r})e^{i\int_{t_g}\gamma\boldsymbol{G}(t)\cdot\boldsymbol{r}dt} = M_{xy}(\boldsymbol{r})e^{i2\pi\cdot\frac{\gamma}{2\pi}\int_{t_g}\boldsymbol{G}(t)dt\cdot\boldsymbol{r}} = M_{xy}(\boldsymbol{r})e^{i2\pi\cdot\boldsymbol{k}\cdot\boldsymbol{r}} \tag{1.31}$$

with

$$\boldsymbol{k} = \frac{\gamma}{2\pi}\int_{t_g} \boldsymbol{G}(t)dt = \frac{\gamma}{2\pi} \cdot gradient\ area. \tag{1.32}$$

Therefore, the corresponding NMR signal in such a *k-space* point $S(\boldsymbol{k})$ is given by

$$S(\boldsymbol{k}) \propto \int M_{xy}(\boldsymbol{r})e^{i2\pi\boldsymbol{k}\cdot\boldsymbol{r}}d\boldsymbol{r}. \tag{1.33}$$

The NMR signals in the k-space can then be Fourier transformed into the NMR signals in the spatial domain, or the complex-valued NMR images, as shown in Figure 1.7. In the cases of SE or STE, the resulting NMR signal at certain spatial position can be described by

$$s(\boldsymbol{r}) = \int S(\boldsymbol{k})e^{-i2\pi\boldsymbol{k}\cdot\boldsymbol{r}}d\boldsymbol{k} \propto M_{xy}(\boldsymbol{r}) = M_0(\boldsymbol{r}) \cdot sin\alpha \cdot e^{-\frac{TE}{T_2(\boldsymbol{r})}} \cdot w(\alpha, \frac{TR}{T_1(\boldsymbol{r})}), \tag{1.34}$$

which are weighted by spin density contrast $M_0(\boldsymbol{r})$, T_2 contrast $e^{-\frac{TE}{T_2(\boldsymbol{r})}}$, and T_1 contrast $w(\alpha, \frac{TR}{T_1(\boldsymbol{r})})$. Such k-space NMR technique is termed *NMR Tomography* or *NMR Imaging* (MRI). Note that additional contrast occurs when $\boldsymbol{B}_1$ inhomogeneity exists ($\alpha = \alpha(\boldsymbol{r})$). On the other hand, T_2^* contrast $e^{-\frac{TE}{T_2^*(\boldsymbol{r})}}$ will replace T_2 contrast if FID or GRE signals instead of echoes (SE or STE) are acquired. Combined with the k-space concept, spatially resolved NMR Relaxometry and Spectroscopy, or named *NMR Relaxivity Mapping* and *NMR Spectroscopic Imaging*, are enabled.

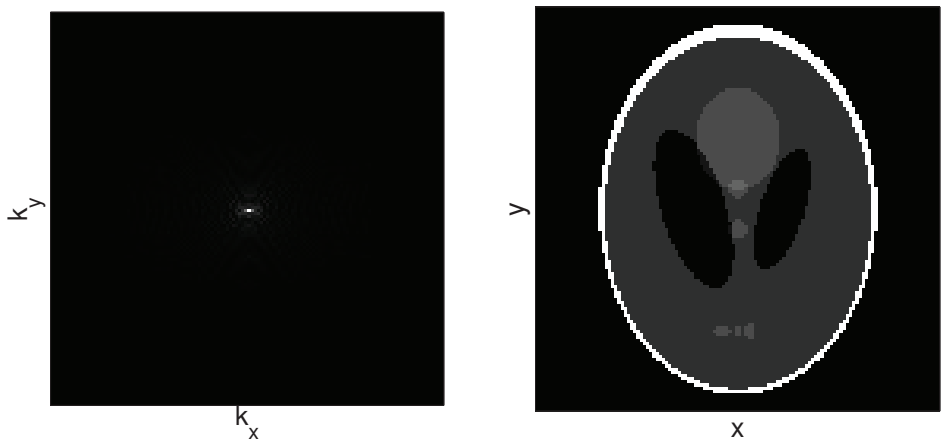

Figure 1.7: Signals in the k-space (a) and images in the real space (b) of a Shepp-Logan phantom.

Traversing the k-space can be performed by *frequency encoding* and/or *phase encoding*. Frequency encoding means that the NMR signals are read during a *read gradient* G_r applied with a fixed magnitude, which gives rise to a resonance frequency spectrum of spins encoding the corresponding *1D projection* in the k-space. Phase encoding means an encoding gradient G_{PE} (typically with a fixed duration and a varying magnitude in different TR-periods) is applied for movements in the k-space before acquisition. With non-Cartesian k-space grids, a non-uniform Fourier transform, or a regridding plus a uniform Fourier transform, can generate NMR images within Cartesian grids in the real space.

In the *discrete Fourier transform* between the k-space and spatial grids, the product of both grid sizes δk and δr satisfies

$$\delta k \cdot \delta r = \frac{1}{N} \tag{1.35}$$

with the *matrix size* N. Given the *Field Of View* (FOV) as the measured spatial range, the spatial grid or volume element (*voxel*) has a size of δr given by

$$\delta r = \frac{FOV}{N}. \tag{1.36}$$

Thus, by substituting Equation 1.36 into 1.35,

$$\delta k = \frac{1}{N\delta r} = \frac{1}{FOV}. \tag{1.37}$$

According to Equation 1.37, in the read direction,

$$\delta k_r = \frac{\gamma}{2\pi} G_r t_d = \frac{1}{FOV_r}, \tag{1.38}$$

and therefore

$$G_r = \frac{2\pi}{\gamma FOV_r t_d} = \frac{2\pi BW_{acq}}{\gamma FOV_r}. \tag{1.39}$$

So the voxel size is determined by the acquisition bandwidth BW_{acq} and the read gradient magnitude G_r. According to Equation 1.24, the point-wise bandwidth must meet

$$\frac{BW_{acq}}{N_r} = \frac{\gamma G_r FOV_r}{2\pi N_r} \gg \frac{1}{\pi T_2^*}, \tag{1.40}$$

which can be rewritten as

$$\delta r_r = \frac{FOV_r}{N_r} = \frac{2\pi}{\gamma G_r} \cdot \frac{BW_{acq}}{N_r} \gg \frac{2}{\gamma G_r T_2^*}. \tag{1.41}$$

This indicates that the spatial resolution is limited by both the encoding gradient and the point spreading function due to T_2^* relaxation.

Image artifacts may take place in many situations, *e.g.* motion of the measured matter during the measurements, NMR hardware instability, and distorted k-space. The mismatching points in the k-space can originate from off-resonance effects (*CS*, *magnetic susceptibility*, and so on) and encoding gradient imperfections (*eddy currents* as well as *concomitant fields*).

1.2.4 Basics of q-Space

Spatial displacements of spins can take place due to molecular diffusion and flow. The displacements can be described by the *propagator* P, which is a probability density function of spin displacements $\Delta\boldsymbol{r}$ and satisfies

$$\int_{-\infty}^{+\infty} P(\Delta\boldsymbol{r})d(\Delta\boldsymbol{r}) = 1. \tag{1.42}$$

By applying a pair of *bipolar gradients*, which are identical to each other except for opposite polarities, the NMR signals will be modulated by the propagator with additional displacement related phase

$$\int_{-\infty}^{+\infty} P(\Delta\boldsymbol{r})e^{i2\pi\boldsymbol{q}\cdot\Delta\boldsymbol{r}}d(\Delta\boldsymbol{r}), \tag{1.43}$$

with

$$\boldsymbol{q} = \frac{\gamma}{2\pi}\int_{t_g} \boldsymbol{G}(t)dt = \frac{\gamma}{2\pi}\cdot gradient\ area \tag{1.44}$$

of one of the *displacement encoding* gradients. Note that static spins do not obtain such additional phase.

According to the mathematical description, the definition of $\boldsymbol{q}$ is identical to the definition of $\boldsymbol{k}$. However, the concept of *q-space* is still defined here, extending displacement-based dimensions of NMR signals and thus differentiating itself from the k-space concept. The propagator revealing diffusion and velocity information can then be extracted by a Fourier transform of the q-space NMR signals, and the corresponding methods are termed *NMR Diffusometry* and *NMR Velocimetry*, respectively.

Combined with the concept of k-space, the q-space NMR is capable of spatially resolving diffusion and velocity, and is termed *q-space MRI*. Figure 1.8 shows Gaussian diffusion (*cf.* Figure 1.8a and 1.8b) and motion with a constant velocity (Figure 1.8c and 1.8d) as the two simple examples using the q-space concept. In such cases, the propagators are assumed as Gaussian (*cf.* Figure 1.8a) and Dirac (*cf.* Figure 1.8c) functions, respectively. The former

results in an exponential magnitude decay of the NMR signals based on the q-value and *diffusion coefficient* (*cf.* Figure 1.8b), and the latter results in a linear phase shift of the NMR signals based on the q-value and velocity (*cf.* Figure 1.8d).

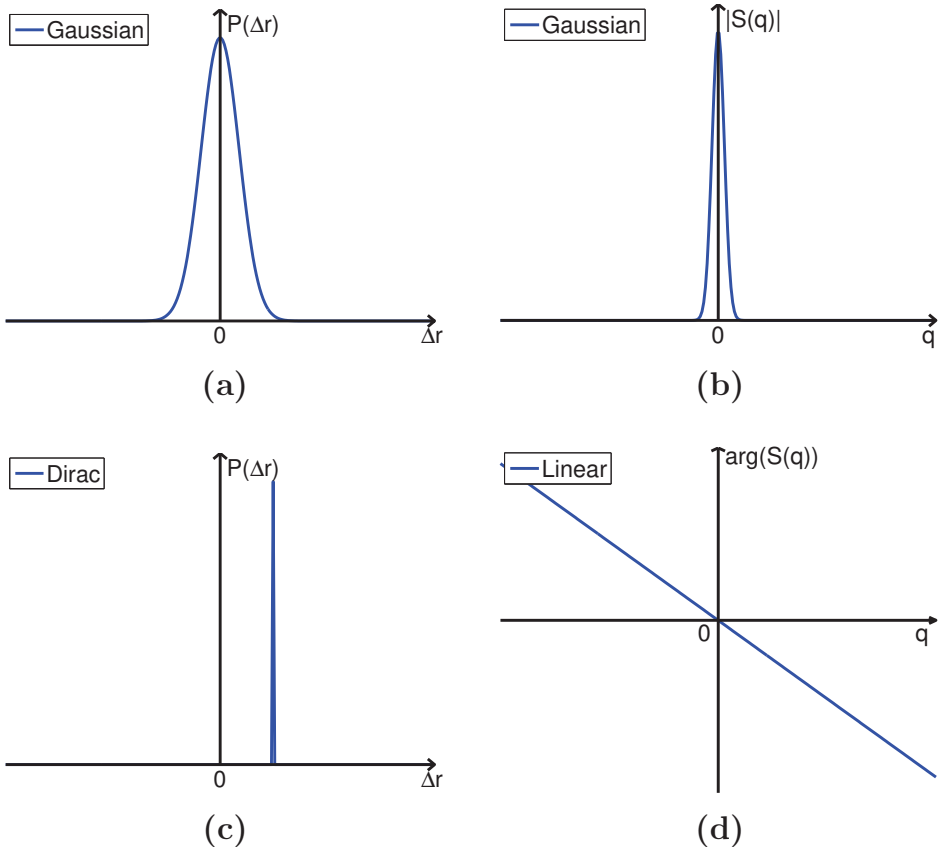

Figure 1.8: Two simple examples of propagators and corresponding signals in the q-space as Fourier transform pairs. (a) A propagator as a Gaussian function. (b) The magnitude of the corresponding signals in the q-space as a Fourier transform of the Gaussian function in (a) is another Gaussian function. (c) A propagator as a Dirac function. (d) The phase of the corresponding signals in the q-space as a Fourier transform of the Dirac function in (c) is a linear function.

The displacement information can then be measured with a substantially reduced number of q-space encoding steps. The corresponding techniques are defined as *Diffusion Weighted MRI* (DW-MRI) and *Phase Contrast MRI* (PC-MRI), respectively. The former technique can be extended to *Diffusion Tensor MRI* (DT-MRI) for considering of anisotropic diffusion. Specific data post-processing procedures other than Fourier transform are often required

in such simplified q-space MRI techniques, *e.g.* exponential fitting for DW-MRI, phase differencing for PC-MRI.

1.3 NMR Applications

With the capability of non-invasively revealing physical, chemical, and biological properties of matter, NMR technology is used in a wide range of areas, *e.g.* in clinical areas for diagnostic imaging or MRI-guided interventions, in biology for the analysis of protein structures, in analytical chemistry for the analysis of chemical compounds.

Furthermore, NMR technology finds broad applications for investigations on porous materials [3, 12] including porous ceramics, cement-based materials, rocks, coals, packed beds of beads, polymers, pharmaceutical tablets, as well as thin films. One main focus on dynamic processes in such heterogeneous systems is the mass transport in the porous structures, particularly the physical transfer of fluids within the pores, *e.g.* drying and sorption as well as flow. Spatially resolving the mass transport can help better understanding the mechanisms underlying the corresponding dynamic processes and improve system designs.

The main challenges of spatially resolved NMR on porous materials are the strong magnetic susceptibility effects at the interfaces between heterogeneous matter [3, 12]. Then $\boldsymbol{B}_0$ is highly inhomogeneous with *internal gradients*, and thus T_2^* is usually much shorter than T_2. As a result, conventional GRE is typically not suitable, and NMR methods using ultrashort TE FID signals or echoes (SE and/or STE) are backbones. Moreover, an adequate temporal resolution is also demanded for monitoring the changes of the heterogeneous systems, which is particularly difficult to achieve when high 3D spatial resolution is also required. There will also be additional drawbacks in specific applications like low NMR sensitivity in measuring gases in porous materials.

1.4 NMR Facilities

In general, NMR facilities contain the magnet for providing $\boldsymbol{B}_0$, the gradient system for generating the gradients, the RF coils for transmitting $\boldsymbol{B}_1$ and/or receiving NMR signals, the gradient and RF amplifiers, the digitizer for *Analog-to-Digital Conversion*, and the console for controlling the scanner.

In this work, a horizontal-bore $7\,T$ NMR scanner (Bruker BioSpec 70/20 USR, Bruker BioSpin MRI, Germany) with a gradient system (B-GA 12S2,

Bruker BioSpin MRI, Germany) was used (*cf.* Figure 1.9). The superconducting magnet with helium cooling has a bore diameter of $200\,mm$, and the resonance frequency for ^1H nucleus is $300\,MHz$. The gradient system with water cooling has a bore diameter of $114\,mm$. It can generate gradients with a maximum magnitude of $440\,mT/m$ ($18.8\,KHz/mm$) and a *slew rate* of $3440\,T/m/s$ (usually $130\,\mu s$ for gradient ramping). It also has room temperature shim coils up to the second order for homogenizing $\boldsymbol{B}_0$. Multiple RF coils can be used for different purposes. The console is a Linux workstation with ParaVision 5.1 (Bruker BioSpin MRI, Germany), in which pulse sequence programming, measurements by protocols with pulse sequences, and online image reconstruction can be performed. Furthermore, offline image reconstruction and data post-processing were performed on another Linux workstation with higher computation power in Matlab R2014a (MathWorks, USA). Some open-source software was also used for specific tasks in image processing, *e.g.* Slicer 4.4 (National Institute of Health, USA) [13] for image registration.

Figure 1.9: Photo of the NMR scanner used in this work.

Chapter 2

Zero Echo Time MRI of Drying

2.1 Introduction

Drying in porous materials [14] is defined as the process in which liquids (water or solvents) within pores are removed by evaporation over time. The drying process is often employed in a variety of applications, *e.g.* hydration of cement-based materials, moisture removal in foods, and curing of polymer films. The quality of the resulting products is notably affected by the drying process and the remaining liquids. Sophisticated mechanisms underlying the drying process include evaporation, capillary and film flow, as well as diffusion. The drying process can be controlled by tailoring the corresponding conditions like temperature, pressure, and air stream. By monitoring the amount and distribution of liquids in porous materials over time, the drying process can then be characterized for analyzing the material quality and investigating the drying mechanisms. This can certainly help to find improved production procedures.

The evolution of liquid evaporation in porous materials can be simply measured by a balance. However, this can only provide macroscopic evaluation of the whole sample. Recent advances in non-destructive analytical imaging technologies open new doors to spatially resolved studies of the drying process inside porous materials, which are often opaque and thus do not allow the use of optical imaging technologies.

Among these technologies, *X-ray Micro-Tomography* (XMT) [15, 16] is often considered superior to other imaging technologies with its capability of ultrahigh spatial resolution imaging. The principle of XMT is that an object can be reconstructed by inverse Radon transform of 1D projections, which are line integrals of the object and are measured under a lot of different projecting angles. In XMT, such line integrals as signals are acquired from

X-ray radiation that penetrates the measured matter and is attenuated by absorption. Therefore, the reconstructed XMT images are weighted by X-ray absorption coefficient contrast. With an array of precise detection units and a very small increment step of the projecting angles, XMT can achieve ultrahigh spatial resolution imaging. Note that a high dynamic range in XMT is demanded for studies involving soft matter, since the X-ray absorption by soft matter is typically much weaker than by hard matter. Moreover, the projection-based XMT requires rotation of the measured object or the X-ray beam source plus the array of detection units. The former implies a change of the drying conditions and disables *in situ* imaging, while the latter is often an unusual setup of an XMT scanner, particularly for material studies.

MRI can provide *in situ* high spatial resolution images with much more versatile contrast, *e.g.* spin density, T_1, and T_2. For drying studies, moderate measurement time is often demanded for reasonable temporal resolution. Conventional GRE-based MRI methods are not suitable for drying studies in porous materials for very fast T_2^* relaxation. To overcome these effects of B_0 inhomogeneity, RF refocusing resulting in SE or STE signals can be performed. However, T_2 contrast may be large and even evolve during the experiment, leading to systematic errors in some studies and requesting additional calibration. Another choice is *pure phase encoding* [17, 18], by which no frequency encoding is applied and minimum TE can be much shorter than in conventional MRI. However, the drawback of inefficient acquisition in the k-space limits the temporal resolution, which is particularly important if high 3D spatial resolution is required.

Zero Echo Time (ZTE) MRI [19, 20, 21, 22, 23, 24, 25] is a fast and robust 3D imaging method, which has been shown to have great potential for imaging matter with short T_2^* relaxation, particularly for musculoskeletal imaging in biomedical studies. In ZTE MRI, pure frequency encoding gradients are already switched on before the excitation pulse and the subsequent radial center-out k-space acquisition. Using a short excitation pulse (typically $2\,\mu s$ to $20\,\mu s$) with a small FA (typically $\alpha < 10\,^\circ$) makes the slice selection effect of an RF pulse negligible and also avoids RF heating. Since a short TR ($< 15\,ms$) is possible, ZTE MRI can yield high 3D spatial resolution without sacrificing temporal resolution. The *dead time* t_{dead} [26] is defined as the delay between the excitation pulse and the beginning of acquisition. It equals to the sum of one half of the excitation pulse duration, the transmitter/receiver switching time, and the signal build-up delay of the digitizer. The dead time t_{dead} can be very short (typically $< 20\,\mu s$), and therefore T_2^* contrast can be minimized. ZTE NMR image intensities proved to yield reasonable estimates for spin density mapping [27, 28].

Compared to the similar *Ultrashort Echo Time* (UTE) MRI, in which

the frequency encoding gradient is only switched on after the RF pulse, ZTE MRI does not require extra compensation of gradient delays [29], which is necessary when gradients in three orthogonal directions are not perfectly synchronized and cause radial artifacts in the resulting images. However, several *missing points* in the central k-space cannot be acquired in ZTE MRI due to the dead time t_{dead}.

In this subproject, ZTE MRI was used for characterizing the drying process in porous materials. To the best of my knowledge, this topic has never been described in journals before. Image artifacts, which do not occur in conventional MRI, were investigated and efficiently reduced by two strategies. One was saturating slices in the outer volume for magnetization preparation in the pulse sequence, and the other was using an optimized ^1H-free RF coil.

2.2 Investigation of Wave-pattern Artifacts

Initial experiments measuring water distribution in porous materials by ZTE MRI yielded images with wave-pattern artifacts, which do not exist in conventional MRI. Such image artifacts were identified to be related to ultrafast decaying signals from NMR hardware instead of missing points in the central k-space.

2.2.1 Sample Preparation, Pulse Sequence, and Image Reconstruction

In preliminary studies on the evolution of water evaporation in porous materials, ZTE MRI using a commercial horizontal 72 mm-bore birdcage ^1H quadrature transceiver RF coil (Bruker BioSpin MRI, Germany; named *Bruker coil* in the rest of the thesis) was performed on water-ceramic-cup samples. These samples are constituted by ^1H-free porous ceramics within distilled water in a ^1H-free *PolyTetraFluoroEthylene* (PTFE) cup (*cf.* Figure 2.1). All the porous ceramics in this subproject were made of aluminum oxide (Al_2O_3) and/or silicon dioxide (SiO_2), and have mean pore sizes in a range from submillimeters to millimeters. They were produced according to [30, 31] by the collaborators (Gesa Hollermann and Benjamin Besser) from the Advanced Ceramics Group, Faculty 04 (Production Engineering), University of Bremen. T_2^* of water in such porous ceramics ranges from microseconds to submilliseconds.

In the preparation of the water-ceramic-cup samples, the porous ceramics were saturated by distilled water according to the following steps:

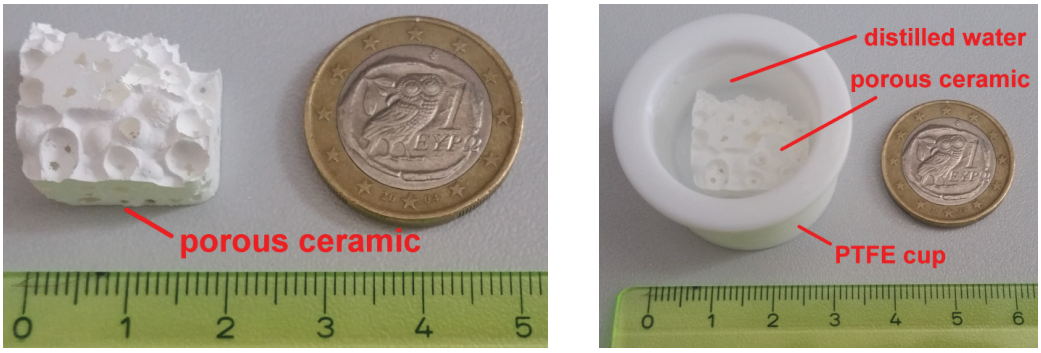

(a) (b)

Figure 2.1: Photos of a representative water-ceramic-cup sample. (a) The porous ceramic. (b) The corresponding water-ceramic-cup sample constituted by the porous ceramic in (a) within distilled water in a PTFE cup.

1. The porous ceramics were placed in the PTFE cup. Distilled water was filled into the cup, submerging the porous ceramics for pore presaturation.

2. Pore saturation was achieved by using an ultrasound bath (SONOREX SUPER RK 100H, BANDELIN electronic, Germany) for 15 min.

3. Due to the ultrasound heating of the water, the whole object had to be cooled down for at least 15 min to room temperature.

Figure 2.2 shows the pulse sequence and corresponding k-space trajectories of the existing ZTE MRI implementation available in ParaVision 5.1. In ZTE MRI, typically a large BW_{acq} ($> 100\,KHz$) is used for imaging matter with short T_2^* relaxation, the frequency encoding gradient in each TR interval is usually prolonged as a spoiler gradient after the acquisition, and oversampling is necessary for subsequent image reconstruction.

FID signals of each spoke in the k-space were then constructed by combining both the positive and negative half spokes and algebraically compensated within the missing points [32]. The trajectories of spokes in the k-space were calculated according to the frequency encoding gradients applied. The k-space data points in the spiky trajectories were regridded to data points in Cartesian grids [33, 34, 35, 36, 37]. Finally the NMR images were reconstructed by Fourier transform of the regridded k-space data points. All these procedures were executed as the online image reconstruction part of the existing ZTE MRI implementation available in ParaVision 5.1.

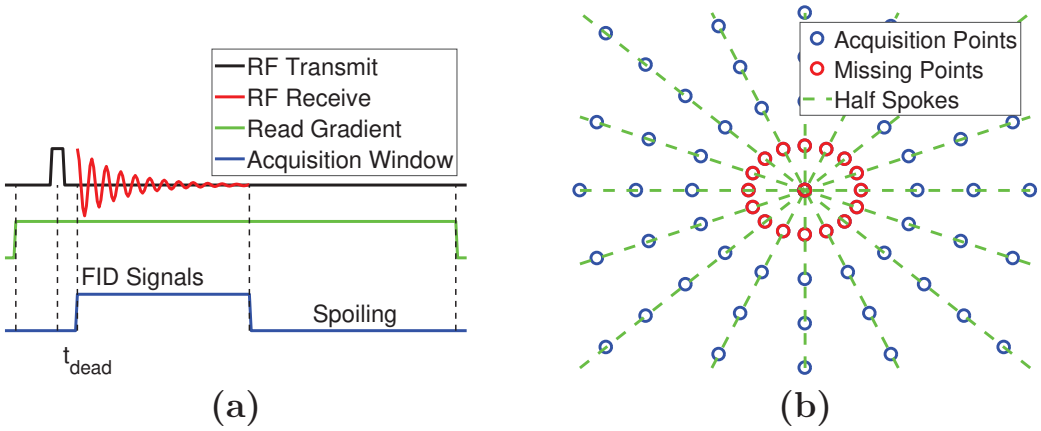

Figure 2.2: The pulse sequence (a) and corresponding k-space trajectories (b) of ZTE MRI.

2.2.2 Wave-pattern Artifacts

In initial experiments on a water-ceramic-cup sample, ZTE MRI was performed with the following protocol: BW_{acq} $150\,KHz$, no undersampling, number of half spokes 116280, TR $4.0\,ms$, NA 1, measurement time $7.75\,min$, rectangular pulse for excitation with α 4° and t_p $2\,\mu s$, number of missing points per half spoke 1.65, spoiling factor $1.5\,cycles/voxel$, switching gradients off in each TR interval, oversampling factor 2, dead time t_{dead} $6\,\mu s$, FOV $40\times40\times40\,mm^3$, matrix size $192\times192\times192$, voxel size $208\times208\times208\,\mu m^3$.

The resulting ZTE NMR images were overlaid by unwanted wave-pattern image artifacts, which have stripe patterns like 3D propagating waves from point sources close to the image origin, as shown in Figure 2.3. The inhomogeneity of image intensities of voxels within each pore might originate from T_2^* contrast. Thus under the consideration of additional T_2 relaxation at the pore surface [38], it should be expected that voxels closer to the pore center have higher image intensities than voxels further from the pore center. However, this explanation was violated for arbitrarily chosen pores, *e.g.* the pore in the image center in Figure 2.3. The origin voxel, which was nearly the pore center, had an image intensity valley instead of a peak compared to neighboring voxels in the identical pore. Moreover, image intensities of voxels in the bulk water region outside the porous ceramics were substantially inhomogeneous. The wave-pattern image artifacts introduced non-existent object structures, and were more severe for studies on objects with super-pore-scale spatial resolution.

Since a whole-image pattern corresponds to the central k-space, it was hypothesized that such wave-pattern artifacts originate from the missing points.

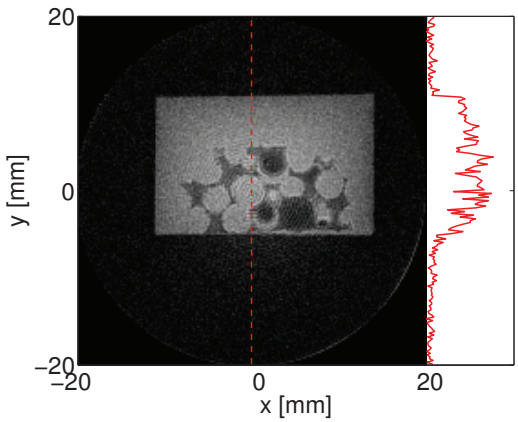

Figure 2.3: Wave-pattern artifacts in ZTE NMR image of a water-ceramic-cup sample.

In ZTE MRI, the missing points are algebraically compensated [32] before re-gridding and Fourier transform. The algebraical compensation is performed by solving the inverse problem, in which the acquired FID signals in each spoke are truncated Fourier-transformed projections of the measured object with a finite length. In practice, the constraint for solving such an inverse problem is that the region outside the measured object in the FOV only provides noise-level signals.

In studies on ultrashort T_2^* matter, *e.g.* liquids in porous materials, a very large BW_{acq} is necessary. However, with such a BW_{acq}, the region outside the measured object in the FOV may yield non-negligible signals instead of noise-level signals. Hence, the algebraical compensation of missing points may be not reliable. Additionally acquiring the missing points with pure phase encoding proved to be an effective means for rebuilding the central k-space [39, 40]. In this subproject, additional FID signals without gradients were acquired and the first data point was used to fill the missing point in the k-space origin. If a large BW_{acq} and a small oversampling factor are used, the k-space origin will not be the only missing point, and this additional FID signal acquisition cannot measure the other non-origin missing points in the central k-space. However, this acquisition would still substantially reduce the whole-image artifacts by providing a reliable k-space origin according to the hypothesis.

This modification of using the acquired k-space origin was already usable in the existing ZTE MRI implementation available in ParaVision 5.1. The hypothesis was examined on another water-ceramic-cup sample. By using the Bruker coil, ZTE MRI and SE MRI were performed for comparison. The ZTE MRI method was applied with the following protocol: BW_{acq} 150 KHz,

no undersampling, number of half spokes 51896, TR 3.0 ms, NA 1, measurement time 2.59 min, rectangular pulse for excitation with α 5 ° and t_p 2 μs, number of missing points per half spoke 1.09, spoiling factor 1.5 $cycles/voxel$, switching gradients off in each TR interval, oversampling factor 8, dead time t_{dead} 6 μs, FOV $32 \times 32 \times 32\,mm^3$, matrix size $128 \times 128 \times 128$, voxel size $250 \times 250 \times 250\,\mu m^3$, using the acquired k-space origin. And the SE MRI method was applied with the following protocol: BW_{acq} 150 KHz, TR 0.8 s, NA 4, measurement time 7.28 h, hermite pulse for excitation with α 90 ° and t_p 0.25 ms, hermite pulse for refocusing with α 180 ° and t_p 0.5 ms, TE 3.3 ms, read direction x, slice direction y, FOV $32 \times 32 \times 16\,mm^3$, matrix size $128 \times 128 \times 64$, voxel size $250 \times 250 \times 250\,\mu m^3$.

As shown in Figure 2.4, the wave-pattern artifacts dominated the water distribution contrast in ZTE MRI. The porous structures, which can be resolved by SE MRI (*cf.* Figure 2.4b), are not resolved by ZTE MRI with the use of acquired k-space origin (*cf.* Figure 2.4a).

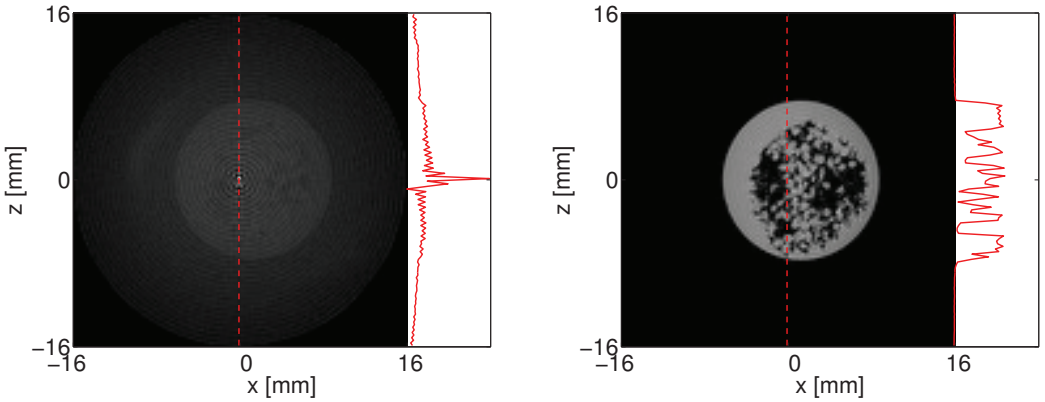

Figure 2.4: NMR images of a water-ceramic-cup sample measured by ZTE MRI (a) and SE MRI (b).

Further measurements showed that, even with a reduced BW_{acq} (down to $100KHz$) and a large oversampling factor (up to 8), the resulting complete k-space with the only missing point (*i.e.* the k-space origin) additionally acquired did not yield images with enhanced or reduced wave-pattern artifacts. Moreover, the same finding was observed in experiments on bulk water. This indicated that the missing points in the central k-space are unrelated to the wave-pattern artifacts.

2.3 Suppression of Background Signals

According to [19, 41], such wave-pattern artifacts may originate from *background signals* of NMR hardware surrounding the measured object. In most of the cases, such hardware refers to as the nearby RF coil inside the magnet and gradient system. And the background signals of the magnet and gradient system proved to be insignificant in this subproject and will be described in this section. Such background signals from the ^1H-containing RF coil or parts of it, which are outside the FOV, cause aliasing in the resulting NMR images. Due to rotational symmetry of the spiky k-space trajectories and often also of the RF coil, this aliasing results in radial or wave-like patterns. In this case, suppression of the background signals was validated and optimized. As investigated in preliminary studies and described in Section 2.2.2, the missing points are unrelated to the wave-pattern artifacts, hence were not additionally acquired but only algebraically compensated in all the remaining experiments of this subproject.

2.3.1 Saturating Slices in the Outer Volume

According to [19], in biomedical studies, the background signals can be suppressed by a first-order binomial preparation pulse (*i.e.* $90\,^\circ \sim -90\,^\circ$), since such signals decay with ultrashort T_2^*, which is typically much shorter than the measured object (tissues in most of the cases). However, in materials studies, T_2^* relaxation of the measured object is often comparably rapid as the background signals, and thus such separation strategy is inefficient.

Typically the RF coil is spatially separated from the measured object. Therefore, the *Outer Volume Suppression* (OVS) strategy [42], by which magnetization in slices outside the FOV is saturated by RF excitation and subsequent spoiler gradients, can be performed for background signal suppression. To suppress background signals of short T_1 components, such an OVS module for magnetization preparation is inserted at the beginning of each TR interval in ZTE MRI. This prolongs the minimum TR and thus increases the minimum measurement time. The pulse sequence was programmed in ParaVision 5.1, and implemented using the Bruker coil.

To examine the interpretation of the artifacts and also the feasibility of the OVS strategy, ZTE MRI was applied without any sample, *i.e.* ZTE MRI measurements were performed with only the Bruker coil inside the magnet and the gradient system. The measurement protocol except for the OVS module was as follows: BW_{acq} $150\,KHz$, no undersampling, number of half spokes 13030, TR $15.0\,ms$, NA 1, measurement time $3.26\,min$, rectangular pulse for excitation with α $4\,^\circ$ and t_p $2\,\mu s$, number of missing points per half

spoke 1.65, spoiling factor 1.5 $cycles/voxel$, switching gradients off in each TR interval, oversampling factor 2, dead time t_{dead} 6 μs, FOV $32 \times 32 \times 32\,mm^3$, matrix size $64 \times 64 \times 64$, voxel size $500 \times 500 \times 500\,\mu m^3$. 3D OVS was applied, *i.e.* two slices on both sides per orthogonal direction (along x-, y-, or z-axis, respectively) were saturated. Each saturated slice has a thickness d_{SS} of 80 mm and a slice position r_{SS} of $\pm 60\,mm$ for suppressing background signals from all surrounding NMR hardware including part of the magnet, the gradient system, and the RF coil. The hyperbolic pulse for saturation has an FA of $\alpha = 90\,^\circ$ and a duration of $t_p = 0.5\,ms$.

When the OVS module was switched off, the wave-pattern artifacts still existed even though there was no sample to be measured, as shown in Figure 2.5a. It is noteworthy that the artifacts here appeared as interfering waves of two point sources. With the OVS module switched on, the wave-pattern artifacts disappeared and only noise-level signals were detected, as shown in Figure 2.5b.

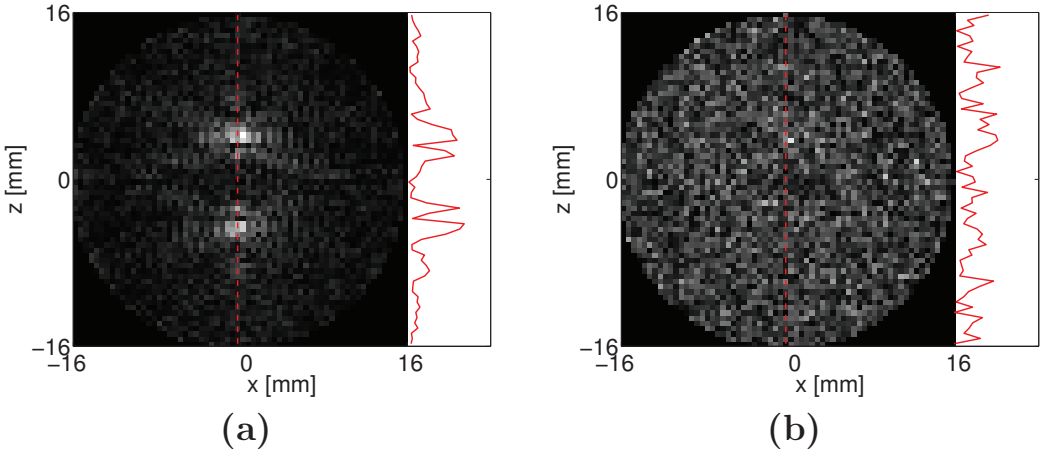

Figure 2.5: NMR images without any sample measured by ZTE MRI without OVS (a) and with OVS (b).

Experiments on bulk water led to the same finding. ZTE MRI was performed by the following protocol: BW_{acq} 150 KHz, no undersampling, number of half spokes 51896, TR 15.0 ms, NA 1, measurement time 12.97 min, rectangular pulse for excitation with α 4 $^\circ$ and t_p 2 μs, number of missing points per half spoke 1.65, spoiling factor 1.5 $cycles/voxel$, switching gradients off in each TR interval, oversampling factor 2, dead time t_{dead} 6 μs, FOV $64 \times 64 \times 64\,mm^3$, matrix size $128 \times 128 \times 128$, voxel size $500 \times 500 \times 500\,\mu m^3$, 3D OVS with d_{SS} 60 mm and r_{SS} $\pm 60\,mm$, hyperbolic pulse for OVS with α 90 $^\circ$ and t_p 0.5 ms. According to Figure 2.6, the wave-pattern artifacts were substantially suppressed by OVS.

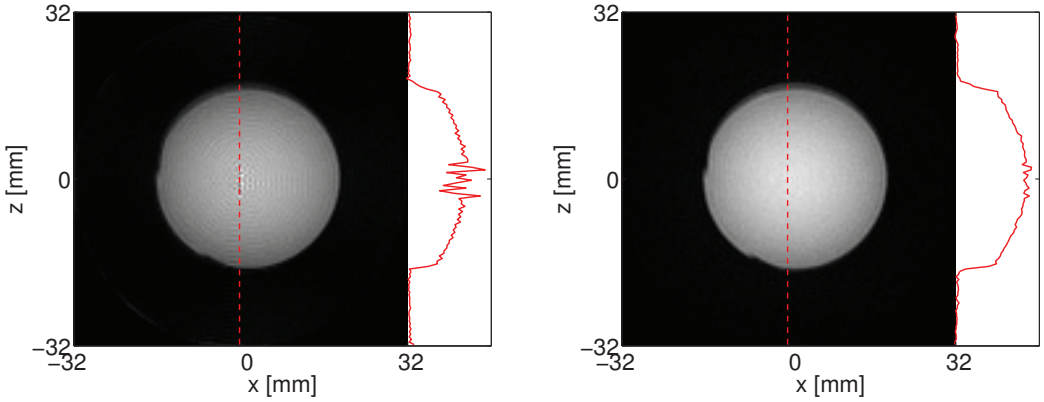

Figure 2.6: NMR images of bulk water measured by ZTE MRI without OVS (a) and with OVS (b).

The resulting ZTE NMR images (*cf.* Figure 2.6) indicate that the background signals from the surrounding NMR hardware cause the wave-pattern artifacts in ZTE MRI and can be suppressed by the inserted OVS preparation module. However, inserting such an OVS preparation module at the beginning of each TR interval prolongs the minimum TR with the module duration. Moreover, the usage of slice selection and spoiler gradients increases the *gradient duty cycle*, thus requesting a further increased TR for safety of the gradient system. Therefore, the OVS module should be optimized to find a compromise between the background signal suppression efficiency and the influence of prolonging measurement time, which will decrease the temporal resolution of serial ZTE MRI measurements.

ZTE MRI measurements with OVS were performed on a rubber sample (eraser, *cf.* Figure 2.7), in order to find out an OVS optimization routine. The measurement protocol except for the OVS parameters was as follows: BW_{acq} 150 KHz, no undersampling, number of half spokes 51896, TR 15.0 ms, NA 1, measurement time 12.97 min, rectangular pulse for excitation with α 4 ° and t_p 2 μs, number of missing points per half spoke 1.65, spoiling factor 1.5 $cycles/voxel$, switching gradients off in each TR interval, oversampling factor 2, dead time t_{dead} 6 μs, FOV $32 \times 32 \times 32\, mm^3$, matrix size $128 \times 128 \times 128$, voxel size $250 \times 250 \times 250\, \mu m^3$. The applied OVS parameters for each measurement are displayed in Table 2.1, and the corresponding ZTE NMR images are shown in Figure 2.8. It is noteworthy that the saturated slices overlaid only most parts of the Bruker coil with the given slice thickness d_{SS} and slice position r_{SS} in Table 2.1.

According to Figure 2.8b, OVS in the z-direction was regarded unneces-

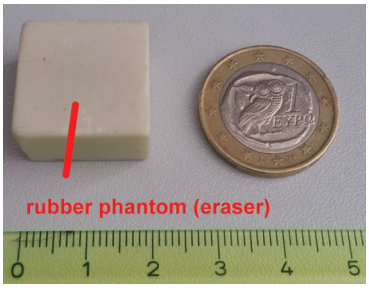

Figure 2.7: Photo of the rubber sample (eraser).

Table 2.1: OVS parameters for ZTE MRI measurements corresponding to NMR images in Figure 2.8.

subfigure	a	b	c	d	e	f
$d_{SS}\,[mm]$	no OVS	32				
$r_{SS}\,[mm]$		± 36				
slice dimension		2D (x and y)	2D (x and y)	1D (y)	2D (x and y)	1D (y)
α		90 °	45 °		30 °	
$t_p\,[ms]$		0.5				

sary, since the Bruker coil as a typical hollow cylindrical resonator is horizontal. This can substantially reduce the OVS module duration, *e.g.* to 2/3 in the cases of isotropic saturation. A reduced saturation FA ($\alpha < 90\,°$) can be used, *e.g.* 45 ° (*cf.* Figure 2.8c and 2.8d) or 30 ° (*cf.* Figure 2.8e and 2.8f). This allows a shorter OVS module duration and less RF heating. 1D OVS will decrease the background signal suppression efficiency in most of the cases due to the RF coil geometry (*cf.* less reduced wave-like patterns in Figure 2.8d and 2.8f compared to Figure 2.8c and 2.8e).

As shown in Figure 2.8, saturating only most parts of the RF coil can substantially reduce the wave-pattern artifacts. Note that OVS can even weaken the image intensities of the sample, particularly at the sample edges close to the sides of saturated slices (*cf.* Figure 2.8b). With a reduced saturation FA ($\alpha < 90\,°$), this SNR loss can be decreased (*cf.* Figure 2.8c and 2.8e). Thus, such drawback may not result from inefficient saturation of the magnet and gradient system. Instead, it was interpreted as consequences of partial saturation due to imperfect slice selection and/or *Magnetization Transfer* effects due to off-resonance saturation.

A practical solution may still be to saturate thick slices with their centers far away from the sample, not for saturating the magnet and gradient system but for shifting away the frequency band of the saturation pulse. Moreover,

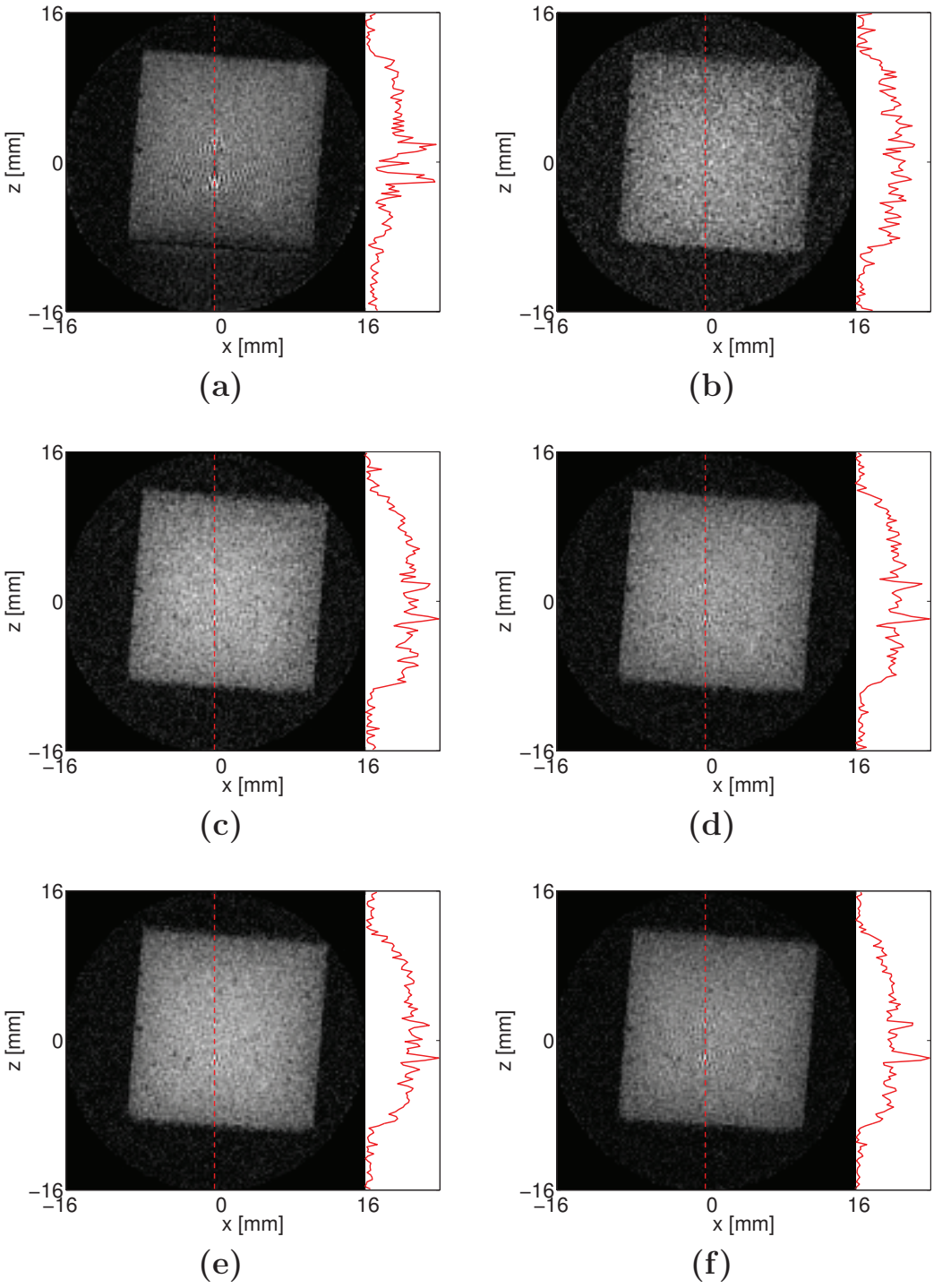

Figure 2.8: NMR images of the rubber sample measured by ZTE MRI (*cf.* Table 2.1) without OVS (a), with 90° 2D OVS (b), with 45° 2D OVS (c), with 45° 1D OVS (d), with 30° 2D OVS (e), and with 30° 1D OVS (f).

a large saturation d_{SS} is less demanding on the slice selection gradient magnitude. This scheme was applied in subsequent experiments on the identical rubber sample. ZTE MRI measurements were then performed with the following protocol: BW_{acq} $150\,KHz$, no undersampling, number of half spokes 13030, TR $15.0\,ms$, NA 1, measurement time $3.26\,min$, rectangular pulse for excitation with α $4\,^\circ$ and t_p $2\,\mu s$, number of missing points per half spoke 1.65, spoiling factor $1.5\,cycles/voxel$, switching gradients off in each TR interval, oversampling factor 2, dead time t_{dead} $6\,\mu s$, FOV $32 \times 32 \times 32\,mm^3$, matrix size $64 \times 64 \times 64$, voxel size $500 \times 500 \times 500\,\mu m^3$. The OVS parameters for each measurement are displayed in Table 2.2, and the corresponding ZTE NMR images are shown in Figure 2.9.

Table 2.2: OVS parameters for ZTE MRI measurements corresponding to NMR images in Figure 2.9.

subfigure	a	b	c	d
$d_{SS}\,[mm]$	no OVS	80		
$r_{SS}\,[mm]$		± 60		
slice dimension		2D (x and y)		
α		$90\,^\circ$	$45\,^\circ$	$30\,^\circ$
$t_p\,[ms]$		0.5		

Results (*cf.* Figure 2.9) showed that when a large region outside the FOV was saturated, the wave-pattern artifacts were substantially reduced without affecting the image intensities of the sample. $45\,^\circ$ was then determined as the optimal saturation FA for a compromise between the saturation efficiency and the shortcomings of the OVS module, which include increased RF heating and prolonged minimum TR.

With the empirically optimized OVS module, ZTE MRI can efficiently suppress the background signals and the corresponding wave-pattern artifacts. An example is given in Figure 2.10, showing results of the measurements on another water-ceramic-cup sample with the following protocol: BW_{acq} $150\,KHz$, no undersampling, number of half spokes 13030, TR $15.0\,ms$, NA 1, measurement time $3.26\,min$, rectangular pulse for excitation with α $4\,^\circ$ and t_p $2\,\mu s$, number of missing points per half spoke 1.65, spoiling factor $1.5\,cycles/voxel$, switching gradients off in each TR interval, oversampling factor 2, dead time t_{dead} $6\,\mu s$, FOV $32 \times 32 \times 32\,mm^3$, matrix size $64 \times 64 \times 64$, voxel size $500 \times 500 \times 500\,\mu m^3$, 2D OVS with d_{SS} $80\,mm$ and r_{SS} $\pm 60\,mm$, hyperbolic pulse for OVS with α $45\,^\circ$ and t_p $0.5\,ms$.

To summarize, the inserted OVS module for magnetization preparation in ZTE MRI can efficiently suppress the background signals from the sur-

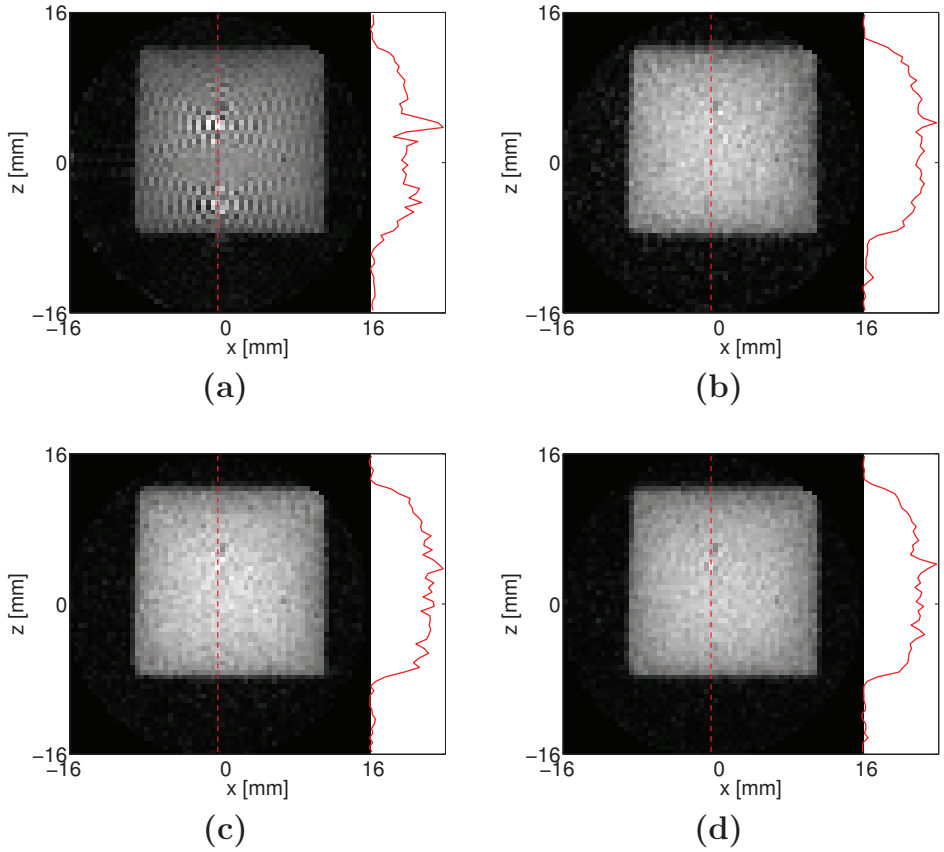

Figure 2.9: NMR images of the rubber sample measured by ZTE MRI (*cf.* Table 2.2) without OVS (a), with 90° 2D OVS (b), with 45° 2D OVS (c), and with 30° 2D OVS (d).

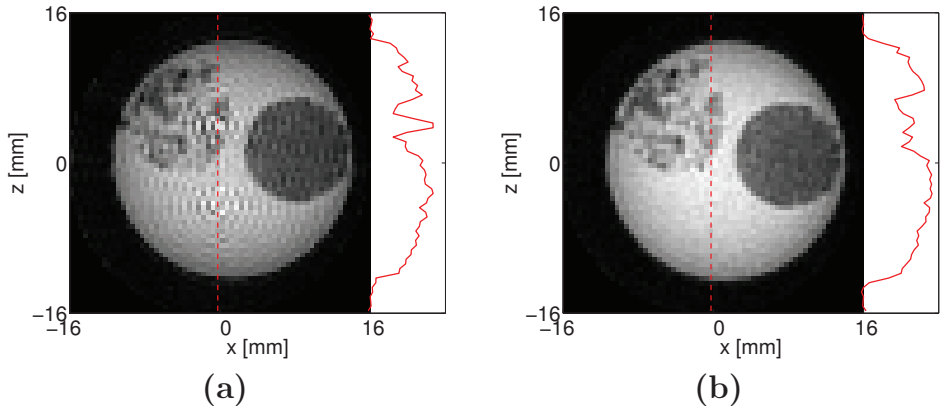

Figure 2.10: NMR images of a water-ceramic-cup sample measured by ZTE MRI without OVS (a) and with empirically optimized OVS (b).

rounding NMR hardware, mainly the RF coil, and thus can reduce the wave-pattern artifacts. However, the compromise between the suppression efficiency and the drawbacks of the OVS module (including a prolonged minimum TR and increased RF heating) was only empirically achieved. Several implicit limitations exist in optimizing the OVS module. Firstly, saturation is expected in the spatial region with inhomogeneous $\boldsymbol{B}_0$ and $\boldsymbol{B}_1$ as well as nonlinear gradients, and thus systematic optimization of the OVS module requires corresponding field measurements and associated calibrations. Secondly, substantially increased RF power may result in unwanted heating of the measured object, which requires additional measures, *e.g.* temperature, for systematic optimization of the OVS module. In the future, dual-band RF pulses can be used in the OVS module to further reduce the module duration, the deposited RF power, and the gradient duty cycle.

2.3.2 Using an Optimized RF Coil

Due to the limitations of the OVS strategy in ZTE MRI, a ^1H-free RF coil may be a better solution. A dedicated horizontal 38 mm-bore LitzCage ^1H quadrature transceiver RF coil (Doty Scientific, USA) was purchased and used in this subproject. It is called Doty coil in the rest of the thesis (*cf.* Figure 2.11). The most important feature of this RF coil is that the coil body was made of PTFE and other ^1H-free materials, which are NMR-insensitive. Additionally, compared to the Bruker coil (*cf.* Figure 2.11), the Doty coil has a smaller bore and thus higher RF efficiency for a better SNR.

ZTE MRI of drying was then applied to water within a porous ceramic as an exemplary study. The porous ceramic with a mean pore size of 0.56 mm was saturated with distilled water as described in Section 2.2.1, taken out of the cup, and positioned directly on a PTFE plate inside the Doty coil. A series of *in situ* ZTE MRI measurements was performed to observe temporal changes of water within the pores.

Since the Doty coil is regarded as ^1H-free in MRI measurements, the OVS module was omitted. The measurement protocol was as follows: BW_{acq} 150 KHz, no undersampling, number of half spokes 51896, TR 5.0 ms, NA 2, measurement time 8.65 min, rectangular pulse for excitation with α 5 ° and t_p 2 μs, number of missing points per half spoke 1.65, spoiling factor 1.5 $cycles/voxel$, switching gradients off in each TR interval, oversampling factor 2, dead time t_{dead} 6 μs, FOV $25 \times 25 \times 25\, mm^3$, matrix size $128 \times 128 \times 128$, voxel size $195 \times 195 \times 195\, \mu m^3$, fifteen measurements in total with the first inter-measurement delay of 20 min and other inter-measurement delays of 60 min.

According to [27, 28], ZTE NMR images are predominantly spin density

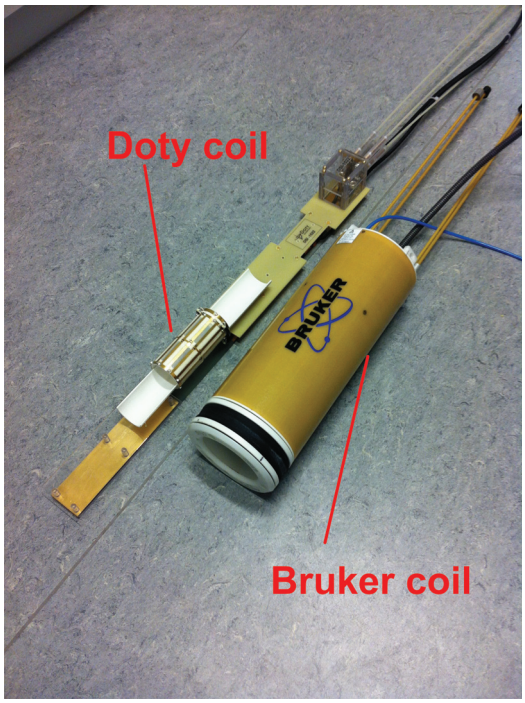

Figure 2.11: Photo of the Doty coil and Bruker coil.

weighted. Hence, image intensity variations in a dataset of ZTE NMR images were assumed to be dominated by the partial occupation of voxels by water. The data post-processing procedures including image processing and quantitative analysis of drying were performed as follows:

1. All datasets of ZTE NMR images were normalized to the maximum image intensity in the first dataset.

2. Binary masking was applied on the first dataset of ZTE NMR images by the Otsu's thresholding algorithm [43] for selection of the pore regions and generation of the image threshold.

3. Voxels with image intensities under the image threshold were considered as water-free, and thus their image intensities were set to be zero.

4. Two types of voxel counts were calculated. The first type was the counts of water-containing voxels in the pore regions defined by the binary mask. And the second type of voxel counts was the voxel counts of the first type additionally weighted by the image intensities of voxels.

5. Fitting by model functions, *e.g.* an exponential decay, was used to find out the drying characteristics.

ZTE NMR images of the first twelve datasets with normalization, masking and hard thresholding (*cf.* step 1, 2 and 3 in the data post-processing procedures, respectively) are shown in Figure 2.12. No wave-pattern artifacts can be observed, reflecting that the background signals in previous experiments originated mainly from the Bruker coil. As a consequence, substantial reduction of water within pores can be measured over time. Water in the spatially lower region evaporated slower than in the spatially upper region, because the bottom of the ceramic was blocked by the PTFE plate. It is revealed that several pores in the spatially upper region adsorbed water for a longer duration than other pores nearby, and the vast majority of water has evaporated after about $11\,h$ (*cf.* Figure 2.12l).

As shown in Figure 2.13, both types of voxel counts reveal an exponential decay. Regression coefficients of both fitting are 0.899 and 0.930, respectively. The drying characteristic times were $t_c = 8.0\,h$ and $t_c^{(w)} = 6.4\,h$, respectively. Under the consideration of partial volume effects and the agreement with the observed total drying after about $11\,h$, the weighted counts were regarded as more reasonable estimation means. Such a drying rate implies that an NMR measurement time no longer than several minutes is necessary for appropriate temporal resolution in drying studies.

This exemplary study indicated the feasibility of monitoring the drying process in porous materials by ZTE MRI using a ^1H-free RF coil for background signal suppression with promising temporal resolution. In the future, controllable drying processes can be studied by combining ZTE MRI and other characterization technologies like weight monitoring for further cross-validation of the proposed ZTE MRI method.

2.4 Conclusion

In this subproject, the wave-pattern artifacts in ZTE MRI was found to be unrelated to the missing points in the central k-space, and proved to originate mainly from the background signals of the ^1H-containing RF coil. Two strategies were applied to suppress the background signals and thus remove unwanted image artifacts with wave-like patterns. The first strategy was saturating slices in the outer volume for magnetization preparation, and the second strategy was the use of a ^1H-free RF coil. When such an optimized RF coil is available, the second strategy is preferable for avoiding limitations of the OVS module, such as increased RF heating and gradient duty cycle, as well as prolonged measurement time. The OVS part (*cf.* Section 2.3.1) of this subproject was published as part of a journal contribution [44], and the drying studies using the optimized ^1H-free RF coil (*cf.* Section 2.3.2) was

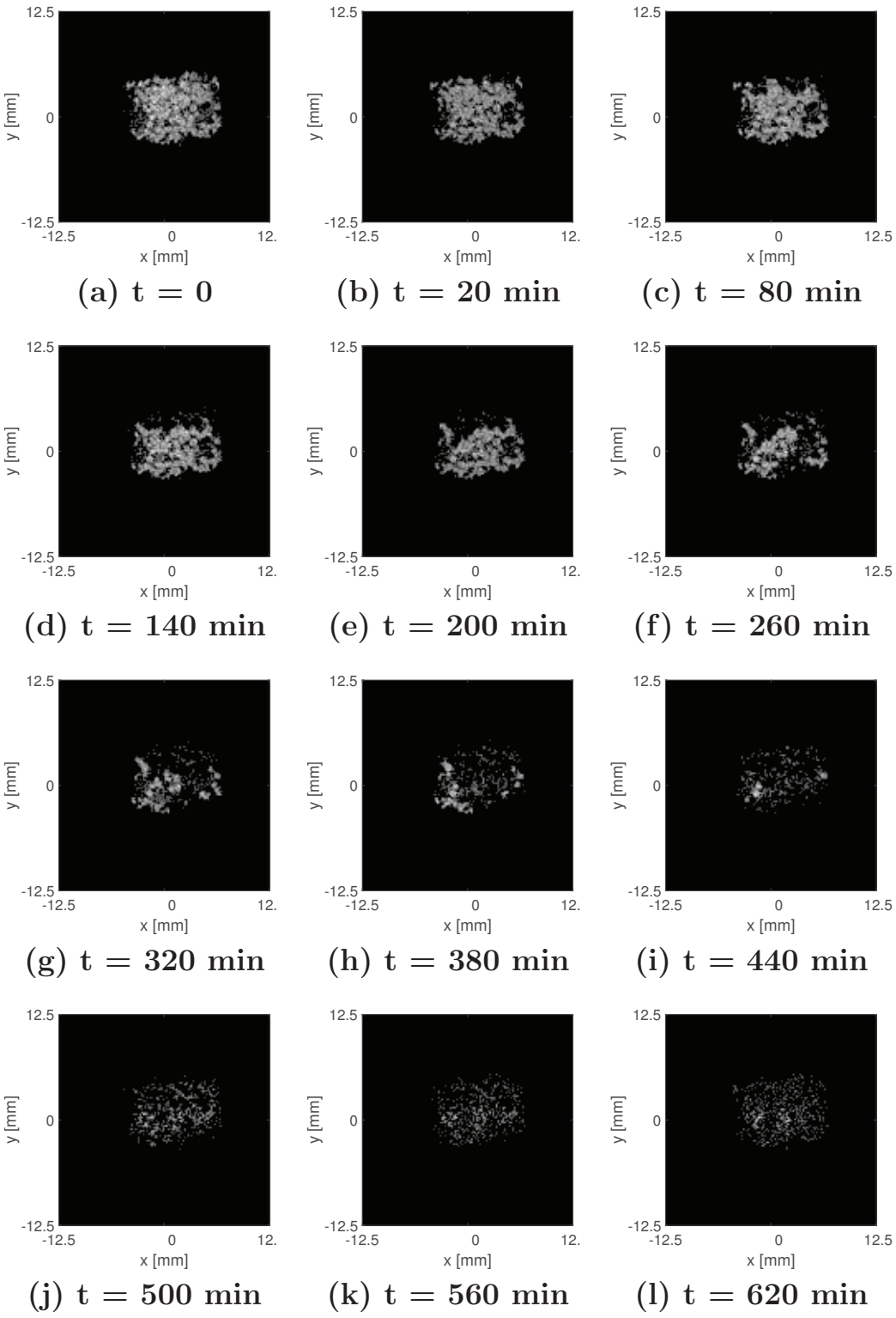

Figure 2.12: Serial ZTE NMR images of water within pores. Images were normalized, masked and hard thresholded (*cf.* step 1, 2 and 3 in the data post-processing procedures, respectively).

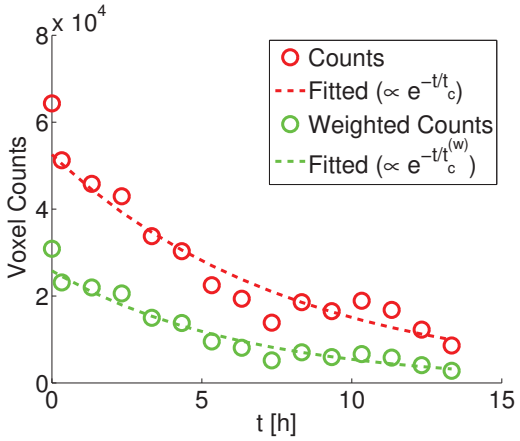

Figure 2.13: Evolution of water in a porous ceramic.

presented as a conference contribution [45].

In studies on fast drying systems, further acceleration methods, such as *Compressed Sensing* [46, 47], may be used for improved temporal resolution. In the future, ZTE MRI may also be used for other applications, such as monitoring liquid uptake in porous materials. With certain limitations like a centered *FOV* encompassing the whole object to be measured, these studies can still benefit from the major advantages, particularly: (i) high 3D spatial resolution with short or moderate measurement time; (ii) minimized T_2^* contrast and predominant spin density contrast.

Chapter 3

Accelerated PC-MRI of Slow Liquid Flow

3.1 Introduction

Deep bed filtration [48, 49, 50, 51, 52] is a separation process with the aim of clarifying a liquid. To this end, the liquid with suspended solid particles is slowly streaming downwards through the porous filter with local velocities of submillimeters to millimeters per second. Two groups of mechanisms underlie the filtration process, one leads to routes of particles towards interfaces between the liquid and the porous filter (*e.g.* gravity settling, diffusion, interception), and the other causes immobilization of particles at the filter surfaces (Van-der-Waals and electrostatic forces, straining). Due to the large amount of particles which can be retained and the slow increase of pressure drop, deep bed filtration is widely used in industrial applications, such as wastewater treatment and desalination [51, 52].

Recent studies [53, 54, 55, 56, 57, 58, 59, 60, 61] have shown the potential of XMT for characterizing the particle deposition processes. With 3D spatial resolution in the micrometer to submillimeter range, serial XMT images of porous structures and deposited particles can provide microscopic knowledge of the particle deposition processes.

While the correlation between the particle deposition processes and the velocity fields of the flowing liquid has been studied for other filtration processes [62, 63, 64], this correlation has not been studied yet for deep bed filtration. Insights into this correlation will certainly lead to a more profound understanding of deep bed filtration mechanisms and thus an improved design of deep bed filters with regard to filtration efficiency. Quantifying the velocity fields of the liquid can be achieved by spatially resolved NMR Velocimetry

[65, 66]. This technique is particularly suitable for opaque structures, for which optical velocimetry techniques cannot be applied. Spatially resolved NMR Velocimetry is a highly versatile tool for velocity mapping of fluid flow, since it contains a variety of adaptable methods for laminar and turbulent, single-phase and multi-phase, fast and slow flow [65, 66]. For the specific case of deep bed filtration, dedicated spatially resolved NMR Velocimetry is required for measuring slow liquid flow of submillimeters to millimeters per second in macroporous materials with 3D sub-pore-scale spatial resolution. Additionally, this spatially resolved NMR Velocimetry method should allow an adequate measurement time, because the velocity fields of the liquid can alter significantly due to substantial changes of pore filling after a few hours of filtration.

Spatially resolved NMR Velocimetry can be achieved by adding a displacement encoding module to a standard MRI pulse sequence. There are two main methods, q-space MRI [67] and PC-MRI [68, 69, 70]. In q-space MRI, the probability distribution of fluid displacements is spatially resolved as the voxel-wise propagator spectra. In PC-MRI, the voxel-wise average propagator is directly measured to provide the average fluid displacement within each voxel. For instance, a simplest implementation of 1D velocimetry in PC-MRI is performing two measurements with $+\boldsymbol{q}$ and $-\boldsymbol{q}$, and then extracting the average displacement in the direction parallel to $\boldsymbol{q}$ using division of the displacement introduced phase contrast by $2q$. Though inferior in velocimetry accuracy to q-space MRI, PC-MRI is widely used due to the much smaller number of required displacement encoding steps, leading to a shorter minimum measurement time.

In PC-MRI, the SNR of the complex-valued NMR images is not only a measure of image quality, but also determines the accuracy of measured velocity maps, because the *STandard Deviation* (STD) of the velocities is reciprocally proportional to the SNR [71, 72, 73]. Therefore, PC-MRI methods using an SE based magnetization preparation module for velocity encoding are superior to those using an STE based magnetization preparation module, because the latter implies a general signal loss of 50 %.

Spatially resolved NMR Velocimetry can be accelerated by different methods, *e.g.* Compressed Sensing, Bayesian NMR, and *Parallel Imaging* [66]. Another strategy with respect to MRI pulse sequence design is the use of *Rapid Acquisition with Relaxation Enhancement* (RARE) method [74], *i.e.* multiple echoes after single excitation for multiple phase encoding steps (usually with a certain number called *RARE factor*). RARE is a reasonably fast spatially resolved NMR Velocimetry approach [75, 76, 77, 78, 79, 80, 81, 82, 83, 84] and has been applied for displacement mapping of liquid in porous systems like plants [75, 76] and rocks [84].

A recent study [84] showed that RARE PC-MRI with 3D super-pore-scale spatial resolution can still be accurate for very slow liquid flow in porous materials. However, the implementation of the method in [84] was not considered optimal for this subproject. First, a specific STE based magnetization preparation module [85] was used in [84] due to very small velocities of sub-millimeters per second and strong internal magnetic field gradients within each super-pore-scale voxel, while an SE based magnetization preparation module can be used in this subproject to improve the SNR because of relatively larger velocities and weaker internal magnetic field gradients within each sub-pore-scale voxel. Second, a rather small RARE factor (2) and thus a short echo train length were used in that study due to short T_2 in rocks, while longer T_2 in deep bed filters allows a larger RARE factor. However, several additional strategies need to be considered for velocimetry accuracy with a relatively longer echo train length, such as RF filter pulses [81] or phase cycling [80, 83] for recovering the correct complex-valued signals, as well as phase encoding *winder and rewinder* gradients for suppressing motion artifacts.

In this subproject, an efficient and accurate RARE PC-MRI approach for slow liquid flow in porous materials was achieved. For SNR reasons and due to a moderate velocity range to be measured, an SE based velocity encoding module was used. A two-step phase cycling containing *Carr-Purcell* (CP) and *Carr-Purcell-Meiboom-Gill* (CPMG) pulse trains [80, 83] was applied to preserve the propagator information within the magnetization in the echo train. Velocity offsets caused by gradient imperfections [86, 87, 88] were measured with zero flow for correcting the velocity maps of the flowing liquid. Velocity maps of odd and even echoes in the echo train were combined to increase velocimetry accuracy. The proposed RARE PC-MRI approach can be a helpful tool for improving the understanding of deep bed filtration and may also be of interest for further spatially resolved NMR Velocimetry applications.

3.2 Methodological Preparation

Before the implementation and optimization of RARE PC-MRI as well as the desired combination with XMT, three procedures as methodological preparation were executed. First, a reliable and efficient phase unwrapping algorithm was selected to unfold possible phase fold-over in PC-MRI. Second, the experimental setup containing a home-made RF coil for a vertical filtration cell and a flow system was developed and tested. Third, an empirically optimized image registration routine was determined for combining the NMR velocity

maps and XMT images.

3.2.1 Phase Unwrapping

Phase wrapping may take place in PC-MRI where the displacement introduced phase contrast between q-space points exceeds 2π. Phase wrapping can only be avoided by carefully choosing q-space step length based on prior knowledge of the measured flow. Therefore, phase unwrapping is necessary in this subproject, because such prior knowledge of the expected maximum velocity is not always available.

A phase map (128×128) with a wrapped phase region (*cf.* Figure 3.1a) was used for comparison of three representative phase unwrapping algorithms: the Laplacian method [89] as a whole-image approach, the best-path method [90] as a voxel-wisingle SE PC-MRI method, and the best-pair-first region merging method [91] as a region-wise method. The first two methods were programmed in Matlab R2014a, while the third method was performed by directly calling the PRELUDE function in the FSL 5.0 toolbox (Oxford Center for Functional MRI of the Brain, UK). As shown in Figure 3.1, the Laplacian method can sometimes produce incorrect phase regions (*cf.* Figure 3.1b), while the best-path (*cf.* Figure 3.1c) and best-pair-first region merging methods (*cf.* Figure 3.1d) can correctly unwrap the wrapped phase. The best-pair-first region merging method, which can be completed in several minutes for 3D images ($128 \times 128 \times 128$), proved to have much less computational cost than the best-path method, which took approximately $1\,min$ for a single slice (128×128) and more than linearly increasing computation time for multiple slices in 3D images ($128 \times 128 \times 128$). Therefore, the best-pair-first region merging method was selected in this subproject.

Note that the basis of phase unwrapping is edge detection on images, and therefore high spatial resolution is necessary for correctly solve the problems of phase fold-over. In this subproject, sub-pore-scale voxel size was always used, and thus possible edge detection errors were regarded as negligible.

3.2.2 Flow Setup and Home-made RF Coil

Distilled water was used as the liquid flowing through the sample. The sample was mounted in a dedicated filtration cell made of PTFE (*cf.* Figure 3.2). The inlet and outlet in the filtration cell have an inner diameter of about $8\,mm$. The filtration cell was connected to a peristaltic tubing pump (ISMATEC REGLO Analog MS-2/6, Cole-Parmer, Germany) by tubes. The pump permits steady liquid flow through the filtration cell with the linearly controllable *Volumetric Flow Rate* (VFR) between $1.26\,mm^3/s$ and

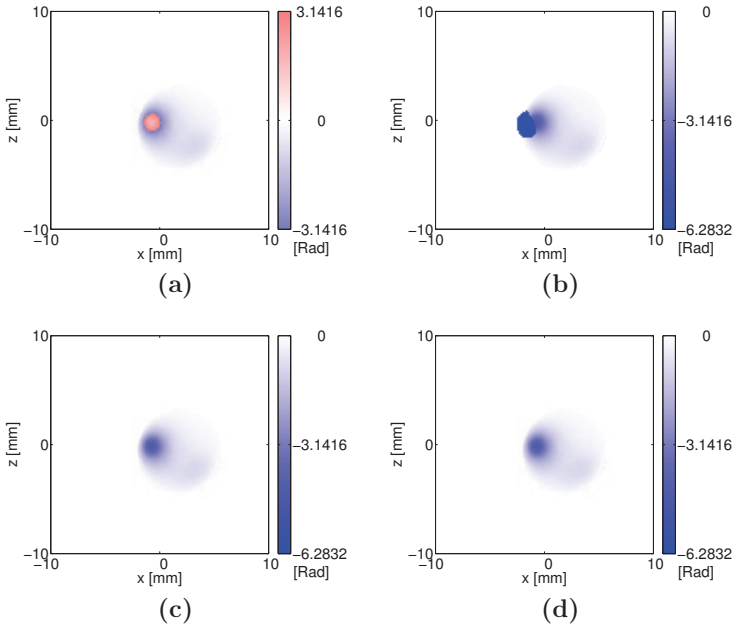

Figure 3.1: A phase map (128 × 128) with a wrapped phase region (a) unwrapped by the Laplacian method (b), the best-path method (c), and the best-pair-first region merging method (d).

$125\,mm^3/s$. The linearity and the VFR range were measured by monitoring the volume of the distilled water flowing out of the filtration cell. Due to the long tube length between the pump and the filtration cell ($> 3\,m$), the pulsation effect of the peristaltic pump is regarded as negligible. Note that the VFR range may differ if the connecting tubes are replaced by tubes of different materials and/or inner diameters. In this subproject, the connecting tubes remained unchanged. Before NMR experiments, the filtration cell was soaked in the distilled water in the bottom part of a desiccator to achieve pore pre-saturation, and then the desiccator was sealed and evacuated from the top by a vacuum pump for pore saturation. Due to the low pressure, remaining gas within the pores degassed and the pores were eventually saturated.

Due to the vertically orientated filtration in deep bed filters, a vertical NMR scanner would certainly be a good choice. However, the drawback of limited vertical space available in a horizontal NMR scanner with a horizontal RF coil was reduced by using a home-made, vertically orientated RF coil. This dedicated coil consists of two identical thin rectangular copper plates fixed on the outer surface of a hollow cylinder resulting in a loop-gap resonator. A fixed-value capacitor was soldered on one gap and a trimmer

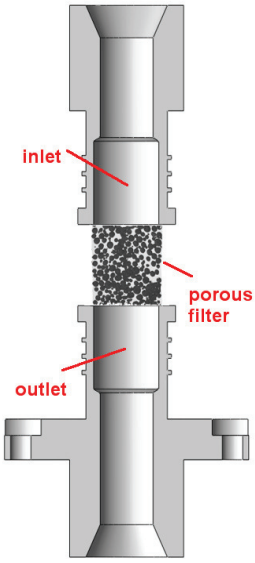

Figure 3.2: The design of the dedicated filtration cell. Reproduced by the collaborator (Gerd Mikolajczyk).

capacitor on the other gap to link the two copper plates. A pick-up loop covering the resonator bore was mounted on a slider, which supports the movement of the pick-up loop along the longitudinal direction of the loop-gap resonator. Tuning and matching of this linear transceiver RF coil is performed by adjusting the trimmer capacitor and sliding the pick-up loop longitudinally, respectively.

Figure 3.3 and 3.4 shows the first and the final versions of the home-made RF coil, respectively. The first version (*cf.* Figure 3.3) was built for feasibility tests of the coil design. In the first version, the cylindrical resonator body and the pick-up loop slider were tailored plastic syringes, and fixed with tapes and papers. The first version proved to have higher transmission efficiency than the Bruker coil by providing about twice the B_1 field strength with the same current magnitude. Afterwards, the final version (*cf.* Figure 3.4) was produced in the Workshop of Faculty 02 (Biology/Chemistry), University of Bremen. In the final version, the cylindrical resonator body and the pick-up loop slider were made of PTFE. Such ^1H-free materials with suppressed NMR background signals could have been replaced by other ^1H-containing materials for SE based PC-MRI in this subproject, but were still used in manufacturing so that the mostly ^1H-free home-made RF coil will have better performances in other applications such as ZTE MRI (*cf.* Chapter 2). Moreover, supporting structures including slots, driving screws, and

distance rings can increase the mechanical stability of the home-made RF coil. In order to achieve high RF efficiency and SNR, the filling factor of the home-made RF coil was maximized by adapting the resonator diameter to the filtration cell diameter. Figure 3.5 shows how the filtration cell is mounted in the home-made RF coil and connected to the pump (not shown in Figure 3.5) by tubes before being inserted into the NMR scanner.

The home-made RF coil used in this subproject has a diameter of 22 mm and a height of 25 mm. B_1 mapping by the *Double Angle Method* [92] was performed on a static water phantom with the maximum filling factor of the home-made RF coil. Across the expected FOV, which is the central region in the filtration cell, the B_1 inhomogeneity of the home-made RF coil was shown to range from $-57\,\%$ to $+14\,\%$ (*cf.* Figure 3.6). For comparison and initial methodological developments, some NMR experiments were performed using the Bruker coil.

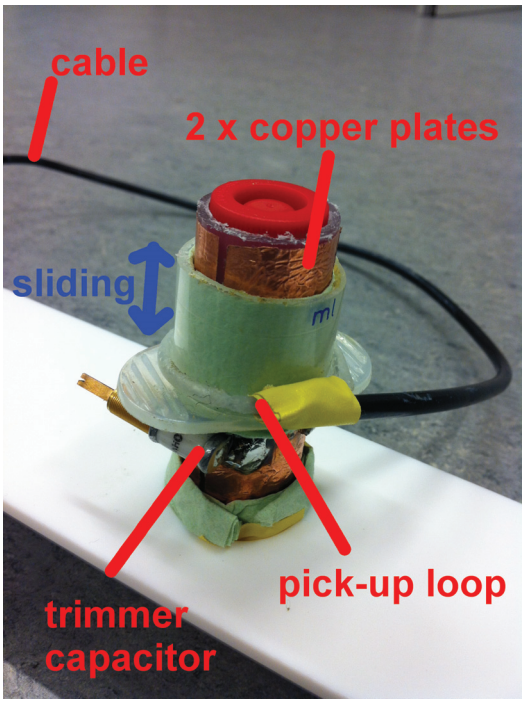

Figure 3.3: The first version of the home-made RF coil.

3.2.3 Image Registration

For the desired combination with XMT, image registration was tested on a dedicated sample, which was made by attaching three glass tubes filled with

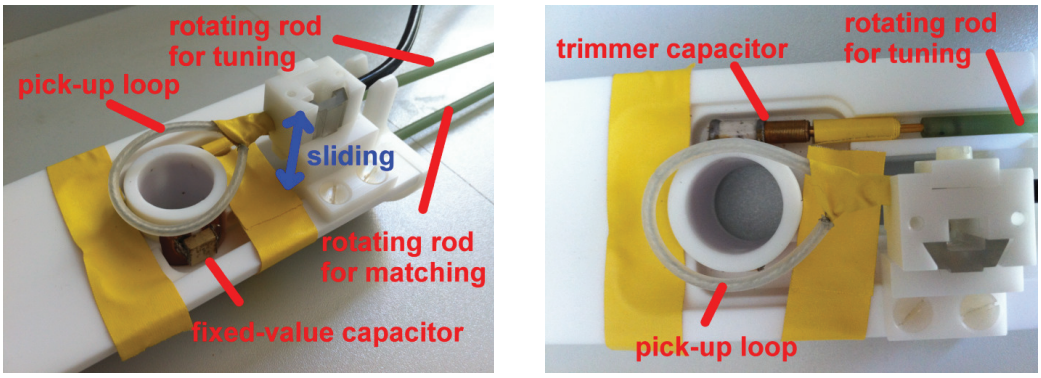

(a) (b)

Figure 3.4: The final version of the home-made RF coil in two different views (a) & (b).

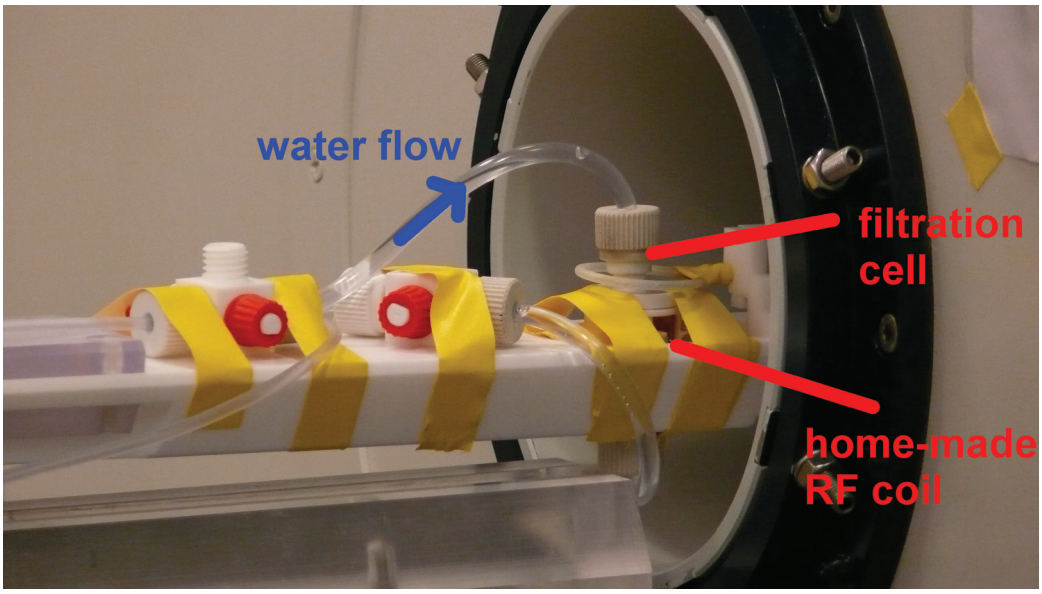

Figure 3.5: The filtration cell mounted in the home-made RF coil and connected to the pump (not shown) by tubes before being inserted into the NMR scanner.

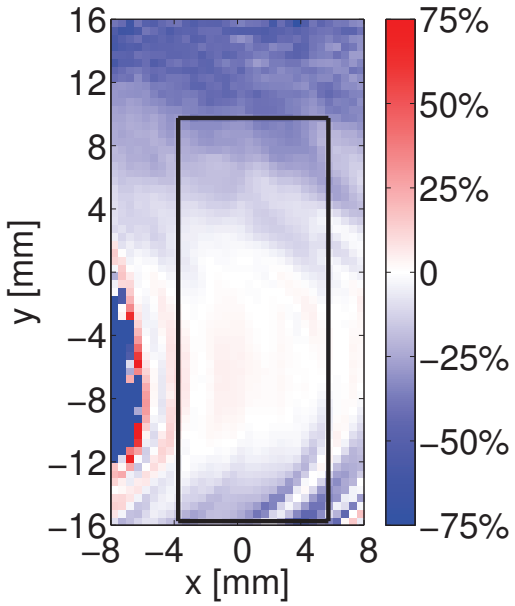

Figure 3.6: B_1 map of the central xy-slice in a static water phantom acquired by Double Angle Method using the home-made RF coil.

gelatin as registration fiducials to the side wall of a porous ceramic cylinder (*cf.* Figure 3.7) with tapes. The collaborator (Gerd Mikolajczyk) performed the XMT measurements on the sample with matrix size $1024 \times 1024 \times 781$ and voxel size of $16.5 \times 16.5 \times 16.5\,\mu m^3$ by using a home-made XMT scanner [93] in the Chair of Magnetofluiddynamics, Measuring and Automation Technology, Institute of Fluid Mechanics, Technical University of Dresden. The sample was then soaked in distilled water, placed vertically (*i.e.* along the y-axis), and measured by 3D SE MRI with the following protocol: rectangular RF pulses, TE $6.0\,ms$, FOV $32 \times 32 \times 32\,mm^3$, matrix size $256 \times 256 \times 256$, read direction z, slice direction y, voxel size $125 \times 125 \times 125\,\mu m^3$, TR $0.3\,s$, NA 4, measurement time $21.85\,h$.

Image registration was performed in Slicer 4.4, as shown in Figure 3.8. XMT images highlight hard matter in the sample such as the porous ceramic, the glass tubes, and the tapes for attaching (*cf.* Figure 3.8a), while NMR images highlight soft matter such as the distilled water inside and outside the porous ceramic, and the gelatin in the glass tubes (*cf.* Figure 3.8c). Image registration by registering NMR images (low spatial resolution) to XMT images (high spatial resolution) was performed according to the following procedures:

1. For reduction of computational cost on the dataset of XMT images

Figure 3.7: Photo of the sample dedicated for image registration tests. The sample was made by attaching three glass tubes filled with gelatin as registration fiducials to the side wall of a porous ceramic cylinder.

with a size of 3.12 $GBytes$, an additional dataset of the XMT images was generated by subsampling with a factor of 2 in three orthogonal directions, thus reducing the dataset size to 391 $MBytes$.

2. Binary masks overlaying the sample were generated by the GrowCut algorithm [94] (*cf.* Figure 3.8b and 3.8d).

3. An initial transform (translation and rotation) of NMR images was manually determined by overlapping the corresponding mask on the mask of subsampled XMT images.

4. In the semi-automated registration module "BRAINS" with the labeled and subsampled XMT images as well as the labeled and initially transformed NMR images, registration parameters were empirically optimized: affine registration, maximum iterations 1500, linear interpolation, minimum step length 0.001.

Two exemplary screenshots of registration results are shown in Figure 3.8e and 3.8f, respectively. Each screenshot contains manually selected regions of interest (blue labeled) in identical position in XMT images (left), transformed NMR images (middle), and registered NMR images (right). Those regions of interest in the porous ceramic with low image intensities in NMR images correspond to bounded beads with low local porosities, as revealed in XMT images. Meanwhile, the regions of interests overlaying the glass tubes agree with each other in all three datasets of images (*cf.* Figure 3.8e). The test verified the feasibility of image registration with the given fiducials and the empirically optimized software module.

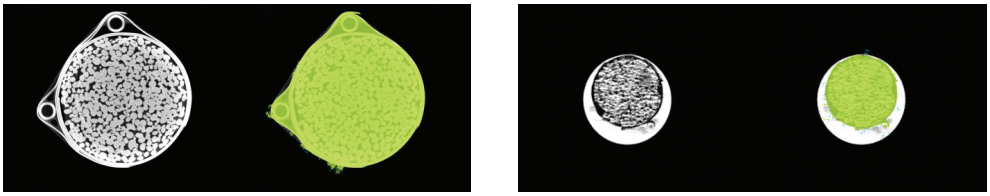

(a) (b) (c) (d)

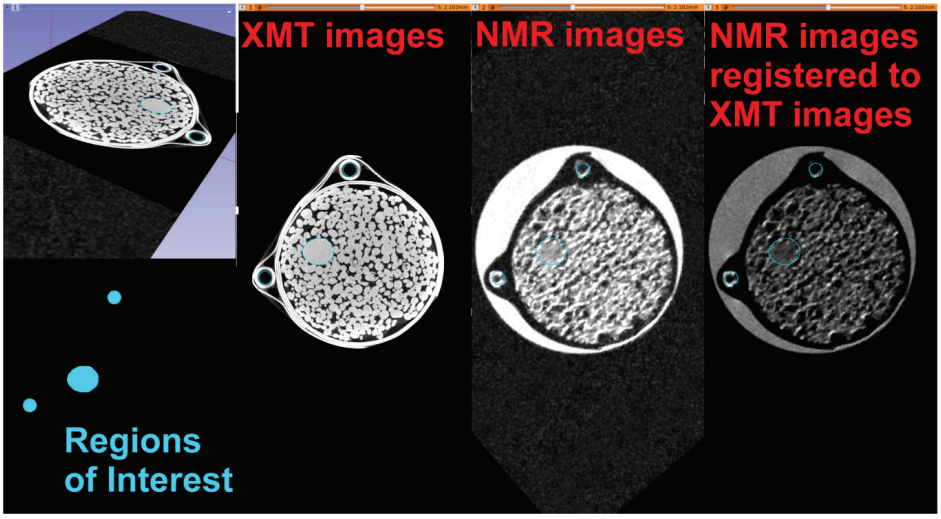

(e)

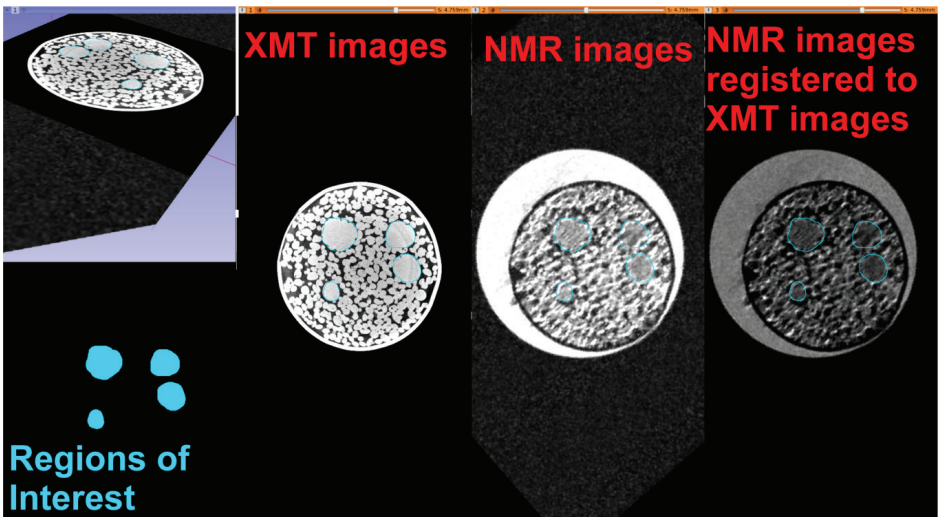

(f)

Figure 3.8: XMT image (a) with a binary mask (b). NMR image (c) with a binary mask (d). Two exemplary screenshots of image registration results (e) & (f). NMR images (low spatial reoslution) were registered to XMT images (high spatial resolution).

3.3 Accelerated PC-MRI Method

Several means were applied to optimize the RARE PC-MRI pulse sequence with a long echo train for accurately measuring the phase contrast, even in the case of a low B_1 homogeneity. Two means are of particular importance. One uses data acquired with zero flow to correct the phase contrast offsets originating from gradient imperfections, and the other combines the phase contrast from signals of both odd and even echoes.

3.3.1 Pulse Sequence and Data Post-processing

The proposed pulse sequence, which was implemented in ParaVision 5.1, is schematically shown in Figure 3.9, where G_{VE} is the magnitude of the velocity encoding gradient, t_δ is the duration of the velocity encoding gradient, and t_Δ is the delay between the velocity encoding gradients. A velocity encoding module with a pair of unipolar gradients separated by a refocusing pulse is placed after the excitation pulse for magnetization preparation. The velocity encoding gradients can be applied in arbitrary direction. By inverting the polarity of the velocity encoding gradients, displacements are encoded into the phase of the NMR signals. For 3D velocimetry, an Hadamard scheme [95, 96] defines the polarities of velocity encoding gradients in three orthogonal directions, as shown in Table 3.1. The velocity encoding range is defined as $[-VENC, VENC]$, where the *Velocity ENCoding* ($VENC$) is given by

$$VENC = \frac{\pi}{N_{VE}\gamma G_{VE} t_\delta t_\Delta} \tag{3.1}$$

with the number of velocity encoding steps N_{VE} (2 for 1D velocimetry and 4 for 3D velocimetry with the Hadamard scheme). Note that for velocity encoding of slow liquid flow a large value of t_Δ is required considering the limited maximum gradient magnitude. The echo after the first refocusing pulse in the preparation module at $t = 2\tau$ (not shown in Figure 3.9) will not be formed if the second velocity encoding gradient is not applied before $t = 2\tau$, and therefore this echo is not acquired. A subsequent RARE MRI module is used for fast spatial encoding. Pairs of balanced *crusher* gradients around all refocusing pulses are used to suppress unwanted coherence pathways.

Within each inter-refocusing interval, zeroth-order *gradient moment* [2] nulling is applied by performing spatial decoding after spatial encoding and acquisition. This scheme suppresses image artifacts due to spin motion in the echo train, with only slightly increased minimum TE. Centric phase encoding is used for higher SNR and lower T_2 contrast than obtained by linear phase

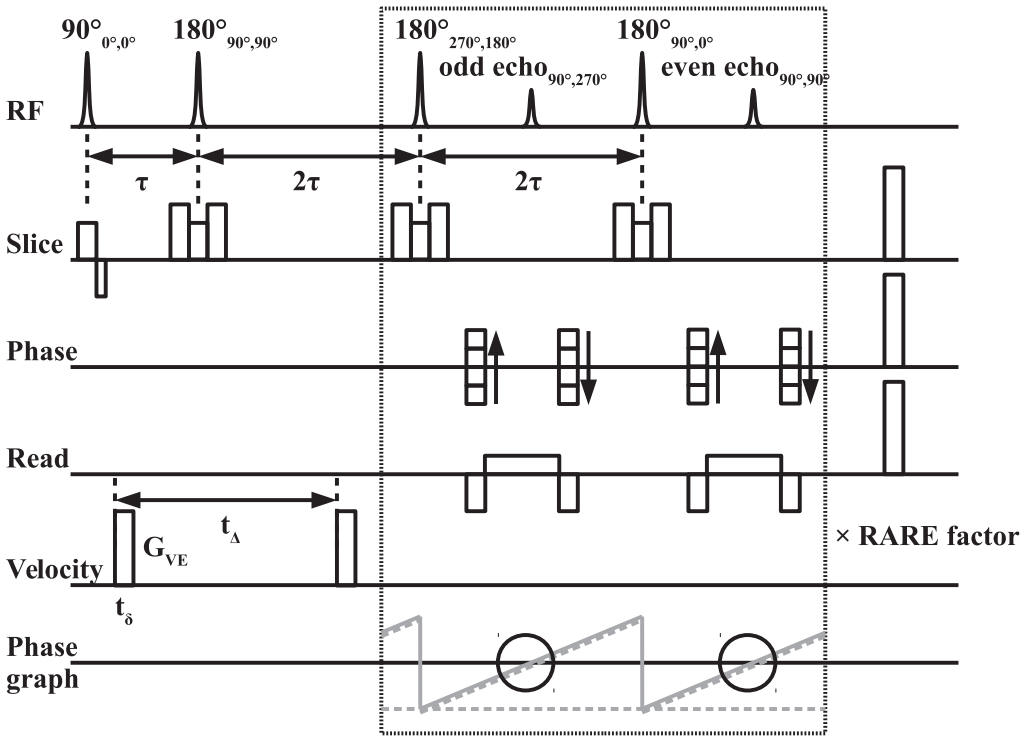

Figure 3.9: The RARE PC-MRI pulse sequence for 2D imaging with 1D velocimetry, applied with centric phase encoding. A pair of an odd echo and the subsequent even echo experiences identical spatial encoding gradients, *i.e.* phase encoding gradients are incremented after every pair of odd and even echoes. For non-slice-selective 3D imaging, soft RF pulses with slice-selection and slice-rephasing gradients are replaced by hard RF pulses, and phase encoding is also performed in the slice direction. The phase graph shows that an echo in the echo train (black solid circles) is a mixture of SE based coherence pathways (gray solid lines, only lowest order coherence pathways are shown) and STE based coherence pathways (gray dashed lines, only lowest order coherence pathways are shown).

Table 3.1: The Hadamard scheme defining the polarities of velocity ecoding gradients in 3D velocimetry.

scan number	G_x	G_y	G_z
1	$-$	$-$	$-$
2	$+$	$+$	$-$
3	$+$	$-$	$+$
4	$-$	$+$	$+$

encoding. Identical phase encoding gradients are applied within the inter-refocusing interval of an odd echo and the subsequent even echo, *i.e.* phase encoding gradients are incremented after every pair of odd and even echoes, in order to further compensate phase errors originating from the non-zero first-order gradient moments within each inter-refocusing interval. Detailed discussion about odd and even echoes will be given later. The effective TE for the NMR images of the odd and even echoes are 4τ and 6τ, respectively. The *echo train length* is defined in this subproject as the delay between the excitation pulse and the last echo, *i.e.* a product of number of echoes and the inter-echo delay 2τ. According to the pulse sequence (*cf.* Figure 3.9), it can be given by $(2 \cdot N_{RARE} + 1) \cdot 2\tau$.

The odd and the even part of the real-valued propagator $P(\Delta\boldsymbol{r}, t_\Delta)$ are the Fourier transform of the real part ($Re\{S(\boldsymbol{q})\}$) and imaginary part ($Im\{S(\boldsymbol{q})\}$) of the displacement-encoded complex-valued NMR signals in the q-space, respectively [81]. Therefore, in both q-space MRI and PC-MRI, both $Re\{S(\boldsymbol{q})\}$ and $Im\{S(\boldsymbol{q})\}$ have to be preserved and acquired correctly for velocimetry accuracy. However, $S(\boldsymbol{q})$ will be distorted due to B_1 inhomogeneity, particularly in the RARE echo train. Either $Re\{S(\boldsymbol{q})\}$ or $Im\{S(\boldsymbol{q})\}$ can be preserved by a pair of $90\,^\circ$ pulses with the corresponding phase, and the other part ($Im\{S(\boldsymbol{q})\}$ or $Re\{S(\boldsymbol{q})\}$ corresponding to the preserved $Re\{S(\boldsymbol{q})\}$ or $Im\{S(\boldsymbol{q})\}$, respectively) can be filtered by spoiler gradients between the pair of $90\,^\circ$ pulses [81]. With a two-step phase cycle [81], both $Re\{S(\boldsymbol{q})\}$ and $Im\{S(\boldsymbol{q})\}$ can be separately measured, respectively, and thus $S(\boldsymbol{q})$ can be correctly recovered. However, such STE based filtering will lead to a $50\,\%$ signal loss.

Another strategy is to apply a two-step phase cycling, where CPMG and CP RF pulse trains are used within the first and second phase cycling steps, respectively [80, 83]. In the first phase cycling step, $Re\{S(\boldsymbol{q})\}$ is preserved and $Im\{S(\boldsymbol{q})\}$ is distorted in the CPMG pulse trains. On the contrary, in the second phase cycling step, $Im\{S(\boldsymbol{q})\}$ is preserved and $Re\{S(\boldsymbol{q})\}$ is distorted in the CP pulse trains. Since $Im\{S(\boldsymbol{q})\}$ in the CPMG pulse trains is distorted with the same factor as $Re\{S(\boldsymbol{q})\}$ in the CP pulse trains, the correct phase of $S(\boldsymbol{q})$ can be recovered from the averaged signals of the two phase cycling steps.

One can also apply an imbalance in the read-dephasing gradient to separate SE based and STE based echoes in each inter-refocusing interval [97]. The mixing of SE and STE based echoes originates from B_1 inhomogeneity and results in a distortion of $S(\boldsymbol{q})$. With a balanced read-dephasing gradient, SE and STE based echoes coincide. With an unbalanced read-dephasing gradient (typically one half of the balanced one), both parity echoes can be separated in the time domain. The combination of them can recover the

information loss of the encoded displacements. This strategy does not need phase cycling and is thus at least twice as fast as the other two strategies mentioned above, though with the drawbacks of prolonged minimum TE, additional T_2^* contrast, and reduced SNR.

In this subproject, the two-step CPMG-CP phase cycling scheme [80, 83] was used to achieve high SNR and reduced T_2^* contrast, which is essential for PC-MRI in porous systems (*cf.* Figure 3.9). To compensate for B_1 inhomogeneity, an additional phase shift of π is applied to the refocusing pulses for the odd echoes. Unlike in earlier publications [80, 83], both odd and even echoes are acquired and combined to improve the SNR and velocimetry accuracy. A detailed discussion about the echo combination will be given later.

Gradient imperfections, such as eddy currents [86, 87] and concomitant magnetic fields [88], can generate additional phase errors, leading to non-zero phase contrast for static spins as offsets. The velocity offset maps can be measured with zero flow (*i.e* with the pump switched off) for correction of velocity maps.

Thus, the total measurement time t_{total} is given by

$$t_{total} = TR \cdot \frac{N_{PE}}{N_{RARE}} \cdot N_{slice} \cdot NA \cdot N_{VE} \cdot 2, \tag{3.2}$$

where N_{PE} is the number of primary phase encoding steps, N_{RARE} is the RARE factor, N_{slice} is the number of slices for 2D imaging (1 for multi-slice scheme) or the number of secondary phase encoding steps for 3D imaging, NA is at least 2 for phase cycling, and the factor of 2 refers to the measurements performed with the pump switched on and off. The effective acceleration factor of the pulse sequence is one half of N_{RARE}, which is due to the used two-step phase cycling. Thus, with an $N_{RARE} > 2$, the pulse sequence reduces the minimum t_{total} as compared to a single SE pulse sequence.

Data post-processing containing offline image reconstruction and velocity mapping was performed by home-made programs written in Matlab R2014a:

1. Individual NMR raw datasets of odd and even echoes measured with the pump switched on and off in different velocity encoding steps were separately Fourier transformed, yielding complex-valued NMR images.

2. Magnitude maps of the complex-valued NMR images were averaged to generate the structural images.

3. Gained by performing Otsu's thresholding algorithm [43] on the NMR images obtained in step 2, a binary mask was used in step 6 for nulling velocities in water-free voxels.

4. Phase contrast maps between the complex-valued NMR images in different velocity encoding steps were calculated by complex conjugation instead of direct phase difference, avoiding additional phase wrapping.

5. Phase unwrapping was performed by calling the external function PRELUDE [91] in the FSL 5.0 toolbox for individual phase contrast maps of odd and even echoes measured with the pump switched on and off.

6. Phase contrast maps were converted to velocity maps by multiplying the factor of $VENC/\pi$ and the binary mask generated in step 3.

7. Echo combined velocity maps were computed by voxel-wise averaging of velocity maps of odd and even echoes. Offset corrected velocity maps were computed by voxel-wise subtraction of velocity maps measured with the pump switched off from velocity maps measured with the pump switched on.

8. Slice-wise VFR along a given direction was computed by integrating the corresponding velocity components in the direction and then multiplying by the cross-sectional area of a single voxel. For instance, slice-wise VFR along the z-axis ($VFR_z(z)$) is given by

$$VFR_z(z) = (\delta x \cdot \delta y) \cdot \sum_{x,y} v_z(x, y, z), \tag{3.3}$$

   where δx and δy are the voxel sizes in the x- and y-directions, respectively, and v_z is the z-component of the velocity.

9. Quantitative assessment of the proposed method, particularly the performance of echo combination and offset correction, was based on statistics of slice-wise VFR. On the one hand, an averaged VFR over slices closest to the expected value of the pumping rate indicates the most accurate velocimetry. On the other hand, a least STD between VFR over slices implies the flow continuity.

3.3.2 Validation on Laminar Tube Flow using the Bruker Coil

The proposed RARE PC-MRI method, particularly the echo combination strategy which is different from existing literatures (*e.g.* [81]), was validated by measurements of a simple sample containing a tube with laminar flow of distilled water and two neighboring bottles with static distilled water. The pumping rate was set to $63.0\,mm^3/s$ according to the linear dependency

of formerly measured VFR, yielding laminar flow with velocities of up to approximately $5\,mm/s$ through the tube with a diameter of about $6\,mm$. However, this time the VFR, which was measured by monitoring the outflowing water again, was slightly lower ($60.7\,mm^3/s$) than expected. The Bruker RF coil with high B_1 homogeneity was used for these measurements.

Multi-slice 2D imaging with 1D velocimetry by the proposed RARE PC-MRI method was performed with the following protocol: hermite RF pulses, τ $5.0\,ms$, effective TE $20.0\,ms$ / $30.0\,ms$ (odd / even echo), FOV $20 \times 20\,mm^2$, matrix size 160×160, read direction x, N_{RARE} 16, echo train length $330.0\,ms$, d_{SS} $0.5\,mm$, N_{slice} 5, inter-slice distance $6.0\,mm$, slice direction z, voxel size $125 \times 125 \times 500\,\mu m^3$, t_Δ $10.0\,ms$, $VENC$ $7.5\,mm/s$, 1D velocity encoding in the z-direction, N_{VE} 2, TR $5.0\,s$, NA 2, t_{total} $6.67\,min$.

For comparison, 2D imaging with 1D velocimetry by a single SE PC-MRI pulse sequence was performed using a mostly identical protocol to the one described above: hermite RF pulses, TE $10.0\,ms$, FOV $20 \times 20\,mm^2$, matrix size 160×160, read direction x, d_{SS} $0.5\,mm$, N_{slice} 5, inter-slice distance $6.0\,mm$, slice direction z, voxel size $125 \times 125 \times 500\,\mu m^3$, t_Δ $10.0\,ms$, $VENC$ $7.5\,mm/s$, 1D velocity encoding in the z-direction, N_{VE} 2, TR $5.0\,s$, NA 2, t_{total} $1.78\,h$.

Additionally, 3D imaging with 1D velocimetry was performed by the proposed RARE PC-MRI method with the following protocol: rectangular RF pulses, τ $4.0\,ms$, effective TE $16.0\,ms$ / $24.0\,ms$ (odd / even echo), FOV $32 \times 16 \times 16\,mm^3$, matrix size $200 \times 100 \times 100$, voxel size $160 \times 160 \times 160\,\mu m^3$, read direction z, RARE phase encoding in the y-direction, N_{RARE} 10, echo train length $168.0\,ms$, t_Δ $4.0\,ms$, $VENC$ $15.0\,mm/s$, 1D velocity encoding in the z-direction, N_{VE} 2, TR $1.0\,s$, NA 2, t_{total} $2.22\,h$.

Figure 3.10 shows the NMR image of a representative slice in the sample, which was measured by the proposed RARE PC-MRI method as 2D imaging with 1D velocimetry. Nine velocity maps of the corresponding slice are shown in Figure 3.11, representing intermediate post-processing results with echo combination and/or offset correction (*cf.* step 7 in the post-processing procedures). Non-negligible velocity offsets of static water were observed in the bottles (bottom) and also in the tube (top) with the pump switched off, indicating the necessity of offset correction. Such offset correction by differencing velocity maps with the pump switched on and off was also applied in the single SE PC-MRI method, as shown in Figure 3.12a, 3.12b, and 3.12c. An extra offset as a base value remaining in the resulting velocity maps (Figure 3.12c) was then estimated by averaging velocities of static water, and was subsequently corrected. The final velocity maps without substantial velocity offsets are displayed in Figure 3.12d. Due to the necessity of offset correction, results in the rest of this subsection focus on the echo combination strategy.

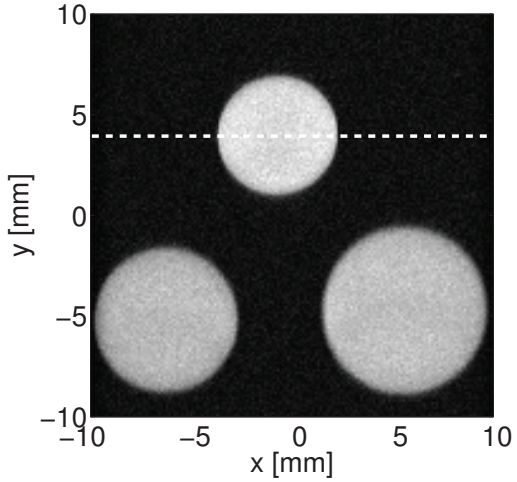

Figure 3.10: NMR image of a representative slice in the sample with laminar flow of water in a tube (top) and static water in bottles (bottom). The white dashed line represents the horizontal line crossing the tube center and was selected for subsequent comparison between velocity profiles.

According to the Hagen-Poisueille flow, parabolic fitting was performed on the offset corrected velocity maps (*cf.* Figure 3.11c, 3.11f, and 3.11i, and 3.12d). The corresponding longitudinal velocity (v_z) values of the selected line (*cf.* Figure 3.10, white dashed line) were then compared, as shown in Figure 3.13. Good agreement between the flow patterns obtained in both PC-MRI methods was found only if echo combination in the proposed RARE PC-MRI method was used (*cf.* Figure 3.13, solid green and black lines).

Further quantitative analysis using different VFR computation ways supported this finding. In Figure 3.14 slice-wise longitudinal VFR (VFR_z) values in 2D imaging with 1D velocimetry measured by both PC-MRI methods are compared. Figure 3.15 shows a comparison between slice-wise longitudinal VFR (VFR_z) values from intermediate post-processing results in 3D imaging with 1D velocimetry by the proposed RARE PC-MRI method. The statistics of longitudinal VFR (VFR_z) values over xy-slices corresponding to Figure 3.14 and 3.15 is summarized in Table 3.2. In 2D imaging with 1D velocimetry, the VFR values measured by both PC-MRI methods and computed by parabolic fitting, as well as the expected VFR value of $63.0\,mm^3/s$, agree with each other only if echo combination in the proposed RARE PC-MRI method was used. In 3D imaging with 1D velocimetry, the coincidence between the expected VFR value of $63.0\,mm^3/s$ and the VFR values measured by the proposed RARE PC-MRI method and computed by parabolic fitting was again found only when both odd and even echoes were combined.

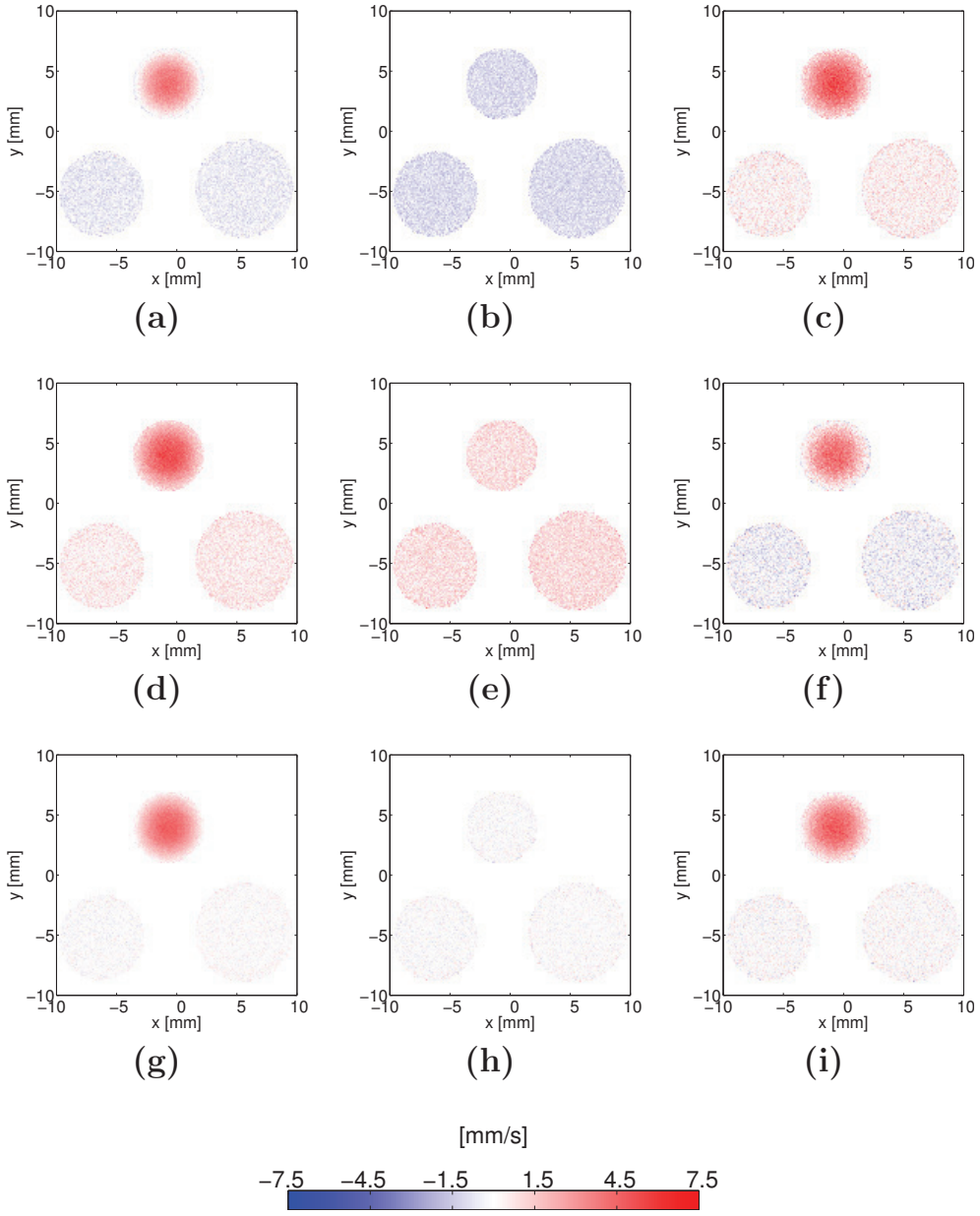

Figure 3.11: Velocity maps of the corresponding slice in Figure 3.10 measured by the proposed RARE PC-MRI method as 2D imaging with 1D velocimetry, representing intermediate post-processing results (*cf.* step 7 in the post-processing procedures) with: (a) odd echo alone, pump on; (b) odd echo alone, pump off; (c) odd echo alone, offset corrected; (d) even echo alone, pump on; (e) even echo alone, pump off; (f) even echo alone, offset corrected; (g) echo combined, pump on; (h) echo combined, pump off; (i) echo combined, offset corrected.

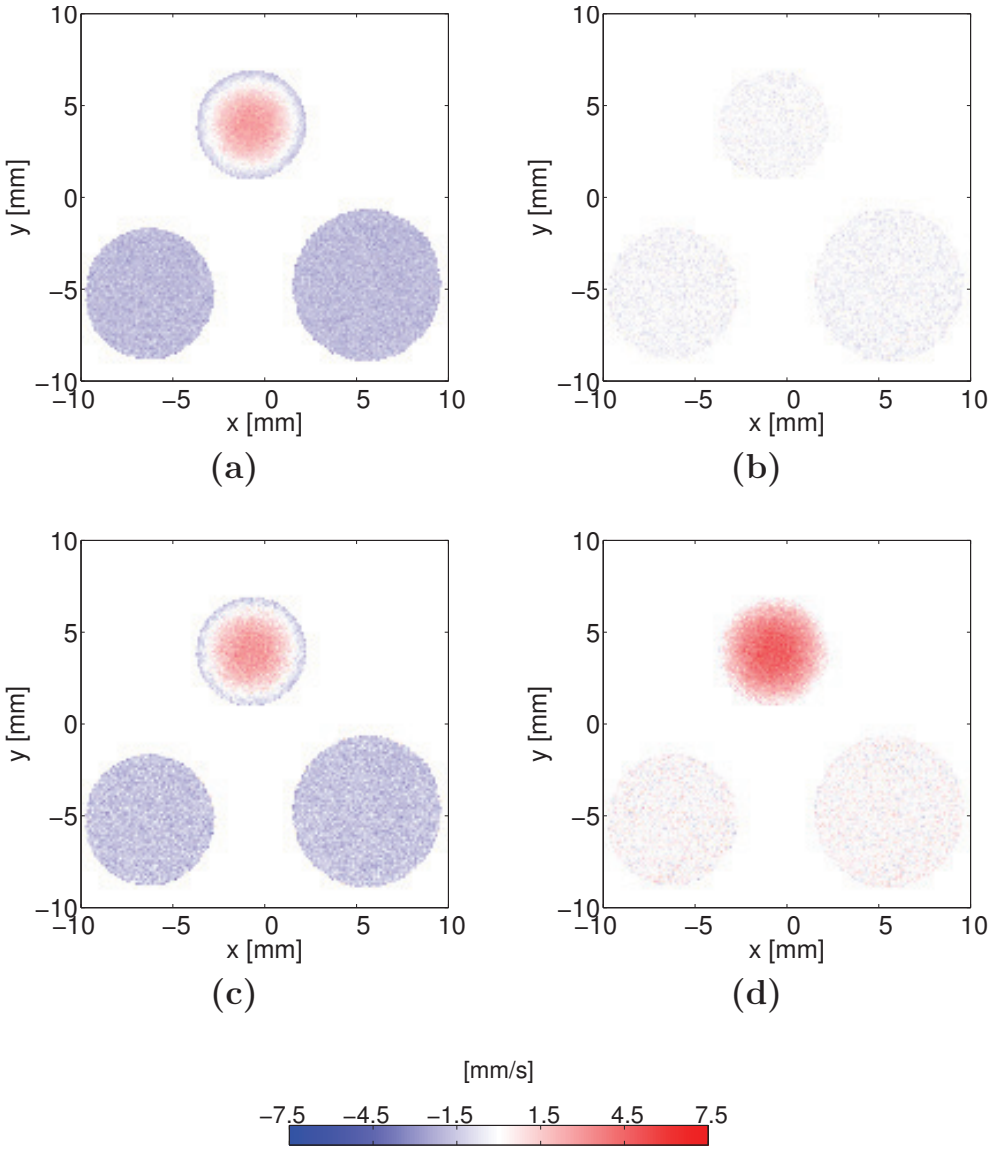

Figure 3.12: Velocity maps of the corresponding slice in Figure 3.10 measured by the single SE PC-MRI method as 2D imaging with 1D velocimetry, representing intermediate post-processing results with: (a) pump on; (b) pump off; (c) offset preliminarily corrected by differencing (a) and (b); (d) offset corrected.

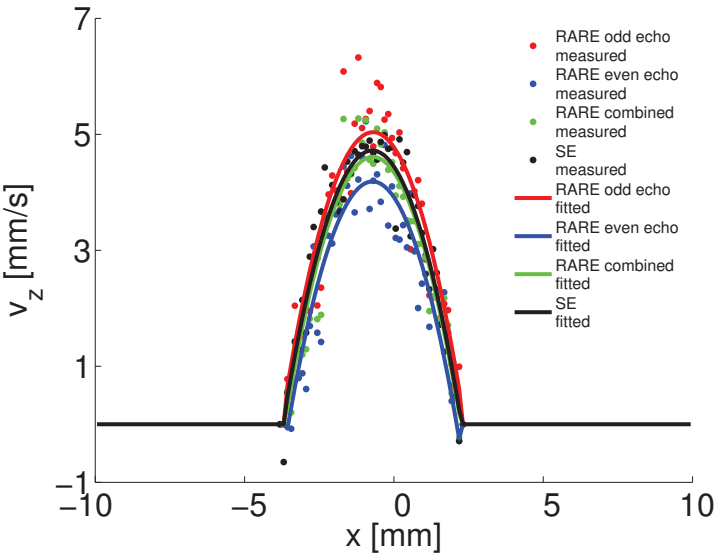

Figure 3.13: Comparison between longitudinal velocity (v_z) values of the selected line (*cf.* Figure 3.10, white dashed line) in offset corrected velocity maps measured and regressed by parabolic fitting in both PC-MRI methods as 2D imaging with 1D velocimetry.

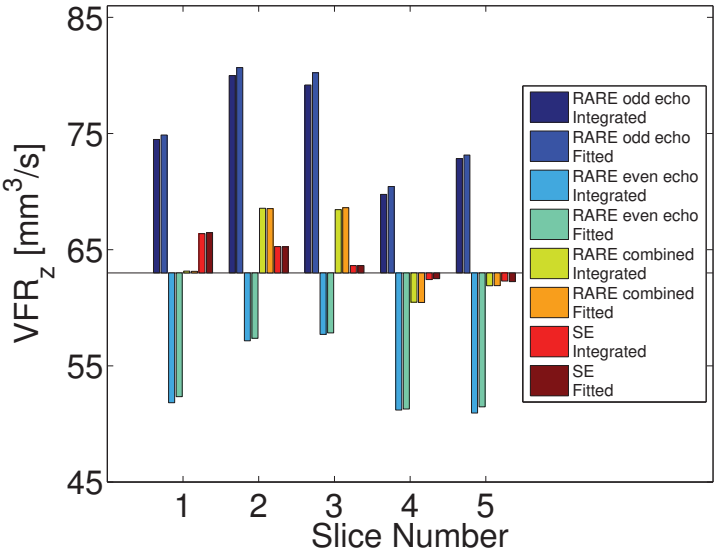

Figure 3.14: Bar graph of slice-wise longitudinal VFR (VFR_z) values obtained by both PC-MRI methods as 2D imaging with 1D velocimetry and different computation ways: integration (*cf.* step 8 in the post-processing procedures) and parabolic fitting. The baseline of the bar graph is the expected pumping rate $63.0\,mm^3/s$.

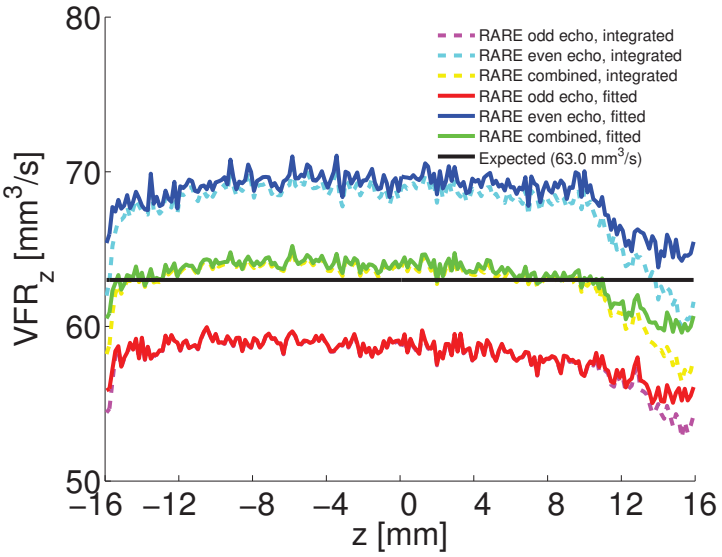

Figure 3.15: Plots of slice-wise longitudinal VFR (VFR_z) values obtained by the proposed RARE PC-MRI method as 3D imaging with 1D velocimetry and different computation ways: integration (*cf.* step 8 in the post-processing procedures) and parabolic fitting.

Both the datasets of the odd echo alone and the echo combined have slice-wise VFR values comparably close to another expected VFR of $60.7\,mm^3/s$ (measured by monitoring outgoing water) in 3D imaging with 1D velocimetry by the proposed RARE PC-MRI method (*cf.* Table 3.2a). However, still only the echo combination yielded the VFR closest to this expected VFR of $60.7\,mm^3/s$ in 2D imaging with 1D velocimetry (*cf.* Table 3.2b). The echo combination strategy proved to improve the velocimetry accuracy.

Note that a greater improvement on velocimetry accuracy was found in 2D imaging with 1D velocimetry than in 3D imaging with 1D velocimetry. Odd or even echo alone generated incorrect VFR in the former experiment (*cf.* Figure 3.14 and Table 3.2a), and yielded approximately correct VFR in the latter experiment (*cf.* Figure 3.15 and Table 3.2b). The same finding was observed in succeeding experiments on the filtration cell and will be discussed later.

In this subproject, the quantitative analysis of flow was based on slice-wise VFR values, which were obtained by integrating velocities within voxels in the same slices (*cf.* step 8 in the proposed data post-processing procedures). The consistency between results from the integration and parabolic fitting methods (*cf.* Figure 3.14 and 3.15, as well as Table 3.2) indicated the feasibility of the integration method.

Table 3.2: Statistics (average ± STD, *cf.* step 9 in the post-processing procedures) of VFR_z over xy-slices in the laminar tube flow sample.

$VFR_z\,[mm^3/s]$	RARE odd echo	RARE even echo	RARE combined	SE
integration	75.2 ± 4.31	53.8 ± 3.37	64.5 ± 3.77	64.0 ± 1.79
parabolic fitting	75.9 ± 4.47	54.1 ± 3.26	64.5 ± 3.81	64.0 ± 1.81

(a) 2D imaging with 1D velocimetry.

$VFR_z\,[mm^3/s]$	RARE odd echo	RARE even echo	RARE combined
integration	58.0 ± 1.47	67.6 ± 2.23	62.8 ± 1.81
parabolic fitting	58.2 ± 1.12	68.6 ± 1.55	63.2 ± 1.27

(b) 3D imaging with 1D velocimetry.

It is also noteworthy that the additional velocity offsets in the single SE PC-MRI method may be interpreted as propagator distortion in the implemented single SE PC-MRI method. In the future, an improved scheme of phase cycling may compensate this propagator distortion.

3.3.3 Results on Porous Filter using the Bruker Coil

The proposed RARE PC-MRI method was subsequently examined on the filtration cell using the Bruker coil. The mounted porous filter was a templated foam derived from polysiloxane and produced as a cylindrical filter sample (diameter $9\,mm$, height $18\,mm$) with spherical pores with a mean diameter of about $2\,mm$ by the collaborator (Michaela Wilhelm) according to [98]. Due to limited vertical space available in the scanner bore, the filtration cell was placed horizontally at the coil center. The pumping rate was $12.6\,mm^3/s$, yielding a longitudinal flow through the filtration cell with velocities of up to $5\,mm/s$. Multi-slice 2D imaging with 1D velocimetry was performed. The measurement protocol was as follows: hermite RF pulses, τ $5.0\,ms$, effective TE $20.0\,ms$ / $30.0\,ms$ (odd / even echo), FOV $20\times20\,mm^2$, matrix size 160×160, read direction x, N_{RARE} 16, echo train length $330.0\,ms$, d_{SS} $0.5\,mm$, N_{slice} 5, inter-slice distance $6.0\,mm$, slice direction z, voxel size $125\times125\times500\,\mu m^3$, t_Δ $10.0\,ms$, $VENC$ $7.5\,mm/s$, 1D velocity encoding in the z-direction, N_{VE} 2, TR $5.0\,s$, NA 2, t_{total} $6.7\,min$.

NMR images of distilled water in the sample (slice 2 to 4) and also in the outlet (slice 1) and inlet (slice 5) are shown in Figure 3.16. The half ring structure outside the outlet in slice 1 is due to static water within the

sealing of the filtration cell. The static water settled accidentally during the installation of the sample into the filtration cell or during pore saturation. Since the sealing has no connection to the internal part of the filtration cell, the static water was considered to have no influences on the velocimetry results.

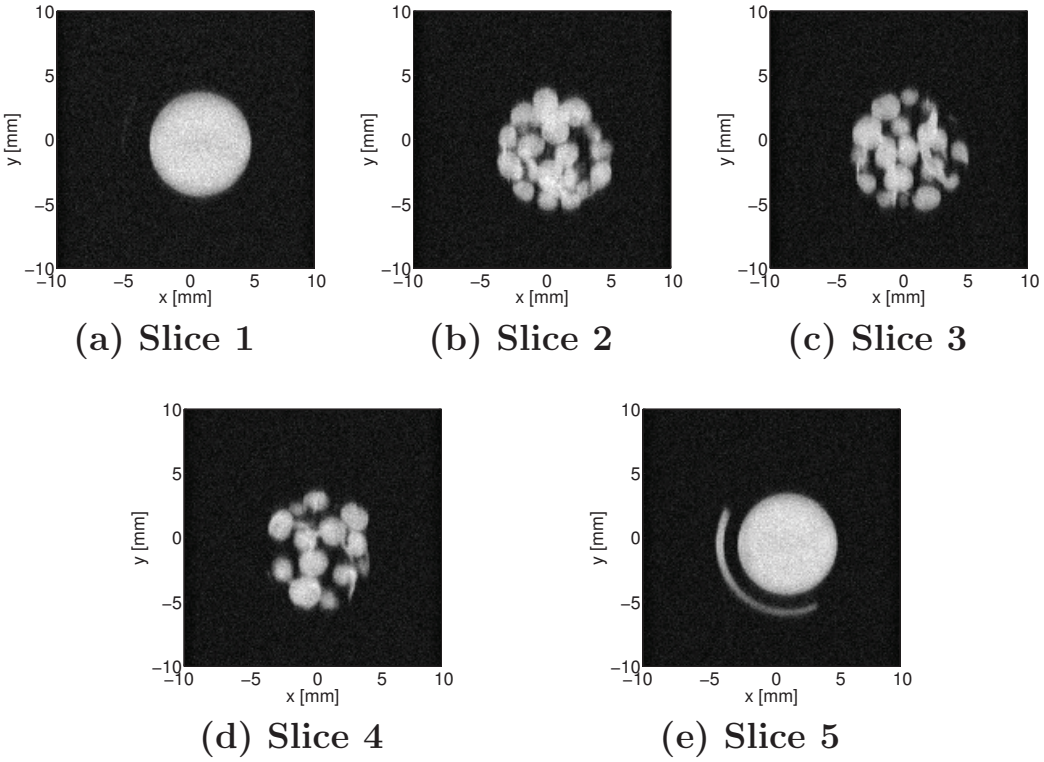

(a) Slice 1 **(b) Slice 2** **(c) Slice 3**

(d) Slice 4 **(e) Slice 5**

Figure 3.16: NMR images of 5 slices from the 2D imaging with 1D velocimetry measurement. Slice 1 is in the outlet, slice 2 to 4 in the sample, and slice 5 in the inlet.

Nine velocity maps of the central slice (slice 3 in Figure 3.16) are shown in Figure 3.17, representing intermediate post-processing results with echo combination and/or offset correction (*cf.* step 7 in the post-processing procedures). In the middle column (*cf.* Figure 3.17b, 3.17e, and 3.17h), non-zero velocity maps of odd and even echoes alone and echo combination measured with the pump switched off can be observed, again demonstrating the necessity for offset correction.

These nine velocity maps (*cf.* Figure 3.17) were compared by investigating the slice-wise longitudinal VFR (VFR_z) (*cf.* step 8 in the post-processing procedures). The best agreement with the expected VFR_z (the pumping rate as the baseline in Figure 3.18) was found if both echo combination and

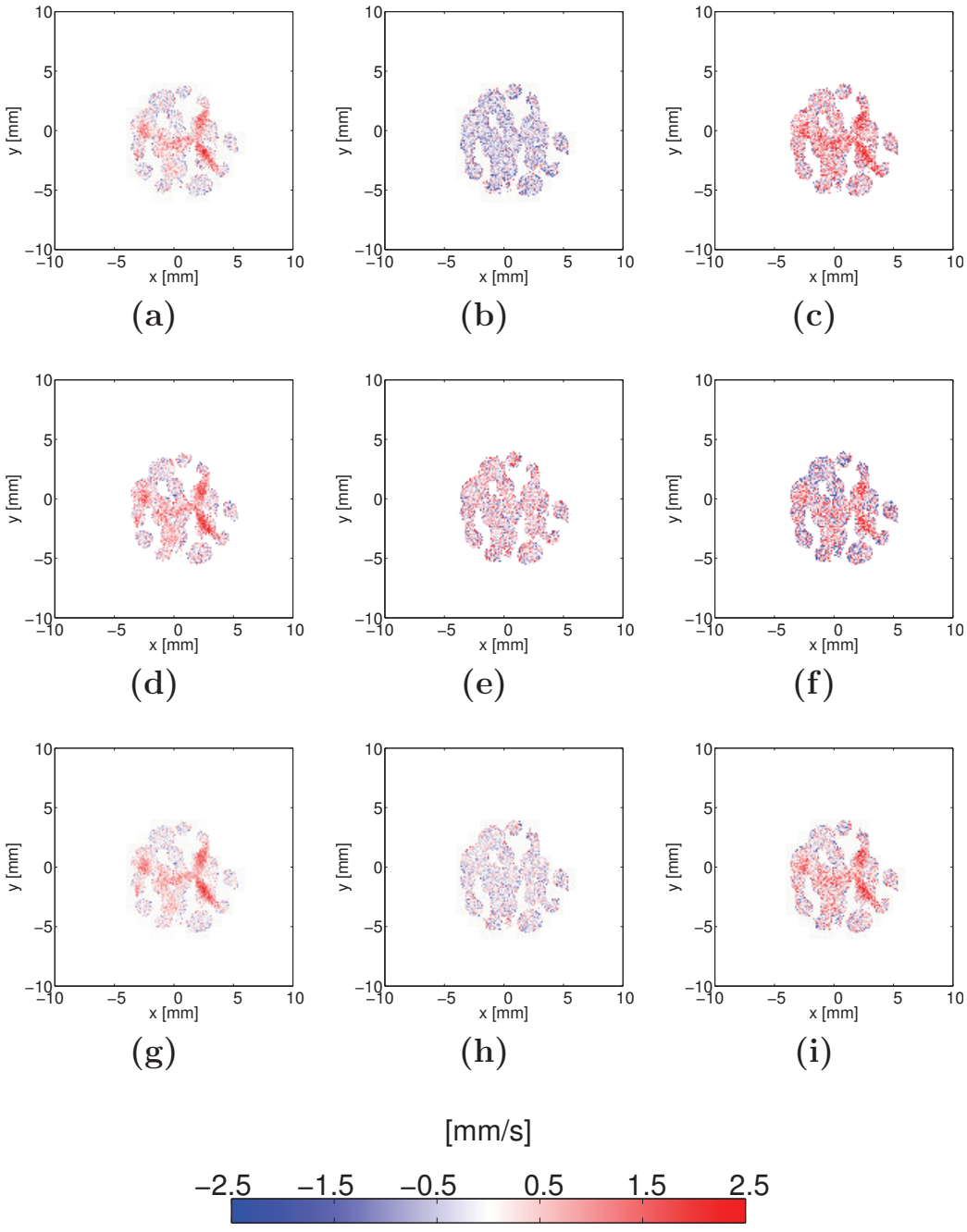

Figure 3.17: Velocity maps of the central slice (slice 3 in Figure 3.16) in the 2D imaging with 1D velocimetry measurement as intermediate post-processing results (*cf.* step 7 in the post-processing procedures) with: (a) odd echo alone, pump on; (b) odd echo alone, pump off; (c) odd echo alone, offset corrected; (d) even echo alone, pump on; (e) even echo alone, pump off; (f) even echo alone, offset corrected; (g) echo combined, pump on; (h) echo combined, pump off; (i) echo combined, offset corrected.

offset correction (dark red bars as the smallest ones in Figure 3.18) were applied. Statistics of VFR_z over xy-slices (*cf.* step 9 in the post-processing procedures), as shown in Table 3.3, also support this finding: with both echo combination and offset correction, the averaged VFR_z over xy-slices has the most accurate value ($13.1\,mm^3/s$ compared to $12.6\,mm^3/s$ corresponding to the pumping rate, relative error about $4\,\%$) and the STD between VFR_z over xy-slices has the least value ($1.00\,mm^3/s$).

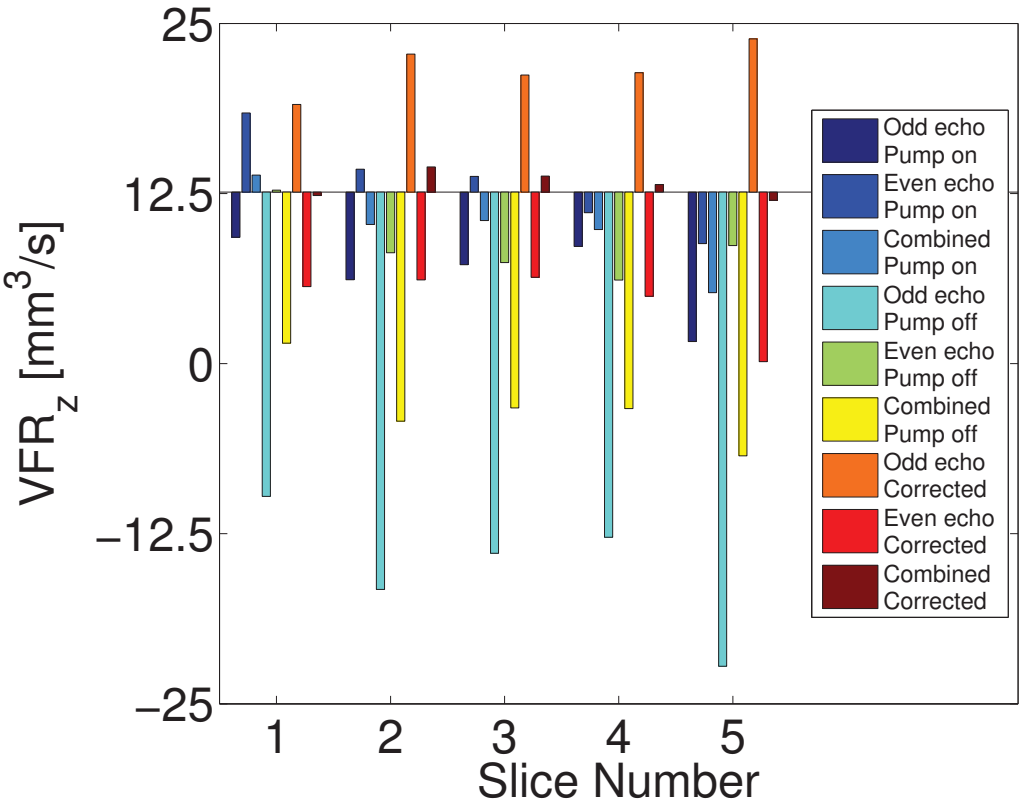

Figure 3.18: Bar graph of slice-wise longitudinal VFR (VFR_z) values obtained by the proposed RARE PC-MRI method, representing intermediate post-processing results with echo combination and/or offset correction (*cf.* step 7 in the post-processing procedures). The baseline of the bar graph is the expected pumping rate $12.6\,mm^3/s$.

Table 3.3: Statistics (average ± STD, *cf.* step 9 in the post-processing procedures) of VFR_z over xy-slices in the filtration cell using the Bruker coil.

$VFR_z\,[mm^3/s]$	pump on	pump off	corrected
odd echo	6.59 ± 3.03	-15.1 ± 4.71	21.7 ± 1.81
even echo	13.3 ± 3.62	8.63 ± 2.49	4.65 ± 2.57
combined	9.93 ± 3.08	-3.22 ± 3.00	13.1 ± 1.00

3.3.4 Results on Porous Filter using the Home-made RF Coil

After the above examination, the proposed RARE pulse sequence was used in combination with the home-made RF coil. The filtration cell with the same porous filter mounted was placed vertically, with the sample at the coil center. The pumping rate was set to $37.8\,mm^3/s$, providing a vertical flow through the filtration cell with velocities of up to $15\,mm/s$. 3D imaging with 1D velocimetry was performed. The measurement protocol was as follows: rectangular RF pulses, τ $4.0\,ms$, effective TE $16.0\,ms$ / $24.0\,ms$ (odd / even echo), FOV $32 \times 16 \times 16\,mm^3$, matrix size $200 \times 100 \times 100$, voxel size $160 \times 160 \times 160\,\mu m^3$, read direction y, RARE phase encoding in the z-direction, N_{RARE} 10, echo train length $168.0\,ms$, t_Δ $4.0\,ms$, $VENC$ $15.0\,mm/s$, 1D velocity encoding in the y-direction, N_{VE} 2, TR $1.0\,s$, NA 2, t_{total} $2.2\,h$.

An NMR image of distilled water in the filtration cell is shown in Figure 3.19a. Reduced image intensities were observed in the inlet (top region) and outlet (bottom region), resulting from the B_1 inhomogeneity of the home-made RF coil (*cf.* Figure 3.6). In the bottom right region in Figure 3.19a, again some static water within the sealing of the filtration cell is visible again.

The map of vertical velocity (v_y) after echo combination and offset correction (*cf.* Figure 3.19b) shows several main streaming paths of the distilled water through the sample. The negative values stand for velocities in the $-y$ direction, *i.e.* vertically downwards.

Vertical VFR (VFR_y) values *versus* xz-slice position are plotted in Figure 3.19c. Large linear ramps of VFR and thus velocities are found in the datasets measured with the pump switched on (magenta, cyan, and yellow solid lines in Figure 3.19c) and off (magenta, cyan, and yellow dashed lines in Figure 3.19c), respectively. With offset correction, these ramps are substantially compensated (red, and blue solid lines in Figure 3.19c). The later applied echo combination (green solid line in Figure 3.19c) yields a VFR_y which is in better agreement with the pumping rate (black solid line in Figure 3.19c) than those obtained from odd (red solid line in Figure 3.19c) or even

(blue solid line in Figure 3.19c) echo analyzed individually.

Statistics of VFR_y over xz-slices (*cf.* step 9 in the post-processing procedures) are shown in Table 3.4. Fluctuations of velocities can be strongly reduced by offset correction. Additionally, systematic errors are substantially reduced by echo combination, yielding an accurate averaged VFR_y of $-36.6\,mm^3/s$ compared to $-37.8\,mm^3/s$ (relative error about 3 %) corresponding to the pumping rate, although with slightly higher STD of $1.62\,mm^3/s$ than for the dataset of the odd echo alone of $1.02\,mm^3/s$ (*cf.* fourth column in Table 3.4).

Table 3.4: Statistics (average ± STD, *cf.* step 9 in the proposed data post-processing procedures) of vertical VFR (VFR_y) over xz-slices in the 3D imaging with 1D velocimetry measurement.

$VFR_z\,[mm^3/s]$	pump on	pump off	corrected
odd echo	-42.9 ± 33.5	-9.36 ± 32.9	-33.6 ± 1.02
even echo	-51.3 ± 33.7	-11.6 ± 31.7	-40.0 ± 2.39
combined	-47.1 ± 33.6	-10.5 ± 32.3	-36.6 ± 1.62

3.3.5 Towards Applications: 3D Imaging with 3D Velocimetry on Porous Filter using the Home-made RF Coil

3D velocity maps of slow water flow through the filtration cell with the same porous filter mounted were acquired by using the home-made RF coil, mimicking the desired PC-MRI application for deep bed filtration. The pumping rate was $12.6\,mm^3/s$, yielding a vertical flow through the filtration cell with velocities of up to $5\,mm/s$. The measurement protocol of the 3D imaging with 3D velocimetry was as follows: rectangular RF pulses, τ $4.0\,ms$, effective TE $16.0\,ms$ / $24.0\,ms$ (odd / even echo), FOV $32 \times 16 \times 16\,mm^3$, matrix size $200 \times 100 \times 100$, voxel size $160 \times 160 \times 160\,\mu m^3$, read direction y, RARE phase encoding in the z-direction, N_{RARE} 10, echo train length $168.0\,ms$, t_Δ $8.0\,ms$, $VENC$ $5.0\,mm/s$, 3D velocity encoding in the x-, y- and z-directions, N_{VE} 4, TR $1.0\,s$, NA 2, t_{total} $4.4\,h$.

An NMR image of the central xy-slice with overlaid velocity vector fields and enlarged view of an image section (blue rectangle) are shown in Figure 3.20a. The vertical VFR (VFR_y) values *versus* xz-slice position are plotted in Figure 3.20b, yielding consistent VFR_y (red solid line in Figure 3.20b) which is slightly lower than expected (blue dashed line in Figure 3.20b). Similarly, Figure 3.20c shows an NMR image of the central xz-slice with

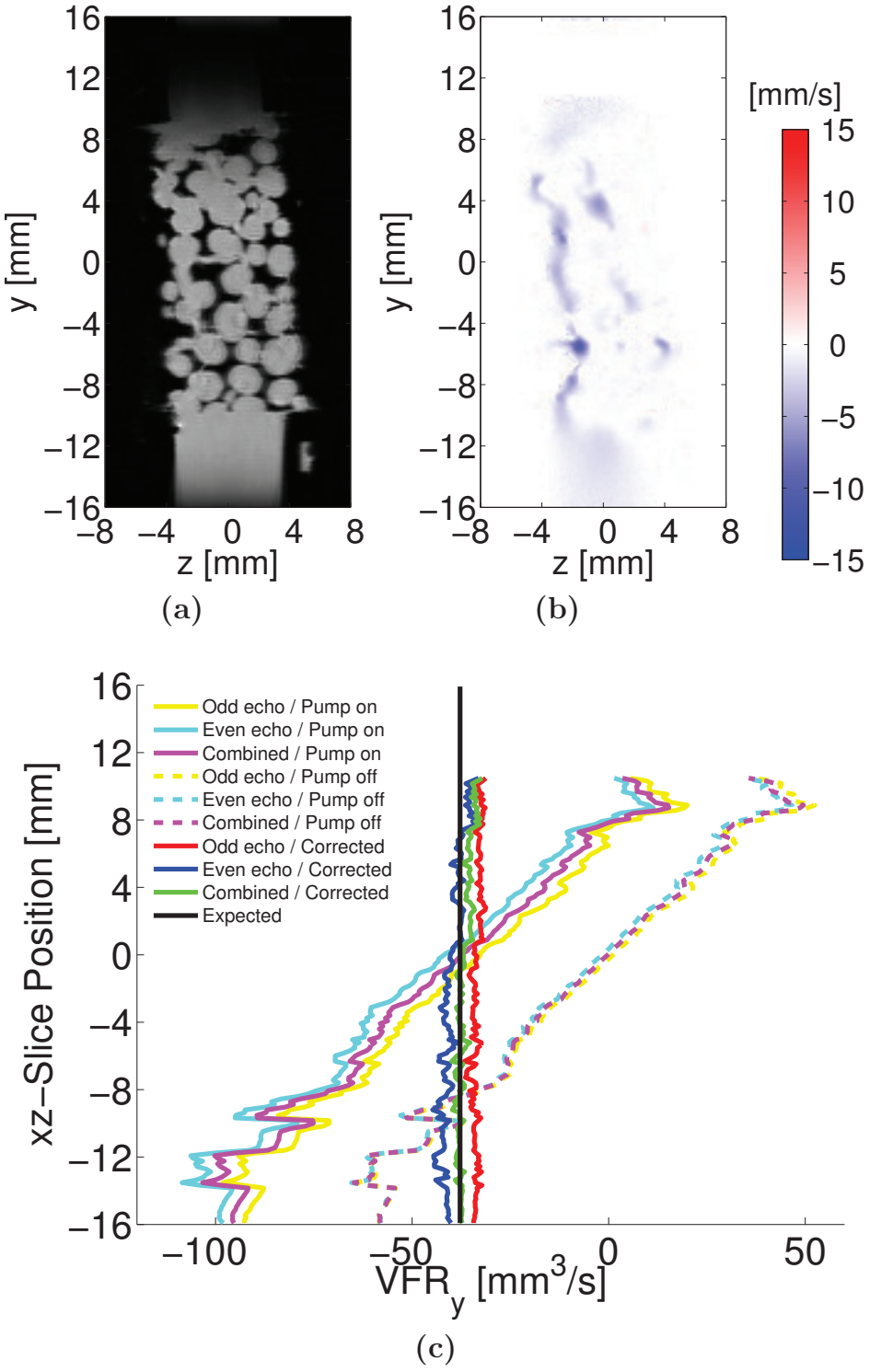

Figure 3.19: Results of 3D imaging with 1D velocimetry on the filtration cell using the home-made RF coil. (a) NMR image of the central yz-slice. (b) Map of vertical velocity (v_y) of the central yz-slice. (c) Plot of vertical VFR (VFR_y) values of different intermediate post-processing datasets *versus* xz-slice position.

overlaid velocity vector fields, and enlarged view of an image section (blue rectangle). As an example of the transversal VFR, the VFR along the x-axis (VFR_x) *versus* yz-slice position are plotted in Figure 3.20d. The fluctuations of the slice-wise VFR_x around zero (*cf.* Figure 3.20d) reflect that no net transversal flow or leakage was taking place during the measurement. The averaged VFR_y with STD over xz-slices is $-12.0 \pm 0.524\,mm^3/s$ compared to $-12.6\,mm^3/s$ (relative error about 5 %) the independently measured the pumping rate, while the averaged VFR_x with STD over yz-slices is $0.139 \pm 0.780\,mm^3/s$ comes very close to the expected zero value.

3.4 Discussion of the Proposed RARE PC-MRI Method

In this subproject, both the experimental setup and existing PC-MRI methods were optimized for velocimetry of slow liquid flow in porous materials. First, a dedicated RF coil was constructed and adjusted to the specific requirements of a filtration cell used to study deep bed filtration. Second, a RARE PC-MRI pulse sequence was modified for fast and accurate velocimetry in porous materials despite B_1 inhomogeneity, particularly by means of offset correction and echo combination. Third, a set of customized routines for data post-processing was used to quantify and verify velocity fields measured in a porous sample.

3.4.1 Pulse Sequence Acceleration

Acceleration of the pulse sequence is determined by the factor N_{RARE} that depends on the inter-echo delay and the maximum echo train length, which is in turn restricted by the T_2 signal decaying. The pulse sequence proved to be insensitive to phase errors introduced within the echo train by certain intra- and inter-pore displacements, resulting in accurate velocity maps and suppressed displacement related blurring and ghosting artifacts. This can be examined particularly in the experiment on the porous filter by performing 3D imaging with 1D velocimetry with a pumping rate of $37.8\,mm^3/s$, where the maximum velocity value (slightly smaller than $15\,mm/s$) was higher than in other experiments. The moving spins with the velocity range of $[-15, 15]\,mm/s$ had displacements of up to $2.52\,mm$ after the echo train, which are equivalent to up to $15.75\,voxels$ with the voxel size of $160\,\mu m$ and $1.26\,pores$ with the mean pore size of about $2\,mm$.

Under the assumption of negligible velocity changes of moving spins in the echo train, suppression of the displacement related phase errors is achieved

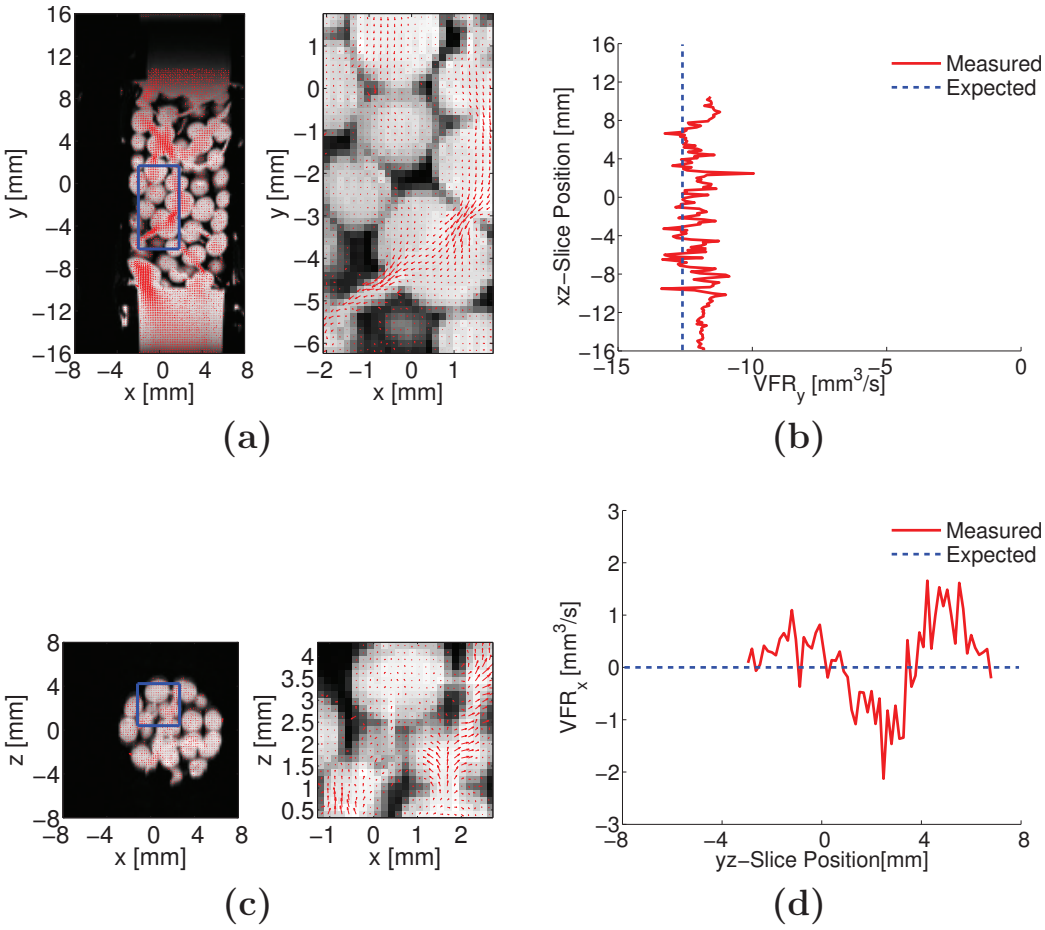

Figure 3.20: Results of 3D imaging with 3D velocimetry on the filtration cell using the home-made RF coil. (a) NMR image of the central xy-slice with overlaid velocity vector fields, and enlarged view of an image section (blue rectangle). (b) Plot of vertical VFR (VFR_y) *versus* xz-slice position. (d) NMR image of the central xz-slice with overlaid velocity vector fields , and enlarged view of an image section (blue rectangle). (d) Plot of transveral VFR in the x-direction (VFR_x) *versus* yz-slice position.

by four means: (i) read dephasing, acquisition and read rephasing within each inter-refocusing interval, suppressing phase errors in read direction; (ii) identical pairs of phase encoding winder and rewinder gradients for each pair of odd and even echoes, compensating phase errors in phase encoding direction after an even number of echoes; (iii) balanced crusher gradient pairs, canceling out phase errors introduced by displacements in slice direction after an even number of echoes; (iv) centric phase encoding, minimizing displacements during the delay between velocity encoding and the subsequent first pair of odd and even echoes, when the central k-space is acquired ($24\,ms$ and thus displacements of up to $0.18\,pores$ in the 3D imaging with 1D velocimetry experiment).

However, for very fast flow, even during the delay between velocity encoding and the subsequent acquisition of the central k-space, moving spins will have very large inter-pore displacements and altered velocities, thus preventing accurate velocimetry by this pulse sequence.

For systems with negligible changes in $\boldsymbol{B}_0$ fields during a series of *in situ* NMR measurements with a fixed protocol, each NMR measurement only takes $t_{total}/2$ as the real measurement time, since the velocity offset maps can be regarded as consistent and require only one additional *in situ* NMR measurement with the identical protocol.

3.4.2 Offset Correction

The necessity of the applied offset correction for accurate velocimetry was recognized when investigating the non-zero velocities measured with the pump switched off in all experiments. As shown in velocity maps (*cf.* Figure 3.11, 3.12, and 3.17) and quantitative analysis of VFR (*cf.* Figure 3.18 and 3.19, as well as Table 3.3 and 3.4), phase contrast was introduced for static spins by inverting the polarity of velocity encoding gradients. This additional phase contrast most likely originates from gradient imperfections, such as eddy currents [86, 87] and concomitant fields [88]. Therefore, for fixed $\boldsymbol{B}_0$ fields and a given measurement protocol, it will remain unchanged when performing measurements with the pump switched either on or off, thus enabling precise velocity maps by offset correction.

3.4.3 Echo Combination

The velocimetry results using odd or even echoes alone, and echo combination were compared for the assessment of echo combination strategy. First, the comparison was applied in the NMR experiment on laminar tube flow of

distilled water using the Bruker coil with high B_1 homogeneity. The measured flow patterns, which were acquired by the proposed RARE PC-MRI method and a single SE PC-MRI method, show good agreement with each other and also coincide with the parabolic flow pattern expected for the given pumping rate, as illustrated in Figure 3.13. Moreover, slice-wise longitudinal VFR (VFR_z) and averaged VFR_z with STD over xy-slices have good agreement with the expected VFR, as shown in Figure 3.14 and 3.15 as well as Table 3.2. Second, such strategy assessment in the NMR experiments on the porous filter was performed by comparing slice-wise longitudinal VFR (VFR_z) and averaged VFR_z with STD over xy-slices in the 2D imaging with 1D velocimetry experiment (*cf.* Figure 3.18 and Table 3.3), and also slice-wise vertical VFR (VFR_y) and averaged VFR_y with STD over xz-slices in the 3D imaging with 1D velocimetry experiment (*cf.* Figure 3.19c and Table 3.4). Echo combination was superior in velocimetry accuracy to using odd or even echo alone, giving best agreement with the expected VFR ($63.0\,mm^3/s$ in the experiment on laminar flow, $12.6\,mm^3/s$ in the experiment on the porous filter using the Bruker coil, and $37.8\,mm^3/s$ in the experiment on the porous filter using the home-made RF coil.

The mechanisms of echo combination may be explained as follows. Due to the balanced pairs of crusher gradients, free induction decays are suppressed and each detected echo is a mixture of SE based and STE based coherence pathways (*cf.* Figure 3.9, phase graph). The discussion here focuses on the lowest order SE based coherence pathway CP_{SE} and STE based coherence pathway CP_{STE}, which are main contributors to the echoes. CP_{SE} represents the pulse train of

$$90^\circ \sim 180^\circ \sim \{180^\circ\}_{n-1} \sim 180^\circ, \tag{3.4}$$

while CP_{STE} represents the pulse train of

$$90^\circ \sim 180^\circ \sim \{180^\circ\}_{n-2} \sim 90^\circ \sim 90^\circ. \tag{3.5}$$

Details of describing NMR experiments by considering coherence pathways can be found in [5, 6, 7, 8]. The main difference between both coherence pathways is that CP_{STE} experiences no gradients in the preceding inter-refocusing interval, while CP_{SE} does. For an odd echo, CP_{SE} experiences both zeroth- and first-order gradient moment nulling, due to an even number of pairs of phase encoding winder and rewinder gradients, an even number of pairs of crusher gradients, and an even number of refocusing pulses, with respect to internal magnetic field gradients. Therefore, CP_{SE} has no additional displacement introduced phase contrast. However, without experiencing gradients in the preceding inter-refocusing interval, CP_{STE} has additional phase

contrast due to non-zero first-order gradient moments. The opposite situation is found for the subsequent even echo, while only CP_{STE} instead of CP_{SE} experiences first-order gradient moment nulling. The additional phase contrast due to non-zero first-order gradient moments occur only in CP_{SE} instead of CP_{STE}. The combination of odd and even echoes is used to suppress the additional phase contrast of both coherence pathways.

It is noteworthy that velocimetry accuracy was far more improved by echo combination in 2D imaging with 1D velocimetry than in 3D imaging with 1D velocimetry. Odd or even echo alone generated incorrect VFR in the former experiments (*cf.* Figure 3.13, 3.14, and 3.18, as well as Table 3.2a and 3.3), and yielded approximately correct VFR in the latter experiments (*cf.* Figure 3.15 and 3.19c, as well as Table 3.2b and 3.4). This difference may be due to additional phase contrast originating from the slice-selection and slice-rephasing gradients, which were not discussed above. These gradients were not applied in the non-slice-selective 3D imaging experiment, but had high magnitudes in the 2D imaging experiment in order to achieve thin slices. Two types of undesired additional phase contrast were then introduced into odd and even echoes. Except for the first slice-selection gradient with the excitation pulse, the other slice-selection gradients produced the first type of additional phase contrast. Similar to the discussion for crusher gradients and internal magnetic field gradients above, this additional phase contrast can be suppressed by echo combination. The second type of additional phase contrast resulted from the first slice-selection and slice-rephasing gradients. This phase contrast had inverse polarity within the odd and even echoes in both SE and STE based coherence pathways, and thus can also be compensated by echo combination. As a result, in both 2D and 3D imaging experiments, consistent and correct VFR were obtained from offset corrected and echo combined velocity maps.

3.4.4 Data Post-processing

Because of the velocity offsets, phase wrapping can still occur even if the real velocity value is within the velocity encoding range. A considerably large $VENC$, particularly with small velocity encoding gradient magnitude, can eliminate phase wrapping. However, since the velocity STD is proportional to $VENC$ [71, 72, 73], an appropriate $VENC$, which is only slightly larger than the maximum real velocity value, is preferable. Therefore, phase unwrapping will be required if slightly higher velocities occur than expected. Moreover, it can rescue measurements for which detailed prior knowledge of the velocity distribution in tortuous structures is not available.

In this subproject, the quantitative analysis of flow was based on slice-wise

VFR values, which were obtained by integrating velocities within voxels in the same slices (*cf.* step 8 in the proposed data post-processing procedures). Errors may occur within voxels at interfaces between liquid and porous materials, since these voxels are only partially filled with liquid. However, the spatial resolution was very high ($125^2 \times 500\,\mu m^3$ in 2D and $160^3\,\mu m^3$ in 3D imaging experiments), *i.e.* the voxel size was much smaller than the mean pore size of about $2\,mm$. Thus, the partial volume effects were regarded as negligible. This integration was examined by NMR measurements of the simple laminar flow of distilled water in a tube using the Bruker coil. The VFR values calculated by integration agree with the VFR values calculated by parabolic fitting (*cf.* Figure 3.13, 3.14, and 3.15, as well as Table 3.2).

In the future, *Computational Fluid Dynamics* (CFD) studies can be performed based on the detailed knowledge on the porous structures, which can be acquired by MRI or XMT. This will allow a cross-validation between the simulated velocity fields and the velocity maps measured by the proposed RARE PC-MRI method.

3.5 Further Investigations using the Proposed RARE PC-MRI Method

The proposed RARE PC-MRI method was applied to further investigations. First, a preliminary combination with XMT on a similar porous filter for the desired deep bed filtration studies was performed. Second, feasibility of the proposed RARE PC-MRI method was surveyed on similarly templated small-pore filters, in which higher B_0 inhomogeneity will be introduced and larger inter-pore displacements of spins within the echo train will take place than in the large-pore filter.

3.5.1 Preliminary Combination with XMT

Together with the collaborator (Gerd Mikolajczyk) from the Chair of Magnetofluiddynamics, Measuring and Automation Technology, Institute of Fluid Mechanics, Technical University of Dresden, preliminary studies on deep bed filtration were performed according to the following procedures:

1. A clean porous filter sample was installed into the filtration cell and saturated by distilled water for NMR measurements.

2. Velocity maps of the slow distilled water flow through the filtration cell with a predefined pumping rate were measured by the proposed RARE PC-MRI method before deep bed filtration.

3. A series of XMT measurements were performed at discrete time points during deep bed filtration.

4. Image registration was used to combine XMT images and NMR velocity maps for further quantitative analysis of correlation between particle deposition and flow fields.

An exemplary study with a pumping rate of $63.0\,mm^3/s$ is illustrated in Figure 3.21 and 3.22. Figure 3.21 shows the evolution of particle deposition acquired by XMT, and Figure 3.22 shows the NMR velocity maps combined with the XMT images by the image registration procedures described before. Pore-wise evaluation of deep bed filtration, *e.g.* discovering pore filling factor changes *versus Reynolds numbers* of each pore, can then be applied to discover correlation between particle deposition and velocity fields.

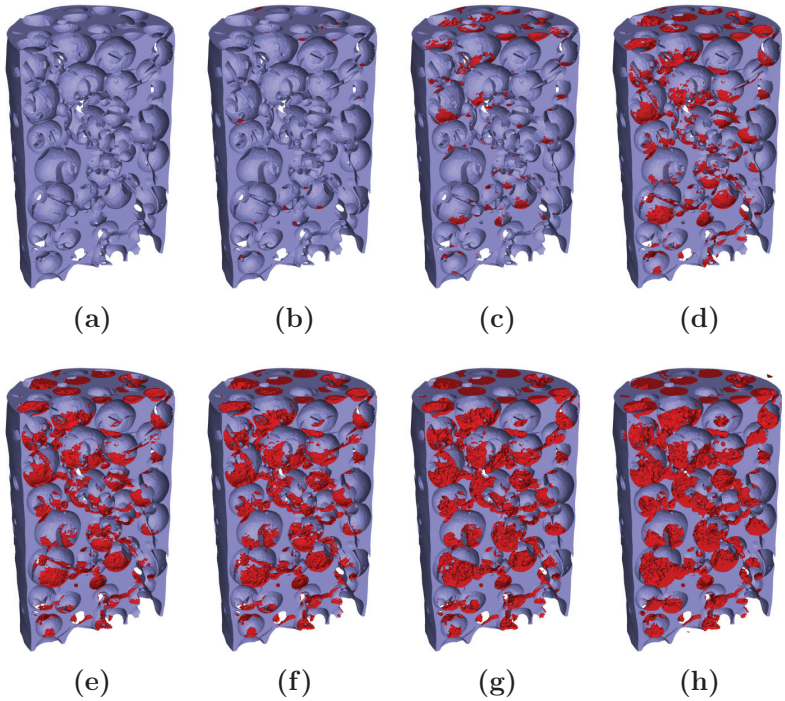

Figure 3.21: Cross-sectional rendered XMT images of the porous filter (blue) and deposited particles (red) in the deep bed filtration process at $t = 0$ (a), $7.5\,min$ (b), $15\,min$ (c), $30\,min$ (d), $60\,min$ (e), $120\,min$ (f), $240\,min$ (g), and $360\,min$ (h). Reproduced by the collaborator (Gerd Mikolajczyk) from a manuscript entitled "Colloid deposition in monolithic porous media - Experimental investigations using X-ray computed microtomography and magnetic resonance velocimetry" submitted to *J. Chem. Eng. Sci.*.

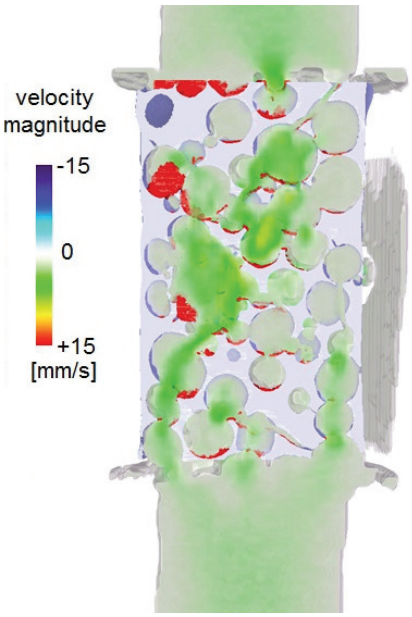

Figure 3.22: Combined XMT images and NMR velocity maps. Reproduced by the collaborator (Gerd Mikolajczyk). Deep red and deep blue regions represent deposited particles and pores, respectively.

Note that the combination of both technologies described above neglected the flow field changes during the deep bed filtration process, which is only valid when the filtration time is relatively short and no significant block of pores exists. This design of experiments was due to the fact that the collaborator with the home-made XMT scanner is not on-site. However, in the future, an additional NMR experiment may be performed at the end of the deep bed filtration process for calibration.

3.5.2 Preliminary Results on Small-pore Porous Filters using the Bruker Coil

A similarly templated porous filter with a substantially smaller mean pore size (about $0.8\,mm$) than the porous filter desired for deep bed filtration studies was used for investigating the limits of the proposed RARE PC-MRI method in the case of more inhomogeneous B_0 and larger displacements of spins within the echo train. In these preliminary experiments, the Bruker coil was used to exclude further errors originating from B_1 inhomogeneity.

With a certain pumping rate, the maximum velocity value inside this small-pore filter was estimated by multiplying the expected value inside the large-pore filter with the factor of $(2.0/0.8)^2 = 6.25$ as the square of the ratio

between the mean pore sizes of these two filters. Thus, with a pumping rate set to $12.6\,mm^3/s$, the expected maximum velocity value inside this small-pore filter was $6.25 \cdot 5 = 31.25\,mm/s$. Therefore, much shorter echo train length should be used for velocimetry on this small-pore filter.

As a starting point, 3D imaging with 1D velocimetry was still performed with a protocol similar to the protocol in studies of the large-pore sample as follows: rectangular RF pulses, τ $4.0\,ms$, effective TE $16.0\,ms$ / $24.0\,ms$ (odd / even echo), FOV $30 \times 20 \times 20\,mm^3$, matrix size $192 \times 128 \times 128$, voxel size $156 \times 156 \times 156\,\mu m^3$, read direction z, RARE phase encoding in the y-direction, N_{RARE} 16, echo train length $264.0\,ms$, t_Δ $4.0\,ms$, $VENC$ $5.0\,mm/s$, 1D velocity encoding in the z-direction, N_{VE} 2, TR $1.0\,s$, NA 2, t_{total} $2.28\,h$.

Before the measurement, several issues were expected in acquired velocities inside the small-pore filter: (i) phase wrapping due to a $VENC$ smaller than the expected maximum velocity value; (ii) erroneous velocity values because of large displacements of spins within the echo train (up to $8.25\,mm$ through the whole echo train and $0.75\,mm$ between the excitation and acquisition of the central k-space). Results of the measurement, as shown in Figure 3.23, indicate that: (i) large velocity values, which are expected inside the porous filter according to the mass conservation law, were not obtained by the proposed RARE PC-MRI method; (ii) velocity values outside the porous filter were correctly acquired only when both means of offset correction and echo combination were used (averaged $VFR_z = 12.5 \pm 1.54\,mm^3/s$).

In further measurements, the velocimetry accuracy inside the small-pore filter was not reproduced by using different voxel size ($78\,\mu m$ and $156\,\mu m$), N_{RARE} (4 and 8), $VENC$ ($2.5\,mm/s$, $7.5\,mm/s$, $10\,mm/s$, $20\,mm/s$, and $40\,mm/s$), and pumping rate ($6.3\,mm^3/s$). Velocity errors originating from phase wrapping and partial volume effects were already excluded by measurements using high 3D spatial resolution and large $VENC$. However, even with a decreased echo train length and thus reduced displacements in the echo train (*e.g.* an echo train length of $72\,ms$ with an N_{RARE} of 4, leading to displacements up to $2.25\,mm$ through the whole echo train and $0.75\,mm$ between the excitation and acquisition of the central k-space, which are close to the values in the measurement on the large-pore sample described in Section 3.3.4), the measured velocities inside the small-pore filter were still incorrect. This inaccuracy was not surprising since the inter-pore displacements in the echo train were still large (up to $2.81\,pores$ through the whole echo train and $0.94\,pores$ between the excitation and acquisition of the central k-space).

However, when the proposed RARE PC-MRI method was applied on another similar small-pore porous filter (mean pore size about $0.7\,mm$) after pore saturation by a stronger vacuum pump than before, the velocity maps

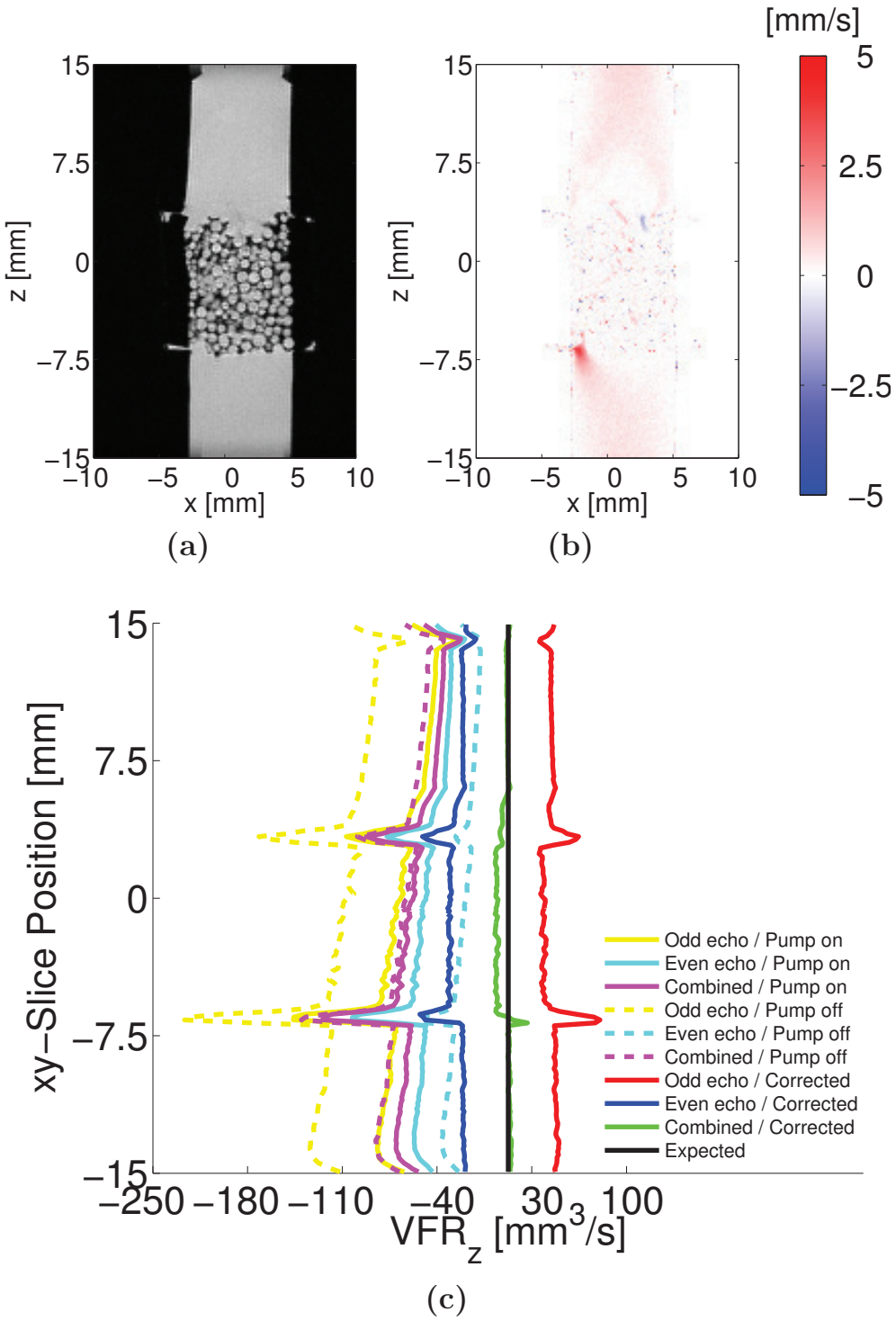

Figure 3.23: Results of 3D imaging with 1D velocimetry on a small-pore sample. (a) NMR image of the central xz-slice. (b) Longitudinal velocity (v_z) map of the central xz-slice. (c) Plot of longitudinal VFR (VFR_z) values *versus* xy-slice position.

can be correctly measured again. With a pumping rate of $47.9\,mm^3/s$, 3D imaging with 3D velocimetry was performed with the following protocol: rectangular RF pulses, τ $4.0\,ms$, effective TE $16.0\,ms$ / $24.0\,ms$ (odd / even echo), FOV $40 \times 20 \times 20\,mm^3$, matrix size $200 \times 100 \times 100$, voxel size $200 \times 200 \times 200\,\mu m^3$, read direction z, RARE phase encoding in the y-direction, N_{RARE} 10, echo train length $168.0\,ms$, t_Δ $8.0\,ms$, $VENC$ $15.0\,mm/s$, 3D velocity encoding in the x-, y- and z-directions, N_{VE} 4, TR $1.0\,s$, NA 2, t_{total} $4.44\,h$. The expected maximum velocity was $155.1\,mm/s$, leading to very large displacements of spins in the echo train.

The corresponding results are shown in Figure 3.24. The averaged longitudinal VFR (VFR_z) is $49.7 \pm 11.4\,mm^3/s$, and the representative averaged transversal VFR (VFR_y) is $-6.78 \pm 9.67\,mm^3/s$. As observed, the fluctuations in velocimetry on this small-pore sample were higher than on the large-pore sample. Surprisingly, however, the velocimetry accuracy was partially restored. This implies that: (i) estimation method for the maximum velocity value may be not applicable; (ii) thin film flow may exist as a bypass at the wall of the small-pore filters, which require higher pressure for pore saturation than the large-pore filer and thus will be saturated only with sufficiently strong vacuum pump. The reduced velocimetry accuracy may at least result from increased inter-pore displacements, particularly with more significant velocity changes in more heterogeneous systems. Experiments may be performed in the future to further validate the method on small-pore samples and investigate the influences of enhanced T_2 relaxation.

3.6 Conclusion

In this subproject, an optimized RARE PC-MRI method was proposed to achieve fast, robust and accurate velocity mapping for slow liquid flow in porous materials. NMR measurements of slow liquid flow in porous materials within a horizontal magnet are enabled by using pulse sequence modifications, particularly the combined use of odd and even echoes and an adjusted RF coil. The achievement without further investigations in Section 3.5 (*i.e.*, the combination with XMT and the experiments on small-pore samples) was published as a journal article [99], and the combination with XMT described in Section 3.5.2 was already submitted as a journal contribution. While this approach was primarily developed for studies on deep bed filtration, it may also be of interest for other NMR Velocimetry studies. In the future, the proposed method may also play an important role in studying slow liquid flow in other heterogeneous systems, such as the dissolution of pharmaceutical tablets. By modifying the SE based velocity encoding module in the

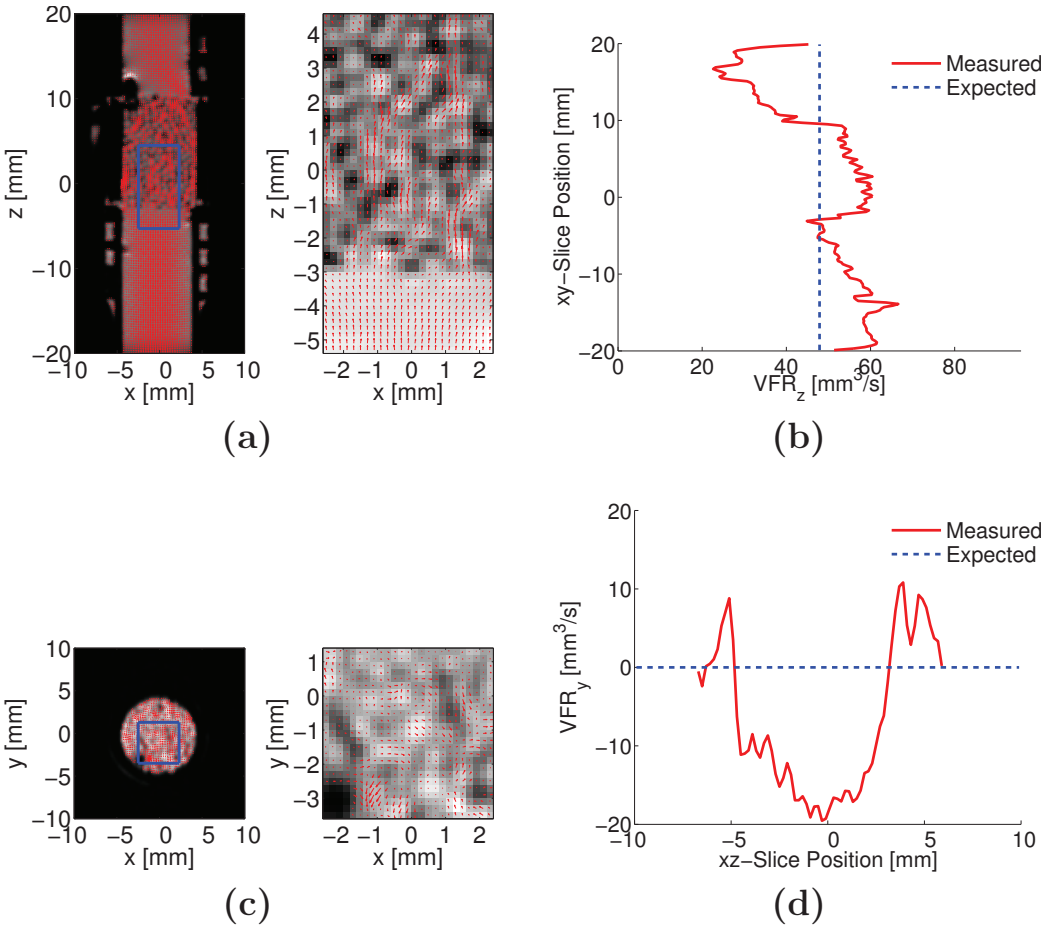

Figure 3.24: Results of 3D imaging with 3D velocimetry on another small-pore sample. (a) NMR image of the central xz-slice with overlaid velocity vector fields, and enlarged view of an image section (blue rectangle). (b) Plot of longitudinal VFR (VFR_z) *versus* xy-slice position. (d) NMR image of the central xy-slice with overlaid velocity vector fields, and enlarged view of an image section (blue rectangle). (d) Plot of transversal VFR in the y-direction (VFR_y) *versus* xz-slice position.

pulse sequence to contain velocity encoding gradients separated by multiple refocusing pulses or using STE based velocity encoding module, a relatively long t_Δ can be obtained with increased T_2 contrast for velocimetry of very slow flow, such as water uptake in porous materials.

Chapter 4

PC-MRI of Gas Flow

4.1 Introduction

Reactions in gas flow through heterogeneous catalytic reactors are used in a wide range of industrial applications, for instance reforming of natural gases and other hydrocarbons as well as air pollution prevention [100]. Studies of heat and mass transport during such processes can indicate the influences of porous structure designs (*e.g.* porosity, morphology, pore size, strut or pellet sizes) on reaction efficiency. Therefore, knowledge of gas flow patterns indicating dispersion, channeling, and dead zones in porous structures is highly desirable. This can be measured by spatially resolved NMR methods, especially spatially resolved NMR Velocimetry for measuring gas flow fields [101]. Moreover, the resulting velocity maps can be used for validation of CFD simulation on gas flow fields in heterogeneous systems.

However, MRI methods of gas flow are often restricted by the low SNR due to the low spin density, the fast transversal relaxation and the strong molecular diffusion. NMR measurements of hyperpolarized gas flow can overcome the SNR limitation by polarizing spins to states far beyond thermal equilibrium conditions [102, 103, 104, 105, 106, 107, 108]. In practice, hyperpolarization of gas nuclei is generally implemented on ^3He, ^{129}Xe, and ^{83}Kr by Spin Exchange Optical Pumping (SEOP) [102, 103, 104, 105, 106, 107, 108]. Such processes include laser induced polarization and subsequent transfer of the polarized states by exchange effects, and require dedicated devices and experimental setups such as a laser system for pumping and alkali metal for exchange. Moreover, in many cases, additional controlling of temperature and gas pressure is necessary after hyperpolarization and before the desired gas flow applications. On the other hand, these gases with such nuclei, particularly ^3He, have much narrower applications than the gases which

are easy to gain and prepare. Therefore, spatially resolved NMR methods of thermally polarized gas flow are still of great interest in many applications.

The feasibility of spatially resolved NMR Velocimetry of thermally polarized gas flow was first proven by flow studies of ^1H-containing acetylene (C_2H_2), propane (C_3H_8), and butane (C_4H_{10}) in monolithic catalysts at $B_0 = 7\,T$ [100]. Subsequently further flow studies of thermally polarized ^1H-containing gases in heterogeneous systems were published [109, 110]. More recently, the thermally polarized ^{19}F-containing sulfur hexafluoride (SF_6) attracted interest due to several NMR characteristics: high gyromagnetic ratio and large natural abundance of ^{19}F (*cf.* Table 1.1), large number of ^{19}F nuclei per molecule, and relatively slow molecular diffusion. Thus, several studies using spatially resolved NMR Velocimetry on SF_6 in porous materials were published [111, 112, 113, 114]. All these applications show the feasibility of characterization of the thermally polarized gas flow fields, the porous structures, as well as the heat and mass transport properties. Though inferior to the chemically inert sulfur hexafluoride in the NMR characteristics described above, ^1H-containing gases such as hydrocarbons are much more widely used in catalytic reactions. Therefore, spatially resolved NMR Velocimetry of thermally polarized ^1H-containing gas flow is still valuable.

In the literatures mentioned above [100, 109, 110, 111, 112, 113, 114], single- or multi-slice 2D imaging with velocimetry was usually performed, and sub-pore-scale to pore-scale anisotropic spatial resolution with small in-plane voxel size and moderate voxel size in the slice direction was achieved. In studies aiming at isotropic information of flow fields and porous structures, 3D imaging with sub-pore-scale to pore-scale isotropic spatial resolution may be more valuable. This increases the challenges of obtaining sufficiently high SNR, which can be achieved by optimizing the measurement protocols. Moreover, in previous publications [100, 109, 110, 111, 112, 113, 114], there was still no structured routine for this optimization. In this subproject, such standardized procedures were developed and applied in studies on a gas reactor.

4.2 Methods and Results

In this subproject, SE based velocity encoding was preferred over STE based velocity encoding, in order to avoid the general signal loss of 50 % in STE based pulse sequences, and PC-MRI was considered superior to q-space MRI with respect to the number of required displacement encoding steps and thus minimum measurement time. Three means were used in the proposed procedures: (i) adjusting TR and excitation FA; (ii) adjusting TE based on

T_2 and the diffusion coefficient D; (iii) phase cycling.

4.2.1 Pulse Sequence and Experimental Setup

An SE PC-MRI pulse sequence was used in this subproject. Figure 4.1 shows a diagram for non-slice-selective 3D imaging with 1D velocimetry by applying linear phase encoding in two orthogonal directions. For slice-selective 2D imaging, soft RF pulses with slice-selection and slice-rephasing gradients were used instead of hard RF pulses, and linear phase encoding was only performed in one direction. Velocity encoding gradients before and after the refocusing pulse also acted as crusher gradients, and dedicated crusher gradients could be omitted resulting in less diffusion-associated signal loss. Since strong velocity encoding gradients will lead to strong diffusion-associated signal loss, they have typically relatively small magnitudes, constraining the capability of the pulse sequence to measuring slow gas flow. In such cases, velocity offsets originating from gradient imperfections were neglected in this subproject. For more efficient suppression of the FID signals, RF phase cycling can be used as discussed later.

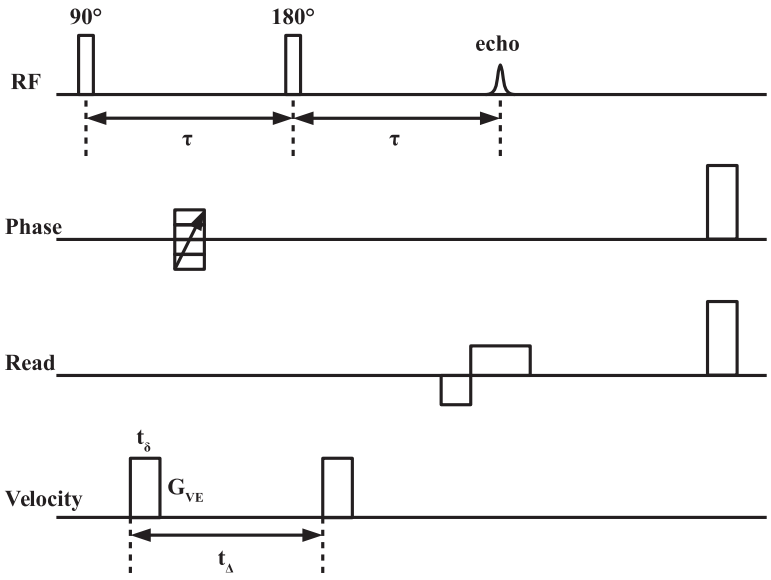

Figure 4.1: The SE PC-MRI pulse sequence for 3D imaging with 1D velocimetry, applied with linear phase encoding in two orthogonal directions. For slice-selective 2D imaging, soft RF pulses with slice-selection and slice-rephasing gradients in the slice direction are used instead of hard RF pulses, and linear phase encoding is only performed in one direction.

In this subproject, a horizontal gas reactor compatible for NMR experiments [115, 116] was used. This reactor was designed and customized by the collaborator (Jürgen Ulpts) from the Department of Chemical Engineering - Recovery and Recycling, Center for Environmental Research and Sustainable Technology, Faculty 04 (Production Engineering), University of Bremen. Porous materials, *e.g.* packed beds or porous sponges, can be mounted into the reactor bore, which has a diameter of $30\,mm$. In this subproject, the mounted materials were three cylindrical porous sponges (Hofmann Ceramics, Germany) bounded by a heat shrink tube. The sponges have a diameter of $25\,mm$, a height of $24\,mm$, an open porosity of 0.75, and a mean pore sizes of about $1.3\,mm$ (*cf.* Figure 4.2a). Gas flow can be supplied by the mass flow controllers (F-201CV, Bronkhorst, Netherlands; FMA-2618-A, Omega Engineering, USA) connected. Figure 4.2 shows the porous sponges and the gas reactor for the measurements. Nitrogen was used for system initialization before each NMR experiment and clean-up after each NMR experiment. Methane (CH_4) was used as the measured thermally polarized gas. The pressure was $1.5\,bar$ and the VFR was $2.5 \times 10^4\,mm^3/s$, supporting gas flow through the mounted porous sponges with expected maximum velocity of $250\,mm/s$. The Bruker coil was used for all NMR experiments in this subproject.

4.2.2 Optimization Procedures

Before PC-MRI, an NMR experiment for T_2 measurement was performed on a dedicated sample, which was a glass tube filled with porous sponges similar to those described above and methane with a pressure of $1.5\,bar$. The measured T_2 value was about $9.2 \pm 3.1\,ms$. The diffusion coefficient D value is $14.5\,mm^2/s$ according to literatures [117, 118].

Initially the imaging geometry was determined according to the reactor structure: FOV $96 \times 64 \times 64\,mm^3$, matrix size $120 \times 80 \times 80$, voxel size $800 \times 800 \times 800\,\mu m^3$, read direction z. And $VENC$ (*cf.* Equation 3.1) was set to $300\,mm/s$, which is moderately higher than the expected maximum velocity of $250\,mm/s$ to avoid phase wrapping. The other parameters will be derived as described in the following.

In NMR measurements, full recovery of the magnetization (*i.e.* $\rightarrow M_0$) after the signal acquisition can be achieved by using a very long TR (typically $TR > 5T_1$). In practice, a much shorter TR (smaller than or comparable to T_1) is used for the demand of minimum temporal resolution. In such cases, an optimal SNR will be yielded, if the excitation FA equals to the *Ernst Angle* α_E (typically $\alpha_E \neq 90\,^\circ$) [119]. Compared to an excitation FA of $90\,^\circ$, certain longitudinal component of the magnetization is preserved through

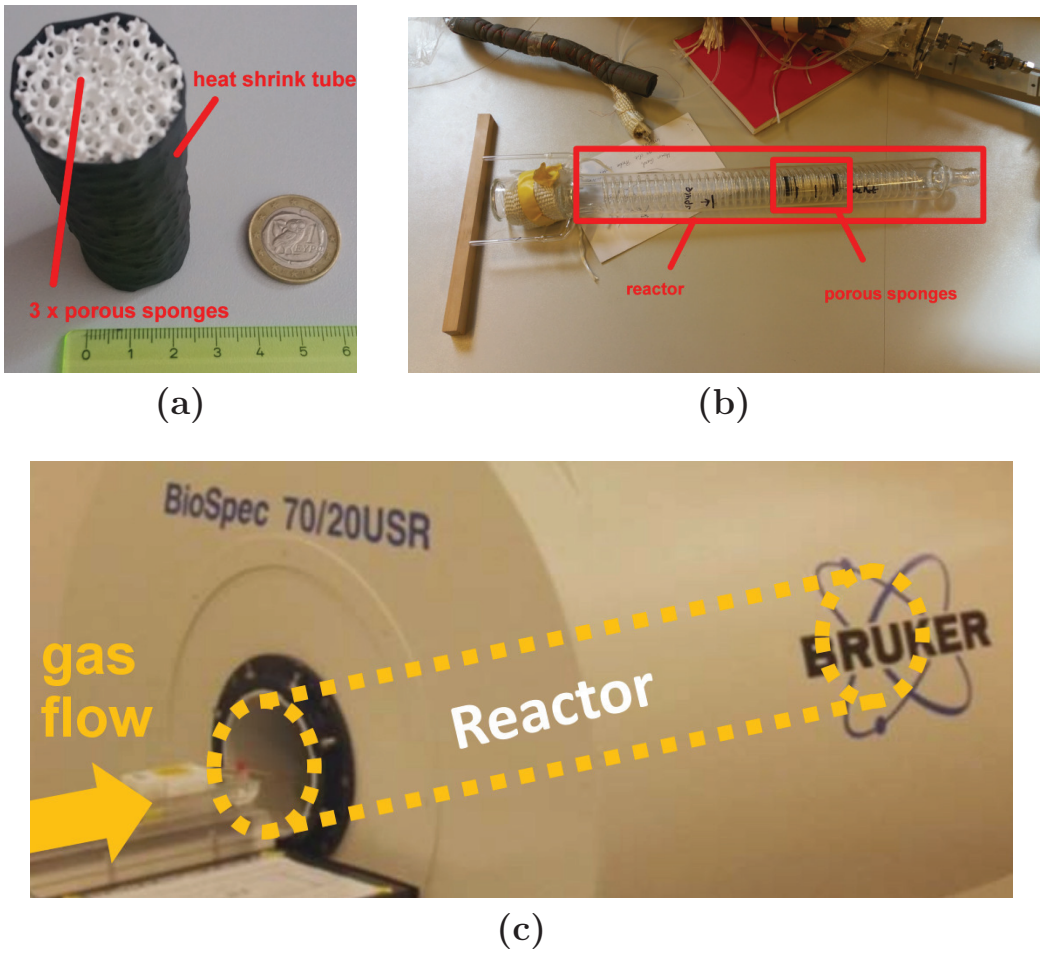

(a) (b)

(c)

Figure 4.2: (a) Photo of the porous sponges. (b) Photo of the gas reactor with mounted porous sponges. (c) Design of the gas reactor in the NMR scanner. Reproduced by the collaborator (Jürgen Ulpts).

the excitation-acquisition period with an excitation FA of α_E, resulting in a larger magnetization after the recovery delay and thus a larger transversal component of the magnetization during the signal acquisition.

In single SE NMR methods, $\alpha_E > 90\,^\circ$, *i.e.* M_z is negative after the excitation pulse with an FA of α_E and is subsequently inverted by the refocusing pulse with an FA of $180\,^\circ$, and thus positive. The theoretical dependency of signals in single SE NMR on TR and excitation FA α is given by

$$S(TR, \alpha) \propto sin\alpha \cdot \frac{1 - e^{-TR/T_1}}{1 + cos\alpha \cdot e^{-TR/T_1}}. \tag{4.1}$$

With the Ernst Angle α_E,

$$\frac{\partial S(TR, \alpha)}{\partial \alpha}|_{\alpha=\alpha_E} = 0. \tag{4.2}$$

Thus, the Ernst Angle α_E given by

$$\alpha_E = arc\,cos(-e^{-TR/T_1}) \tag{4.3}$$

is larger than $90\,^\circ$ when TR is not much longer than T_1. As a consequence, the optimal signals are given by

$$S(TR, \alpha)|_{\alpha=\alpha_E} \propto \sqrt{\frac{1 - e^{-TR/T_1}}{1 + e^{-TR/T_1}}}. \tag{4.4}$$

Before performing single SE PC-MRI measurements, the NMR signals in the spatial domain was estimated as follows:

1. The proposed SE PC-MRI pulse sequence was executed with only the read gradient switched on, and the resulting time-domain NMR signals were 1D projections of the measured object.

2. Magnitudes of the NMR signals were accumulated in the time domain, and the result was regarded as an estimate of NMR signals in the spatial domain.

This way of estimation is directly available in ParaVision 5.1.

The estimates of NMR signals in the spatial domain *versus* TR from $25\,ms$ to $250\,ms$ were measured with different excitation FA ($90\,^\circ$, $120\,^\circ$, and $150\,^\circ$), as plotted in Figure 4.3. Such limits of TR was determined due to the minimum TR and the demanded measurement time. According to Equation 4.1, the NMR signal estimate as a function of TR with an excitation FA of $90\,^\circ$ can be simplified as

$$S(TR, \alpha = 90\,^\circ) \propto (1 - e^{-TR/T_1}). \tag{4.5}$$

Thus, exponential fitting was performed on the data points measured with an excitation FA of 90°, and the resulting T_1 value was about 122 ms (*cf.* Figure 4.3, blue dashed line). According to Equation 4.1, such T_1 value agrees with the observed finding in Figure 4.3: signals with an excitation FA of 120° were stronger than signals with an excitation FA of either 90° or 150° in the TR range of $[25, 250]$ ms; and signals with an excitation FA of 150° were only stronger than signals with an excitation FA of 90° when $TR < 100$ ms.

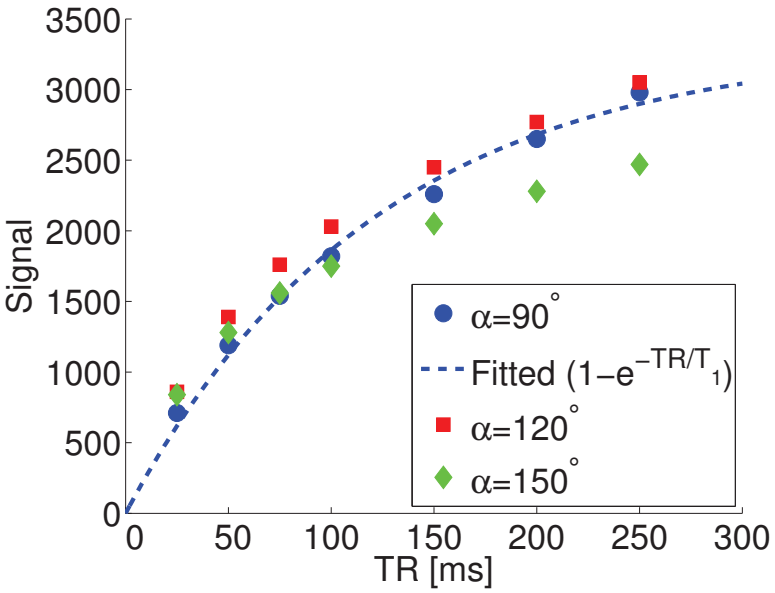

Figure 4.3: Measured estimates of NMR signals in the spatial domain *versus* TR with different excitation FA. Blue dashed line represents exponential fitting of the data points measured with an excitation FA of 90°, and the resulting T_1 value was about 122 ms.

Equation 4.4 and Figure 4.3 indicate that, no matter how large an excitation FA is, a prolonged TR will lead to an improved SNR in a single measurement. In practice, signal averaging of repetitive measurements can be applied, *i.e.* $NA > 1$, to increase the SNR. The measurement time will then certainly be prolonged, but the temporal resolution can still be maintained when a moderate NA is used. The *signal efficiency* S_t, defined as the NMR signals obtained per unit measurement time, was used as a measure of SNR improvement by signal averaging of repetitive measurements. It can be given by

$$S_t(TR, \alpha) \propto \frac{S(TR, \alpha)}{\sqrt{TR}} \propto \frac{sin\alpha \cdot (1 - e^{-TR/T_1})}{\sqrt{TR} \cdot (1 + cos\alpha \cdot e^{-TR/T_1})}. \tag{4.6}$$

The corresponding simulation of the signal efficiency S_t *versus* TR with different excitation FA is illustrated in Figure 4.4. An optimal SNR can be gained when a large excitation FA ($\geqslant 120\,^\circ$) and a short TR ($< 100\,ms$) are used. Moreover, with an increased excitation FA, the TR should be shortened for an optimal SNR (*cf.* Equation 4.3).

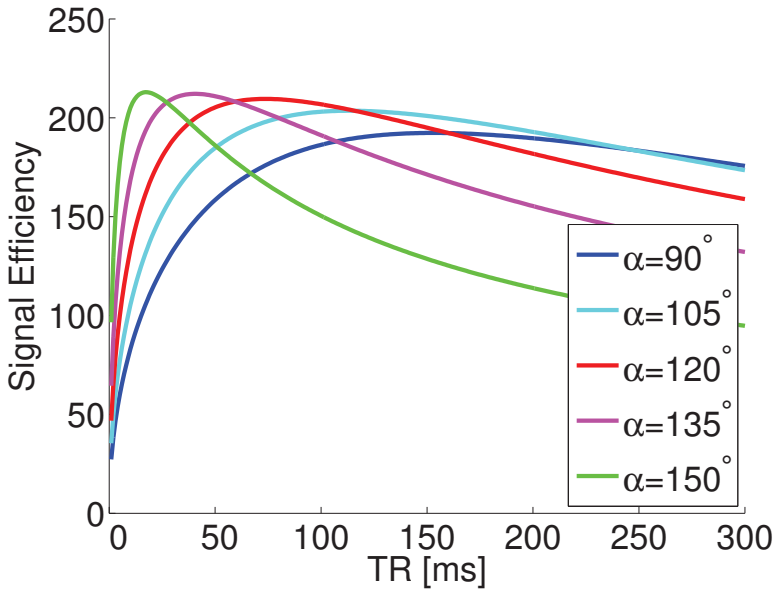

Figure 4.4: Simulated efficiency of NMR signals in the spatial domain *versus* TR with different excitation FA.

According to Equation 4.6, the signal efficiency was then calculated based on the measured data (*cf.* Figure 4.3). The results are plotted as the solid markers in Figure 4.5. On the other hand, the simulated signal efficiency *versus* TR with the same excitation FA ($90\,^\circ$, $120\,^\circ$, and $150\,^\circ$) are plotted as dashed lines in Figure 4.5. They are the same as solid lines in Figure 4.4 with identical colors. With an excitation FA of $90\,^\circ$ or $120\,^\circ$, the measured signal efficiency generally agree with the simulated values. However, with an excitation FA of $150\,^\circ$, the predicated signals deviated from the measured data. This may be explained as consequences of different T_1 values in bulk volume and at surfaces [38], B_1 inhomogeneity (particularly severe with a large FA for such a large FOV), or signal offsets due to noise from electronics.

Based on both measured and simulated signal efficiency values (*cf.* Figure 4.5), to achieve the optimal SNR, the excitation FA should be about $120\,^\circ$, and the corresponding TR values could be between $50\,ms$ and $75\,ms$. In this subproject, TR was determined as $50\,ms$. Simulated according to Equation 4.1, the signal estimates also proportional to the signal efficiency are plotted

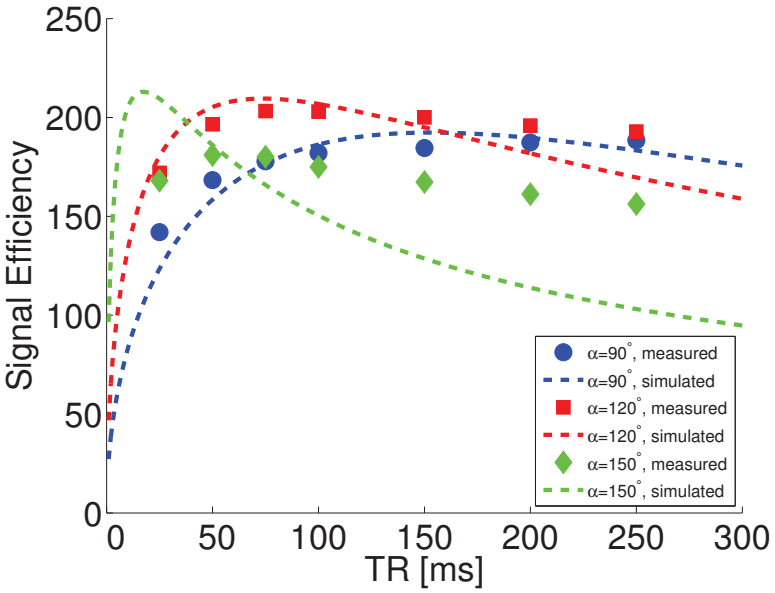

Figure 4.5: Measured and simulated efficiency of NMR signals in the spatial domain *versus* TR with different excitation FA. Dashed lines represent simulation results and are the same as solid lines in Figure 4.4 with identical colors.

in Figure 4.6 as a function of the excitation FA with such TR ($50\,ms$) and given T_1 ($122\,ms$). The corresponding Ernst Angle is $\alpha_E = 132\,^\circ$ according to Equation 4.3. In practice, further signal estimation as described above was performed with different excitation FA by changing the RF transmission power with a step length of $0.5\,dB$ and an initial value for an excitation FA of $90\,^\circ$. Finally, maximum signals were found at $+3.0\,dB$, resulting in an excitation FA of $127\,^\circ$ close to $\alpha_E = 132\,^\circ$ and thus leading to an SNR improvement of about $33\,\%$ compared to the SNR with an excitation FA of $90\,^\circ$ (*cf.* Figure 4.6).

The next step for optimization was to find a compromise between signal decays by T_2 relaxation ($\propto e^{-TE/T_2}$) and diffusion ($\propto e^{-b\cdot D}$), *i.e.*

$$S(TE, b) \propto e^{-\frac{TE}{T_2} - b\cdot D}. \tag{4.7}$$

The signal decay by T_2 relaxation can be reduced with a shortened TE, which decreases the upper limit of the delay between velocity encoding gradients t_Δ. With a shorter t_Δ, a stronger velocity encoding gradient magnitude G_{VE} is required for maintaining the $VENC$ (*cf.* Equation 3.1), thus leading to the larger signal decay by diffusion. *Vice versa*, a prolonged t_Δ allows a weakened G_{VE} for the reduced signal decay by diffusion, but increases the

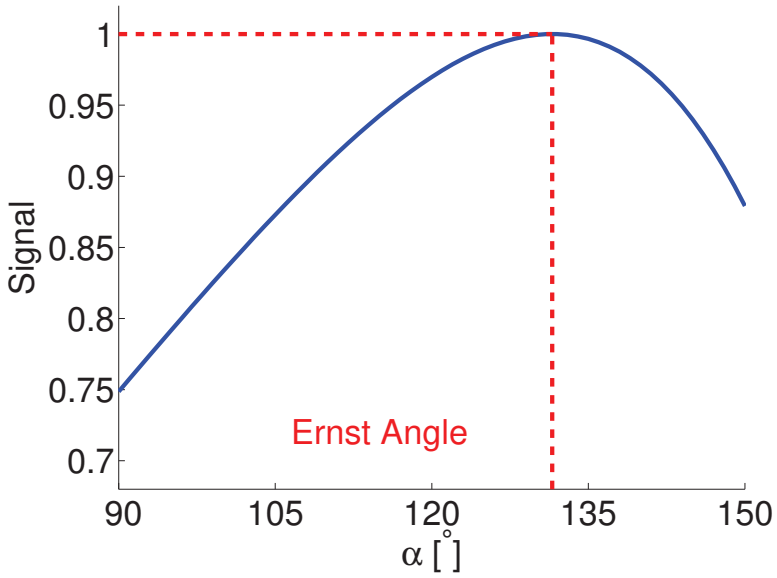

Figure 4.6: Simulated estimates of NMR signals in the spatial domain *versus* excitation FA with $TR = 50\,ms$ and $T_1 = 122\,ms$ according to Equation 4.1. The values are normalized to the maximum. Red dashed lines indicate the Ernst Angle $\alpha_E = 132\,°$.

lower limit of TE, thus resulting in the larger signal decay by T_2 relaxation. A simplified relation between TE and t_Δ was assumed for further discussion, and will be described in the following.

Except for the mandatory gradients for spatial encoding (*i.e.* frequency encoding and phase encoding gradients), the signal decay by diffusion originates from the diffusion-sensitizing velocity encoding gradients. Therefore, the b value [120] is given by

$$b \simeq (N_{VE} - 1) \cdot (\gamma G_{VE} t_\delta)^2 \cdot (t_\Delta - \frac{t_\delta}{3}), \tag{4.8}$$

with the factor $(N_{VE} - 1)$ indicating that velocity encoding gradients are applied in one direction for 1D velocimetry or in three orthogonal directions for 3D velocimetry (*cf.* Subsection 3.3.1). Thus, for minimizing the b value, reducing t_δ is more efficient than reducing t_Δ. In this subproject, t_δ was at least four times smaller than t_Δ, so that $t_\Delta \gg \frac{t_\delta}{3}$. The b value can then be simplified as

$$b \simeq (N_{VE} - 1) \cdot (\gamma G_{VE} t_\delta)^2 \cdot t_\Delta. \tag{4.9}$$

With a certain $VENC$ (*cf.* Equation 3.1), the b value can then be given by

$$b \simeq (N_{VE} - 1) \cdot (\frac{\pi}{N_{VE} \cdot VENC})^2 \cdot \frac{1}{t_\Delta}. \tag{4.10}$$

On the other hand, t_Δ should be maximized if a certain TE is used. Therefore, in the pulse sequence, the first velocity encoding gradient was switched on immediately after the end of the excitation pulse, and dephasing in the read direction was applied immediately after the second velocity encoding gradient was switched off. The simplified relation between t_Δ and TE can then be given by

$$TE = t_\Delta + t_{other} \tag{4.11}$$

with t_{other} equals to the sum of all other durations and delays. t_{other} was regarded as constant, when the excitation pulse duration, t_δ, frequency encoding parameters (*i.e.* FOV, matrix size and BW_{acq}) and thus dephasing and frequency encoding gradients in the read direction were determined. Therefore, TE was approximately proportional to t_Δ, *i.e.*

$$TE \propto t_\Delta \tag{4.12}$$

According to Equation 4.7, 4.10, and 4.12, the NMR signals with decays by T_2 relaxation and diffusion can be described as a function of t_Δ, given by

$$S(t_\Delta) \propto \sqrt{N_{VE}} \cdot e^{-\frac{t_\Delta}{T_2} - (N_{VE}-1)\cdot(\frac{\pi}{N_{VE}\cdot VENC})^2 \cdot \frac{D}{t_\Delta}} \tag{4.13}$$

with the factor $\sqrt{N_{VE}}$ representing the SNR improvement due to signal averaging of N_{VE} measurements. The signals will have the minimum loss if

$$\frac{\partial S(t_\Delta)}{\partial t_\Delta}\Big|_{t_\Delta = t_\Delta^{(opt)}} = 0, \tag{4.14}$$

i.e.

$$t_\Delta^{(opt)} = \sqrt{N_{VE}-1} \cdot \frac{\pi}{N_{VE}\cdot VENC} \cdot \sqrt{D \cdot T_2}. \tag{4.15}$$

The signals with the minimum loss can be given by

$$S(t_\Delta)\big|_{t_\Delta = t_\Delta^{(opt)}} \propto \sqrt{N_{VE}} \cdot e^{-\sqrt{N_{VE}-1}\cdot\frac{2\pi}{N_{VE}\cdot VENC}\cdot\sqrt{\frac{D}{T_2}}}, \tag{4.16}$$

With $VENC = 300\,mm/s$, $D = 14.5\,mm^2/s$, and $T_2 = 9.2\,ms$, the simulated signals (*cf.* Equation 4.13) are plotted *versus* t_Δ simulated according to Equation 4.13 are plotted in Figure 4.7. The $t_\Delta^{(opt)}$ value calculated according to Equation 4.16 was $1.65\,ms$. As shown in Figure 4.7, the attenuation of signals with an increasing t_Δ in the range of $t_\Delta > t_\Delta^{(opt)}$ is less significant than the attenuation of signals with an decreasing t_Δ in the range of $t_\Delta < t_\Delta^{(opt)}$. For instance, if $t_\Delta = 0.65\,ms$, which is $1\,ms$ shorter than $t_\Delta^{(opt)}$, the signal loss compared to the optimal signals will then be about 15 %, while

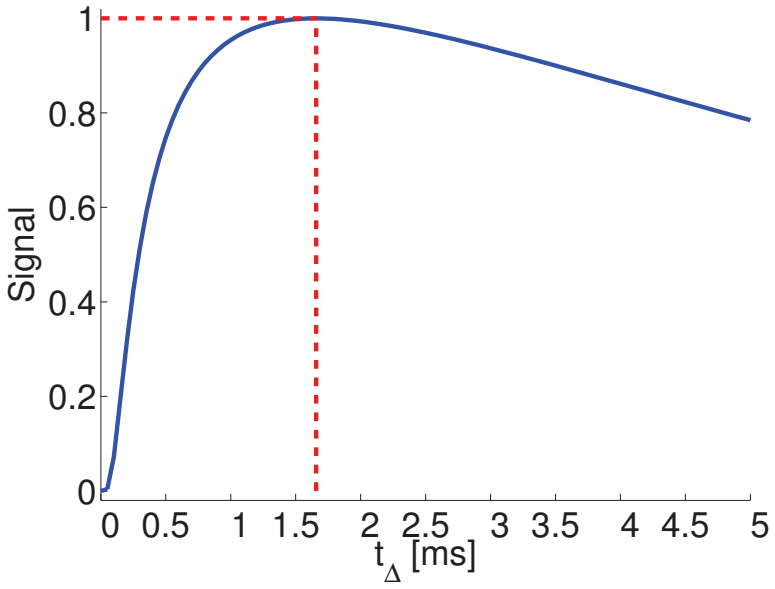

Figure 4.7: NMR signals *versus* t_Δ simulated according to Equation 4.13 with $t_{other} = const$ and normalized to the maximum. Red dashed lines represent the minimum signal loss when $t_\Delta = t_\Delta^{(opt)}$.

if $t_\Delta = 2.65\,ms$, which is $1\,ms$ longer than $t_\Delta^{(opt)}$, the signal loss compared to the optimal signals will only be about $4\,\%$.

After the two procedures described above, the excitation FA, TR, and t_Δ were determined in the measurement protocol: excitation FA $127\,^\circ$, TR $50\,ms$, t_Δ $1.65\,ms$. The rest of measurement parameters were: TE $3.15\,ms$, NA 8, measurement time $2.84\,h$.

The last optimization procedure was improving phase cycling. A simple two-step phase cycle for the excitation pulse was initially used(*cf.* Table 4.1a), however, leading to image artifacts (*cf.* Figure 4.8a). This was interpreted as inefficient suppression of FID signals of the excitation pulse due to the refocusing pulse whose FA was not exactly $180\,^\circ$ because of B_1 inhomogeneity. Therefore, a simple four-step phase cycle (*cf.* Table 4.1b) was used instead, and the image artifacts with stripe patterns (*cf.* Figure 4.8a, particularly in the bulk volume regions at the edges in the z-direction) were efficiently suppressed (*cf.* Figure 4.8b). Note that the curved regions at the edges in the z-direction do not represent the real structures in the gas reactor but are due to the nonlinearity of gradients. The bright regions at the edges in the x- and y-directions as a hollow cylinder surrounding the gas reactor, represent the sealing cord made of glass fiber and used between the gas reactor and the Bruker coil.

Table 4.1: Phase cycling schemes in this subproject.

step	excitation	refocusing	acquisition
1	0 °	90 °	0 °
2	180 °	90 °	180 °

(a) A simple two-step phase cycle for the excitation pulse, corresponding NMR images in Figure 4.8a.

step	excitation	refocusing	acquisition
1	0 °	90 °	0 °
2	180 °	90 °	180 °
3	180 °	180 °	0 °
4	0 °	180 °	180 °

(b) A simple four-step phase cycle for both the excitation and refocusing pulses, corresponding NMR images in Figure 4.8b.

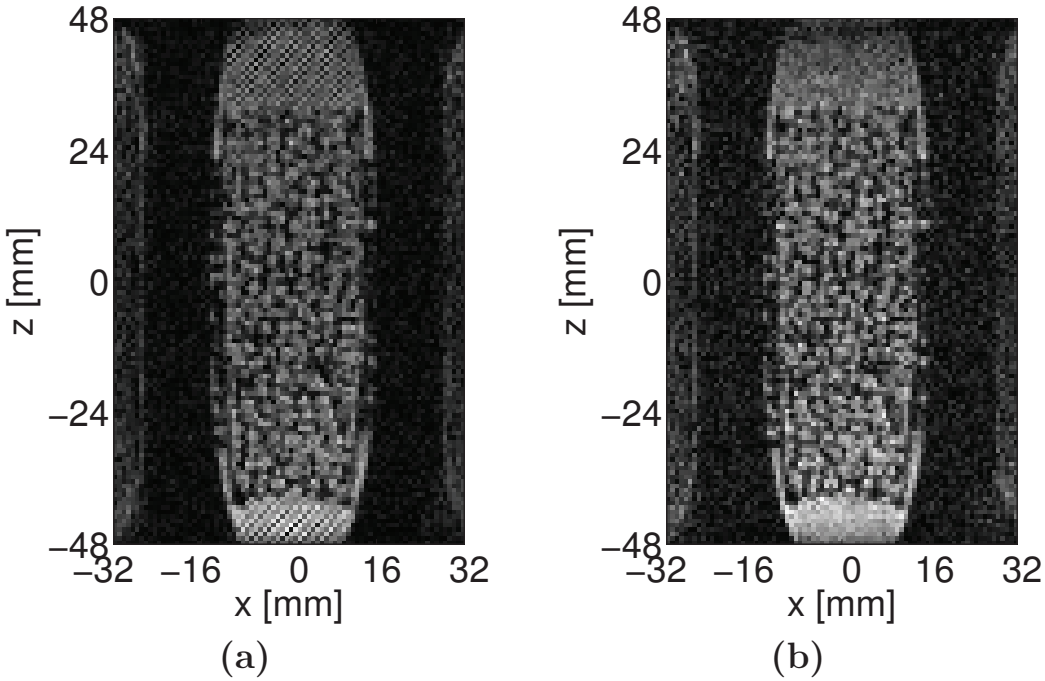

Figure 4.8: NMR images of methane in the gas reactor with the two-step phase cycle illustrated in Table 4.1a (a) and with the four-step phase cycle illustrated in Table 4.1b (b). Image artifacts with stripe patterns (particularly in the bulk volume regions at the edges in the z-direction) can only be found in (a).

Applying all of the above optimization procedures, 3D imaging with 3D velocimetry can yield moderate SNR and is able to measure the velocity maps of thermally polarized methane flow in porous sponges. Results are displayed in Figure 4.9, in which only the central region of the images ($48\times32\times32\,mm^3$) is displayed.

Otsu's thresholding algorithm [43] was applied for binary masking of the NMR images. Voxels within the mask were regarded as methane-containing voxels, through which methane was flowing. The SNR, which was estimated by comparing the mean image intensities of methane-containing voxels in the central region of the gas reactor and the STD of image intensities of voxels outside the gas reactor, was about 23.

Due to the pore-scale spatial resolution, the quantitative analysis of velocimetry accuracy was not based on slice-wise VFR. Instead, it was based on statistics of averaged velocities of methane-containing voxels in two regions: the porous sponges (a horizontal cylinder with a diameter of $25\,mm$), and the sealing cord between the porous sponges and the inner surface of the reactor bore (a hollow horizontal cylinder with a wall thickness of $2.5\,mm$). They form the whole region of the gas reactor (a horizontal cylinder with a diameter of $30\,mm$). These two cylindrical regions as well as the Bruker coil were assumed as coaxial in the following quantitative analysis. Additionally, for compensating partial volume effects, voxel-wise weighting based on NMR image intensities was performed when calculating the averaged velocities. The corresponding results are summarized in Table 4.2.

Table 4.2: Statistics results of averaged velocities in different regions.

region	$\bar{v_x}\,[mm/s]$	$\bar{v_y}\,[mm/s]$	$\bar{v_z}\,[mm/s]$
porous sponges	-0.875 ± 1.45	-1.71 ± 0.795	56.6 ± 4.19
sealing cord	-1.47 ± 2.37	-2.28 ± 1.78	5.33 ± 9.47

(a) Results of non-weighted calculation.

region	$\bar{v_x}\,[mm/s]$	$\bar{v_y}\,[mm/s]$	$\bar{v_z}\,[mm/s]$
porous sponges	-0.840 ± 1.35	-1.72 ± 0.721	60.8 ± 3.87
sealing cord	-1.31 ± 2.14	-2.19 ± 1.58	6.15 ± 9.96

(b) Results of weighted calculation.

No transversal net flow in the porous sponges and the sealing cord was observed corresponding to the low averaged velocity components in the x- and y-directions. Compared to the averaged velocity component in z-direction in the region of the porous sponges, the averaged velocity component in z-direction in the region of the sealing cord was non-negligible, implying a

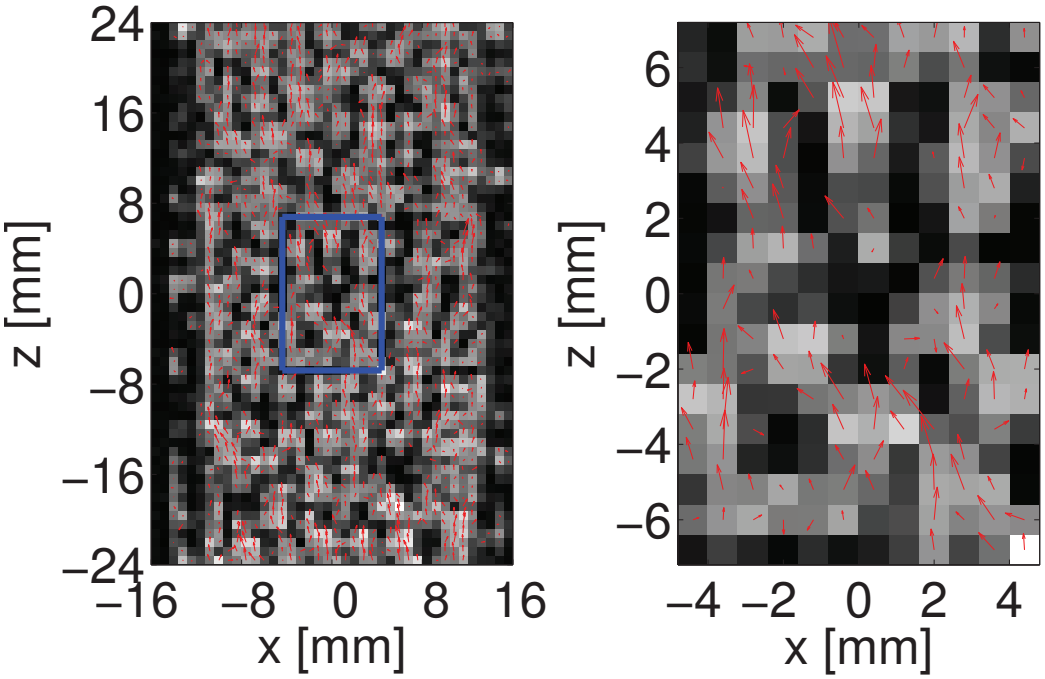

(a)

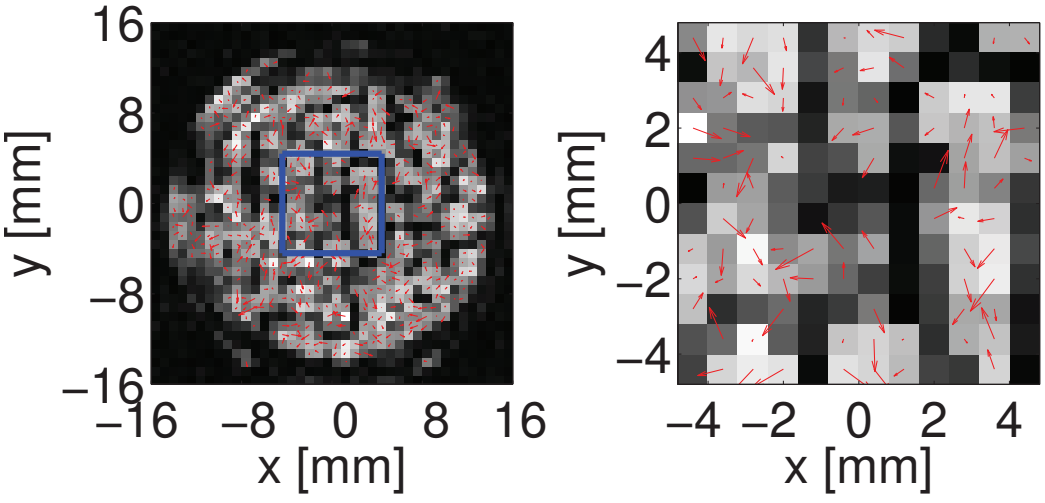

(b)

Figure 4.9: Results of 3D imaging with 3D velocimetry. (a) NMR image of the central xz-slice with overlaid velocity vector fields and enlarged view of an image section (blue rectangle). (b) NMR image of the central xy-slice with overlaid velocity vector fields and enlarged view of an image section (blue rectangle).

possible bypass of methane flow through this region.

With the open porosity (0.75) of the porous sponges, the VFR through the region of porous sponges can be calculated by

$$VFR = \bar{v} \cdot \pi(\frac{diameter}{2})^2 \cdot open\ porosity. \tag{4.17}$$

The calculated VFR through this region was $(2.08 \pm 0.154) \cdot 10^4\, mm^3/s$ using non-weighted averaged velocity, and $(2.24 \pm 0.142) \cdot 10^4\, mm^3/s$ using weighted averaged velocity. While the latter value is closer to the expected VFR of $2.5 \cdot 10^4\, mm^3/s$, there was still a loss of about 10 %, indicating a bypass of methane flow through the region of the sealing cord. However, without knowledge of porosity of the sealing cord, the calculation of VFR through the corresponding region is not possible.

The velocimetry accuracy of the proposed method was examined later by performing the pulse sequence with the same measurement protocol on a dedicated sample, which is a glass tube filled with methane of the same pressure ($1.5\, bar$) as in the experiment mentioned above. Based on quantitative analysis, very small averaged velocities in three directions ($\bar{v_x} = 1.96 \pm 1.72\, mm/s$, $\bar{v_x} = -0.830 \pm 1.59\, mm/s$, and $\bar{v_z} = 1.32 \pm 0.847\, mm/s$) show that there was no net flow in the sealed sample.

4.3 Conclusion

In this subproject, standardized procedures for adjusting the measurement protocol in single SE PC-MRI of thermally polarized gas flow through porous materials were proposed. With such structured routines, velocity maps of gas flow can be obtained with moderate SNR, supporting studies of porous structures in reactors as well as mass transport in catalytic reactions involving thermally polarized ^1H-containing gas flow. A manuscript as an expected journal contribution on this subproject is in preparation. In the future, CFD simulation on gas flow fields in heterogeneous systems may be combined for cross-validation of both technologies as well as more profound knowledge of catalytic gas reactions.

Chapter 5

General Conclusion

In this work, spatially resolved NMR methods at $B_0 = 7\,T$ were improved and optimized for the characterization of mass transport processes including drying and flow in porous materials, which are often opaque and thus do not allow the use of optical imaging technologies. The general challenges for measuring fluids in such heterogeneous systems by NMR techniques are the strong magnetic susceptibility effects at the interfaces between heterogeneous matter, the non-negligible B_0 inhomogeneity, and the significant signal decay due to transversal relaxation of magnetization. Adequate temporal resolution is also demanded for monitoring the changes of the heterogeneous systems, which is particularly difficult to achieve when high 3D spatial resolution is also required. The measured NMR images with the desired contrast not only can provide information of the porous structures, but also will lead to deeper understanding of mechanisms underlying the corresponding dynamic processes in porous materials, thus allowing improvements on system designs.

Employed in a variety of applications, drying in porous materials represents liquid removal by evaporation and notably influences the final product quality. Measured by MRI, the information of the evolution of liquids in such materials can help to improve production procedures. In this work, ZTE MRI with predominant spin density contrast and negligible signal decay by T_2^* relaxation was used for drying studies. The existing wave-pattern image artifacts in ZTE MRI, which do not occur in conventional MRI, were investigated. Such artifacts proved to be unrelated to missing points in ZTE MRI, but mainly originate from the background signals of the ^1H-containing RF coil, which due to short T_2^* are not measured in conventional MRI. Two strategies were used for an efficient suppression of the background signals. The first strategy was saturating slices in the outer volume for magnetization preparation, and the second strategy was the use of a ^1H-free RF coil. When such an optimized RF coil is available, the second strategy is preferable for

avoiding limitations of the OVS module, such as increased RF heating and gradient duty cycle, as well as prolonged measurement time. In the future, ZTE MRI may also be used for other applications, such as monitoring liquid uptake in porous materials. With certain limitations like a centered FOV encompassing the whole object to be measured, these studies can still benefit from advantages including high 3D spatial resolution with short or moderate measurement time, as well as minimized T_2^* contrast and predominant spin density contrast.

Deep bed filtration is widely applied for clarifying suspensions, which are slowly streaming downwards through the porous filter. Spatially resolved NMR Velocimetry of the associated liquid flow can help to understand the movement and immobilization of the particles, thus leading to an improved filter design with regard to filtration efficiency. In this work, an optimized RARE PC-MRI method was proposed to achieve fast and accurate velocity mapping for slow liquid flow in porous materials. A dedicated RF coil with a high filling factor was constructed considering the limited space available for a vertical filtration cell in a horizontal NMR scanner, however, introducing non-negligible $\boldsymbol{B}_1$ inhomogeneity. Several means including phase cycling, centric phase encoding, and an Hadamard scheme for velocity encoding were applied to optimize the RARE PC-MRI pulse sequence for accurately measuring the displacement introduced phase contrast in a long echo train, even in the case of a low $\boldsymbol{B}_1$ homogeneity. Two means were of particular importance. One was the use of data acquired with zero flow to correct the phase contrast offsets from gradient imperfections, and the other was the combination of the phase contrast from signals of both odd and even echoes. The proposed RARE PC-MRI method was combined with XMT for studies on deep bed filtration to investigate the correlation between particle deposition and liquid flow fields, and may play an important role in studying liquid flow in other heterogeneous systems, such as the dissolution of pharmaceutical tablets.

Gas flow patterns in heterogeneous catalytic reactors may help to indicate the influences of porous structure designs on reaction efficiency, and can be measured by MRI. Though having broad applications, thermally polarized gases exhibit several drawbacks in MRI experiments: low spin density, rapid transversal relaxation, and strong molecular diffusion. They all restrict the use of MRI because of low SNR. In this work, standardized procedures for adjusting the measurement protocol in single SE PC-MRI of thermally polarized gas flow through porous materials were proposed. Three means were used in the proposed procedures: adjusting TR and excitation FA; adjusting TE based on T_2 and D; and employing phase cycling. With such structured routines, velocity maps of the gas flow can be measured with moderate SNR, supporting studies of porous structures in gas reactors as well as mass trans-

port in the associated catalytic gas reactions.

In the future, some acceleration strategies like Compressed Sensing may further improve the temporal resolution. Moreover, CFD simulation may be used for cross-validation between the simulation and the proposed PC-MRI methods for flow studies.

Bibliography

[1] Paul T. Callaghan. *Principles of Nuclear Magnetic Resonance Microscopy*. Oxford Science Publications. Clarendon Press, revised edition, 1993.

[2] Matt A. Bernstein, Kevin F. King, and Xiaohong Joe Zhou, editors. *Handbook of MRI Pulse Sequences*. Academic Press, 2004.

[3] Siegfried Stapf and Song-I Han, editors. *NMR Imaging in Chemical Engineering*. Wiley-VCH, 2006.

[4] Robert W. Brown, Yu-Chung N. Cheng, E. Mark Haacke, Michael R. Thompson, and Ramesh Venkatesan. *Magnetic Resonance Imaging: Physical Principles and Sequence Design*. Wiley-Blackwell, 2nd edition, 2014.

[5] Jürgen Hennig. Multiecho imaging sequences with low refocusing flip angles. *J. Magn. Reson.*, 78(3):397–407, 1988.

[6] Jürgen Hennig. Echoes - how to generate, recognize, use or avoid them in MR-imaging sequences. Part I: Fundamental and not so fundamental properties of spin echoes. *Concepts Magn. Reson., Part A*, 3(3):125–143, 1991.

[7] Jürgen Hennig. Echoes - how to generate, recognize, use or avoid them in MR-imaging sequences. Part II: Echoes in imaging sequences. *Concepts Magn. Reson., Part A*, 3(4):179–192, 1991.

[8] Klaus Scheffler. A pictorial description of steady-states in rapid magnetic resonance imaging. *Concepts Magn. Reson., Part A*, 11(5):291–304, 1999.

[9] A. A. Maudsley. Modified Carr-Purcell-Meiboom-Gill sequence for NMR Fourier imaging applications. *J. Magn. Reson.*, 69(3):488–491, 1986.

[10] Terry Gullion, David B. Baker, and Mark S. Conradi. New, compensated Carr-Purcell sequences. *J. Magn. Reson.*, 89(3):479–484, 1990.

[11] Malcom H. Levitt, Ray Freeman, and Thomas Frenkiel. Broadband decoupling in high-resolution nuclear magnetic resonance spectroscopy. *Adv. Magn. Reson.*, 11:47–110, 1983.

[12] Yi-Qiao Song. Magnetic Resonance of Porous Media (MRPM): A perspective. *J. Magn. Reson.*, 229:12–24, 2013.

[13] Andriy Fedorov, Reinhard Beichel, Jayashree Kalpathy-Cramer, Julien Finet, Jean-Christophe Fillion-Robin, Sonia Pujol, Christian Bauer, Dominique Jennings, Fiona Fennessy, Milan Sonka, John Buatti, Stephen Aylward, James V. Miller, Steve Pieper, and Ron Kikinis. 3D Slicer as an image computing platform for the Quantitative Imaging Network. *Magn. Reson. Imaging*, 30(9):1323–1341, 2012.

[14] Igor V. Koptyug. MRI of mass transport in porous media: Drying and sorption processes. *Prog. Nucl. Magn. Reson. Spectrosc.*, 65:1–65, 2012.

[15] Jim C. Elliott and S. D. Dover. X-ray microtomography. *J. Microsc.*, 126(2):211–213, 1982.

[16] S. R. Stock. Recent advances in X-ray microtomography applied to materials. *Int. Mater. Rev.*, 53(3):129–181, 2008.

[17] S. Emid and J. H. N. Creyghton. High resolution NMR imaging in solids. *Physica B+C*, 128(1):81–83, 1985.

[18] Bruce J. Balcom, R. P. Macgregor, S. D. Beyea, D. P. Green, R. L. Armstrong, and T. W. Bremner. Single-Point Ramped Imaging with T1 Enhancement (SPRITE). *J. Magn. Reson., Ser. A*, 123(1):131–134, 1996.

[19] Markus Weiger and Klaas P. Pruessmann. MRI with zero echo time. *eMagRes*, 1(2):311–322, 2012.

[20] S. Hafner. Fast imaging in liquids and solids with the Backprojection Low Angle ShoT (BLAST) technique. *Magn. Reson. Imaging*, 12(7):1047–1051, 1994.

[21] David P. Madio and Irving J. Lowe. Ultra-fast imaging using low flip angles and FIDs. *Magn. Reson. Med.*, 34(4):525–529, 1995.

[22] David P. Madio, H. Michael Gach, and Irving J. Lowe. Ultra-fast velocity imaging in stenotically produced turbulent jets using RUFIS. *Magn. Reson. Med.*, 39(4):574–580, 1998.

[23] Dean O. Kuethe, Arvind Caprihan, Eiichi Fukushima, and R. Allen Waggoner. Imaging lungs using inert fluorinated gases. *Magn. Reson. Med.*, 39(1):85–88, 1998.

[24] Y. Wu, Jerome L. Ackerman, D. A. Chesler, J. Li, R. M. Neer, J. Wang, and M. J. Glimcher. Evaluation of bone mineral density using three-dimensional solid state phosphorus-31 NMR projection imaging. *Calcif. Tissue Int.*, 62(6):512–518, 1998.

[25] Chandrasekhar Ramanathan and Jerome L. Ackerman. Quantitative solid-state NMR imaging of synthetic calcium phosphate implants. *Magn. Reson. Med.*, 41(6):1214–1220, 1999.

[26] Markus Weiger, Klaas P. Pruessmann, and Franciszek Hennel. MRI with zero echo time: Hard versus sweep pulse excitation. *Magn. Reson. Med.*, 66(2):379–389, 2011.

[27] Florian Wiesinger, Laura I. Sacolick, Anne Menini, Sandeep S. Kaushik, Sangtae Ahn, Patrick Veit-Haibach, Gaspar Delso, and Dattesh D. Shanbhag. Zero TE MR bone imaging in the head. *Magn. Reson. Med.*, 75(1):107–114, 2016.

[28] Gaspar Delso, Florian Wiesinger, Laura I. Sacolick, Sandeep S. Kaushik, Dattesh D. Shanbhag, Martin Hüllner, and Patrick Veit-Haibach. Clinical evaluation of zero-echo-time MR imaging for the segmentation of the skull. *J. Nucl. Med.*, 56(3):417–422, 2015.

[29] Dana C. Peters, J. Andrew Derbyshire, and Elliott R. McVeigh. Centering the projection reconstruction trajectory: Reducing gradient delay errors. *Magn. Reson. Med.*, 50(1):1–6, 2003.

[30] Tanja Yvonne Klein, Laura Treccani, and Kurosch Rezwan. Ceramic microbeads as adsorbents for purification technologies with high specific surface area, adjustable pore size, and morphology obtained by ionotropic gelation. *J. Am. Ceram. Soc.*, 95(3):907–914, 2012.

[31] Thomas C. Schumacher, Tanja Yvonne Klein, Laura Treccani, and Kurosch Rezwan. Rapid sintering of porous monoliths assembled from microbeads with high specific surface area and multimodal porosity. *Adv. Eng. Mater.*, 16(2):151–155, 2014.

[32] Dean O. Kuethe, Arvind Caprihan, Irving J. Lowe, David P. Madio, and H. Michael Gach. Transforming NMR data despite missing points. *J. Magn. Reson.*, 139(1):18–25, 1999.

[33] J. I. Jackson, C. H. Meyer, D. G. Nishimura, and A. Macovski. Selection of a convolution function for Fourier inversion using gridding (computerised tomography application). *IEEE Trans. Med. Imaging*, 10(3):473–478, 1991.

[34] P. J. Beatty, D. G. Nishimura, and J. M. Pauly. Rapid gridding reconstruction with a minimal oversampling ratio. *IEEE Trans. Med. Imaging*, 24(6):799–808, 2005.

[35] Klaas P. Pruessmann, Markus Weiger, Markus B. Scheidegger, and Peter Boesiger. SENSE: Sensitivity encoding for fast MRI. *Magn. Reson. Med.*, 42(5):952–962, 1999.

[36] Klaas P. Pruessmann, Markus Weiger, Peter Börnert, and Peter Boesiger. Advances in sensitivity encoding with arbitrary k-space trajectories. *Magn. Reson. Med.*, 46(4):638–651, 2001.

[37] Klaas P. Pruessmann. Encoding and reconstruction in parallel MRI. *NMR Biomed.*, 19(3):288–299, 2006.

[38] K. R. Brownstein and C. E. Tarr. Spin-lattice relaxation in a system governed by diffusion. *J. Magn. Reson.*, 26(1):17–24, 1977.

[39] Dean O. Kuethe, Natalie Adolphi, and Eiichi Fukushima. Short data-acquisition times improve projection images of lung tissue. *Magn. Reson. Med.*, 57(6):1058–1064, 2007.

[40] David M. Grodzki, Peter M. Jakob, and Bjoern Heismann. Ultrashort echo time imaging using pointwise encoding time reduction with radial acquisition (PETRA). *Magn. Reson. Med.*, 67(2):510–518, 2012.

[41] R. Adam Horch, Ken Wilkens, Daniel F. Gochberg, and Mark D. Does. RF coil considerations for short-T2 MRI. *Magn. Reson. Med.*, 64(6):1652–1657, 2010.

[42] Joel P. Felmlee and Richard L. Ehman. Spatial presaturation: A method for suppressing flow artifacts and improving depiction of vascular anatomy in MR imaging. *Radiology*, 164(2):559–564, 1987.

[43] Nobuyuki Otsu. A threshold selection method from gray-level histograms. *IEEE Trans. Syst., Man, Cybern.*, 9(1):62–66, 1979.

[44] Wolfgang Dreher, Ingo Bardenhagen, Li Huang, and Marcus Bäumer. On the suppression of background signals originating from NMR hardware components. Application to zero echo time imaging and relaxation time analysis. *Magn. Reson. Imaging*, 34(3):264–270, 2016.

[45] Li Huang and Wolfgang Dreher. Characterizing macroscopic mass transport in porous media by zero echo time MRI. In *Proceedings of 13th International Conference on Magnetic Resonance Microscopy: Materials, Molecular Processes and Engineering*, Munich, Germany, 2nd - 6th August 2015. P097.

[46] Emmanuel J. Candès, J. Romberg, and Terence Tao. Robust uncertainty principles: Exact signal reconstruction from highly incomplete frequency information. *IEEE Trans. Inf. Theory*, 52(2):489–509, 2006.

[47] M. Lustig, D. L. Donoho, J. M. Santos, and J. M. Pauly. Compressed Sensing MRI. *IEEE Signal Process. Mag.*, 25(2):72–82, 2008.

[48] Kuan-Mu Yao, Mohammad T. Habibian, and Charles R. O'Melia. Water and waste water filtration. Concepts and applications. *Environ. Sci. Technol.*, 5(11):1105–1112, 1971.

[49] Kennth J. Ives, editor. *The Scientific Basis of Filtration: Proceedings of the NATO Advanced Study Institute on the Scientific Basis of Filtration*, volume 2 of *NATO Science Series E Applied Sciences*, Cambridge, UK, 2nd - 20th July 1973. Noordhoff International Publishing.

[50] Laura M. McDowell-Boyer, James R. Hunt, and Nicholas Sitar. Particle transport through porous media. *Water Resour. Res.*, 22(13):1901–1921, 1986.

[51] Kenneth S. Sutherland and George Chase. *Filters and Filtration Handbook*. Elsevier Science, 5th edition, 2008.

[52] André B. de Haan and Hans Bosch. *Industrial Separation Processes: Fundamentals*. De Gruyter Textbook. De Gruyter, 2013.

[53] F. A. H. Al-Abduwani, R. Farajzadeh, W. M. G. T. van den Broek, P. K. Currie, and P. L. J. Zitha. Filtration of micron-sized particles in granular media revealed by x-ray computed tomography. *Rev. Sci. Instrum.*, 76(10), 2005.

[54] Xiqing Li, Chen-Luh Lin, Jan D. Miller, and William P. Johnson. Pore-scale observation of microsphere deposition at grain-to-grain contacts

over assemblage-scale porous media domains using X-ray microtomography. *Environ. Sci. Technol.*, 40(12):3762–3768, 2006.

[55] Jean-François Gaillard, Cheng Chen, Susa H. Stonedahl, Boris L. T. Lau, Denis T. Keane, and Aaron I. Packman. Imaging of colloidal deposits in granular porous media by X-ray difference micro-tomography. *Geophys. Res. Lett.*, 34(18):L18404, 2007.

[56] Cheng Chen, Boris L. T. Lau, Jean-François Gaillard, and Aaron I. Packman. Temporal evolution of pore geometry, fluid flow, and solute transport resulting from colloid deposition. *Water Resour. Res.*, 45(6):W06416, 2009.

[57] Xiqing Li, Zhelong Li, and Dongxiao Zhang. Role of low flow and backward flow zones on colloid transport in pore structures derived from real porous media. *Environ. Sci. Technol.*, 44(13):4936–4942, 2010.

[58] Wei Long, Haiou Huang, Jasmine Serlemitsos, Elizabeth Liu, Allen H. Reed, and Markus Hilpert. Pore-scale study of the collector efficiency of nanoparticles in packings of nonspherical collectors. *Colloids Surf., A*, 358(1-3):163–171, 2010.

[59] Zhelong Li, Dongxiao Zhang, and Xiqing Li. Tracking colloid transport in real pore structures: Comparisons with correlation equations and experimental observations. *Water Resour. Res.*, 48(5):W05533, 2012.

[60] Anja Waske, Michael Heiland, and Stefan Odenbach. Local position of colloid clusters in a packed bed of spheres. *Chem. Eng. Sci.*, 76:192–198, 2012.

[61] Stefan Günther and Stefan Odenbach. A method for image decomposition and particle quantification in multiphase systems. *Transp. Porous Media*, 112(1):105–116, 2016.

[62] Conrad J. Dirckx, Simon A. Clark, Laurance D. Hall, Brian Antalek, Joe Tooma, J. Michael Hewitt, and Ken Kawaoka. Magnetic resonance imaging of the filtration process. *AIChE J.*, 46(1):6–14, 2000.

[63] F. Heese, J. Acosta-Cabronero, P. Robson, and Laurance D. Hall. Measurement of particle separation by magnetic resonance imaging. *IEEE Sens. J.*, 5(2):268–272, 2005.

[64] Steffen Buetehorn, Lavinia Utiu, Markus Küppers, Bernhard Blümich, Thomas Wintgens, Matthias Wessling, and Thomas Melin. NMR imaging of local cumulative permeate flux and local cake growth in submerged microfiltration processes. *J. Membr. Sci.*, 371(1-2):52–64, 2011.

[65] Christopher J. Elkins and Marcus T. Alley. Magnetic resonance velocimetry: applications of magnetic resonance imaging in the measurement of fluid motion. *Exp. Fluids*, 43(6):823–858, 2007.

[66] Lynn F. Gladden and Andrew J. Sederman. Recent advances in Flow MRI. *J. Magn. Reson.*, 229:2–11, 2013.

[67] Paul T. Callaghan, C. D. Eccles, and Y. Xia. NMR microscopy of dynamic displacements: k-space and q-space imaging. *J. Phys. E: Sci. Instrum.*, 21(8):820, 1988.

[68] Paul R. Moran. A flow velocity zeugmatographic interlace for NMR imaging in humans. *Magn. Reson. Imaging*, 1(4):197–203, 1982.

[69] D. J. Bryant, J. A. Payne, D. N. Firmin, and D. B. Longmore. Measurement of flow with NMR imaging using a gradient pulse and phase difference technique. *J. Comput. Assist. Tomogr.*, 8(4):588–593, 1984.

[70] Paul R. Moran, R. A. Moran, and N. Karstaedt. Verification and evaluation of internal flow and motion. True magnetic resonance imaging by the phase gradient modulation method. *Radiology*, 154(2):433–441, 1985.

[71] Thomas E. Conturo and Gregory D. Smith. Signal-to-noise in phase angle reconstruction: Dynamic range extension using phase reference offsets. *Magn. Reson. Med.*, 15(3):420–437, 1990.

[72] Matt A. Bernstein and Yoshikazu Ikezaki. Comparison of phase-difference and complex-difference processing in phase-contrast MR angiography. *J. Magn. Reson. Imaging*, 1(6):725–729, 1991.

[73] Norbert J. Pelc, F. G. Sommer, K. C. Li, T. J. Brosnan, R. J. Herfkens, and D. R. Enzmann. Quantitative magnetic resonance flow imaging. *Magn. Reson. Q.*, 10(3):125–147, 1994.

[74] Jürgen Hennig, A. Nauerth, and H. Friedburg. RARE imaging: A fast imaging method for clinical MR. *Magn. Reson. Med.*, 3(6):823–833, 1986.

[75] T. W. J. Scheenen, D. van Dusschoten, P. A. de Jager, and H. van As. Microscopic displacement imaging with pulsed field gradient turbo spinecho NMR. *J. Magn. Reson.*, 142(2):207–215, 2000.

[76] T. W. J. Scheenen, F. J. Vergeldt, C. W. Windt, P. A. de Jager, and H. van As. Microscopic imaging of slow flow and diffusion: A pulsed field gradient stimulated echo sequence combined with turbo spin echo imaging. *J. Magn. Reson.*, 151(1):94–100, 2001.

[77] Andrew J. Sederman, Mick D. Mantle, and Lynn F. Gladden. Single excitation multiple image RARE (SEMI-RARE): Ultra-fast imaging of static and flowing systems. *J. Magn. Reson.*, 161(1):15–24, 2003.

[78] Federico Casanova, J. Perlo, Bernhard Blümich, and K. Kremer. Multi-echo imaging in highly inhomogeneous magnetic fields. *J. Magn. Reson.*, 166(1):76–81, 2004.

[79] Andrew J. Sederman, Mick D. Mantle, Craig Buckley, and Lynn F. Gladden. MRI technique for measurement of velocity vectors, acceleration, and autocorrelation functions in turbulent flow. *J. Magn. Reson.*, 166(2):182–189, 2004.

[80] Petrik Galvosas and Paul T. Callaghan. Fast magnetic resonance imaging and velocimetry for liquids under high flow rates. *J. Magn. Reson.*, 181(1):119–125, 2006.

[81] S. Ahola, J. Perlo, Federico Casanova, Siegfried Stapf, and Bernhard Blümich. Multiecho sequence for velocity imaging in inhomogeneous rf fields. *J. Magn. Reson.*, 182(1):143–151, 2006.

[82] Andrea Amar, Bernhard Blümich, and Federico Casanova. Rapid multiphase flow dynamics mapped by single-shot MRI velocimetry. *ChemPhysChem*, 11(12):2630–2638, 2010.

[83] Stefan Kuczera and Petrik Galvosas. Advances and artefact suppression in RARE-velocimetry for flow with curved streamlines. *J. Magn. Reson.*, 259:135–145, 2015.

[84] Matsyendra Nath Shukla, Antoine Vallatos, Vernon R. Phoenix, and William M. Holmes. Accurate phase-shift velocimetry in rock. *J. Magn. Reson.*, 267:43–53, 2016.

[85] Natascha Spindler, Petrik Galvosas, Andreas Pohlmeier, and Harry Vereecken. NMR velocimetry with 13-interval stimulated echo multi-slice imaging in natural porous media under low flow rates. *J. Magn. Reson.*, 212(1):216–223, 2011.

[86] P. Jehenson, M. Westphal, and N. Schuff. Analytical method for the compensation of eddy-current effects induced by pulsed magnetic field gradients in NMR systems. *J. Magn. Reson.*, 90(2):264–278, 1990.

[87] Arvind Caprihan, S. A. Altobelli, and E. Benitez-Read. Flow-velocity imaging from linear regression of phase images with techniques for reducing eddy-current effects. *J. Magn. Reson.*, 90(1):71–89, 1990.

[88] Matt A. Bernstein, Xiaohong Joe Zhou, Jason A. Polzin, Kevin F. King, Alexander Ganin, Norbert J. Pelc, and Gary H. Glover. Concomitant gradient terms in phase contrast MR: Analysis and correction. *Magn. Reson. Med.*, 39(2):300–308, 1998.

[89] Marvin A. Schofield and Yimei Zhu. Fast phase unwrapping algorithm for interferometric applications. *Opt. Lett.*, 28(14):1194–1196, 2003.

[90] Hussein S. Abdul-Rahamn, Munther A. Gdeisat, David R. Burton, Michael J. Lalor, Francis Lilley, and Christopher J. Moore. Fast and robust three-dimensional best path phase unwrapping algorithm. *Appl. Opt.*, 46(26):6623–6635, 2007.

[91] Mark Jenkinson. Fast, automated, N-dimensional phase-unwrapping algorithm. *Magn. Reson. Med.*, 49(1):193–197, 2003.

[92] E. K. Insko and L. Bolinger. Mapping of the radiofrequency field. *J. Magn. Reson., Ser. A*, 103(1):82–85, 1993.

[93] Natalia Shevchenko, Stefan Boden, Sven Eckert, Dmitry Borin, Michael Heinze, and Stefan Odenbach. Application of X-ray radioscopic methods for characterization of two-phase phenomena and solidification processes in metallic melts. *The European Physical Journal Special Topics*, 220(1):63–77, 2013.

[94] Vladimir Vezhnevets and Vadim Konouchine. GrowCut - Interactive multi-label N-D image segmentation by cellular automata. In *Proceedings of 15th GraphiCon*, pages 150–156, Novosibirsk, Russia, 20th - 24th June 2005.

[95] Charles L. Dumoulin, Steven P. Souza, Robert D. Darrow, Norbert J. Pelc, William J. Adams, and Stephen A. Ash. Simultaneous acquisition of phase-contrast angiograms and stationary-tissue images with Hadamard encoding of flow-induced phase shifts. *J. Magn. Reson. Imaging*, 1(4):399–404, 1991.

[96] Norbert J. Pelc, Matt A. Bernstein, Ann Shimakawa, and Gary H. Glover. Encoding strategies for three-direction phase-contrast MR imaging of flow. *J. Magn. Reson. Imaging*, 1(4):405–413, 1991.

[97] G. Shiko, Andrew J. Sederman, and Lynn F. Gladden. MRI technique for the snapshot imaging of quantitative velocity maps using RARE. *J. Magn. Reson.*, 216:183–191, 2012.

[98] Michael Adam, Stella Kocanis, Tobias Fey, Michaela Wilhelm, and Georg Grathwohl. Hierarchically ordered foams derived from polysiloxanes with catalytically active coatings. *J. Eur. Ceram. Soc.*, 34(7):1715–1725, 2014.

[99] Li Huang, Gerd Mikolajczyk, Ekkehard Küstermann, Michaela Wilhelm, Stefan Odenbach, and Wolfgang Dreher. Adapted MR velocimetry of slow liquid flow in porous media. *J. Magn. Reson.*, 276:103–112, 2017.

[100] Igor V. Koptyug, Stephen A. Altobelli, Eiichi Fukushima, Anatoly V. Matveev, and Renad Z. Sagdeev. Thermally polarized 1H NMR microimaging studies of liquid and gas flow in monolithic catalysts. *J. Magn. Reson.*, 147(1):36–42, 2000.

[101] Benedict Newling. Gas flow measurements by NMR. *Prog. Nucl. Magn. Reson. Spectrosc.*, 52(1):31–48, 2008.

[102] Alfred Kastler. Quelques suggestions concernant la production optique et la détection optique d'une inégalité de population des niveaux de quantifigation spatiale des atomes. Application à l'expérience de Stern et Gerlach et à la résonance magnétique. *J. Phys. Radium*, 11(6):255–265, 1950.

[103] M. S. Albert, Gordon D. Cates, B. Driehuys, William Happer, Brian Saam, C. S. Jr. Spinger, and A. Wishnia. Biological magnetic resonance imaging using laser-polarized 129Xe. *Nature*, 370(6486):199–201, 1994.

[104] Hunter Middleton, Robert D. Black, Brian Saam, Gordon D. Cates, Gary P. Cofer, Robert Guenther, William Happer, Lawrence W. Hedlund, G. Alan Johnson, Kim Juvan, and John Swartz. MR imaging with hyperpolarized 3He gas. *Magn. Reson. Med.*, 33(2):271–275, 1995.

[105] Thad G. Walker and William Happer. Spin-exchange optical pumping of noble-gas nuclei. *Rev. Mod. Phys.*, 69(2):629–642, 1997.

[106] Galina E. Pavlovskaya, Zackary I. Cleveland, Karl F. Stupic, Randall J. Basaraba, and Thomas Meersmann. Hyperpolarized krypton-83 as a contrast agent for magnetic resonance imaging. *Proc. Natl. Acad. Sci. U. S. A.*, 102(51):18275–18279, 2005.

[107] David M. L. Lilburn, Galina E. Pavlovskaya, and Thomas Meersmann. Perspectives of hyperpolarized noble gas MRI beyond 3He. *J. Magn. Reson.*, 229:173–186, 2013.

[108] Danila A. Barskiy, Aaron M. Coffey, Panayiotis Nikolaou, Dmitry M. Mikhaylov, Boyd M. Goodson, Rosa T. Branca, George J. Lu, Mikhail G. Shapiro, Ville-Veikko Telkki, Vladimir V. Zhivonitko, Igor V. Koptyug, Oleg G. Salnikov, Kirill V. Kovtunov, Valerii I. Bukhtiyarov, Matthew S. Rosen, Michael J. Barlow, Shahideh Safavi, Ian P. Hall, Leif Schrder, and Eduard Y. Chekmenev. NMR hyperpolarization techniques of gases. *Chem. - Eur. J.*, 23(4):725–751, 2017.

[109] Igor V. Koptyug, Ludmila Yu. Ilyina, Anatoly V. Matveev, Renad Z. Sagdeev, Valentin N. Parmon, and Stephen A. Altobelli. Liquid and gas flow and related phenomena in monolithic catalysts studied by 1H NMR microimaging. *Catal. Today*, 69(1-4):385–392, 2001.

[110] Igor V. Koptyug, Anatoly V. Matveev, and Renad Z. Sagdeev. NMR studies of hydrocarbon gas flow and dispersion. *Appl. Magn. Reson.*, 22(2):187–200, 2002.

[111] Benedict Newling, Christopher C. Poirier, Yang Zhi, James A. Rioux, Andrew J. Coristine, Dale Roach, and Bruce J. Balcom. Velocity imaging of highly turbulent gas flow. *Phys. Rev. Lett.*, 93(15):154503, 2004.

[112] Mark H. Sankey, Daniel J. Holland, Andrew J. Sederman, and Lynn F. Gladden. Magnetic resonance velocity imaging of liquid and gas two-phase flow in packed beds. *J. Magn. Reson.*, 196(2):142–148, 2009.

[113] Lynn F. Gladden, Fernando J. R. Abegão, Christopher P. Dunckley, Daniel J. Holland, Mark H. Sankey, and Andrew J. Sederman. MRI:

Operando measurements of temperature, hydrodynamics and local reaction rate in a heterogeneous catalytic reactor. *Catal. Today*, 155(3-4):157–163, 2010.

[114] Nicholas P. Ramskill, Andrew P. E. York, Andrew J. Sederman, and Lynn F. Gladden. Magnetic resonance velocity imaging of gas flow in a diesel particulate filter. *Chem. Eng. Sci.*, 158:490–499, 2017.

[115] Jürgen Ulpts, Wolfgang Dreher, Miriam Klink, and Jorg Thöming. NMR imaging of gas phase hydrogenation in a packed bed flow reactor. *Appl. Catal., A*, 502:340–349, 2015.

[116] Jürgen Ulpts, Wolfgang Dreher, Lars Kiewidt, Miriam Schubert, and Jorg Thöming. In situ analysis of gas phase reaction processes within monolithic catalyst supports by applying NMR imaging methods. *Catal. Today*, 273:91–98, 2016.

[117] M. Cowie and Harry Watts. Diffusion of methane and chloromethanes in air. *Can. J. Chem.*, 49(1):74–77, 1971.

[118] T. R. Marrero and E. A. Mason. Gaseous diffusion coefficients. *J. Phys. Chem. Ref. Data*, 1(1):3–118, 1972.

[119] Richard R. Ernst and W. A. Anderson. Application of Fourier transform spectroscopy to magnetic resonance. *Rev. Sci. Instrum.*, 37(1):93–102, 1966.

[120] E. O. Stejskal and J. E. Tanner. Spin diffusion measurements: Spin echoes in the presence of time-dependent field gradient. *J. Chem. Phys.*, 42(1):288–292, 1965.

Glossary

1D / 2D / 3D = One- / Two- / Three-Dimensional
CP / CPMG = Carr-Purcell / Carr-Purcell-Meiboom-Gill
CFD = Computational Fluid Dynamics
FID = Free Induction Decay
GRE = Gradient Recalled Echo
NMR / MRI = Nuclear Magnetic Resonance / Magnetic Resonance Imaging
DW-MRI / DT-MRI = Diffusion Weighted / Diffusion Tensor MRI
PC-MRI = Phase Contrast MRI
OVS = Outer Volume Suppression
RARE = Rapid Acquisition with Relaxation Enhancement
RF = Radio-Frequency
PTFE = PolyTetraFluoroEthylene
SE / STE = Spin Echo / STimulated Echo
SNR = Signal-to-Noise Ratio
STD = STandard Deviation
UTE / ZTE = Ultrashort / Zero Echo Time
XMT = X-ray Micro-Tomography

b	b value used for describing NMR signal decay by diffusion $[s/m^2]$
$\boldsymbol{B}_0$ / B_0	longitudinal static magnetic field / its magnitude $[T]$
$\boldsymbol{B}_1$ / B_1	transversal oscillating magnetic field / its magnitude $[T]$
BW $(\delta\nu)$ / $\Delta\nu$	BandWidth $[Hz]$ / frequency shift $[Hz]$
CS (σ)	Chemical Shift
D	diffusion coefficient $[m^2/s]$
E	magnetic energy $[eV]$
FA (α) / α_E	Flip Angle / Ernst Angle
FOV	Field-Of-View $[m]$
$\boldsymbol{G}$ / G	magnetic field gradient / its magnitude $[T/m]$
G_{PE}	phase encoding gradient $[T/m]$
G_r	read gradient $[T/m]$
G_{SS}	slice selection gradient $[T/m]$
G_{VE}	velocity encoding gradient $[T/m]$

γ	gyromagnetic ratio ($2\pi \cdot 42.577\, MHz/T$ for ^1H nucleus)
$\hbar$	reduced Planck constant ($6.5821 \cdot 10^{-16}\, eV \cdot s$)
I	nuclear spin quantum number
$\boldsymbol{k}$ / k	k-space vector / its magnitude [m^{-1}]
k_B	Boltzmann constant ($8.6173 \cdot 10^{-5}\, eV/K$)
$\boldsymbol{L}$ / L	angular momentum of nuclear spin / its magnitude [$eV \cdot s$]
L_z	azimuthal angular momentum of nuclear spin [$eV \cdot s$]
$\boldsymbol{M}$	(macroscopic) magnetization
M_0	magnitude of magnetization in thermal equilibrium [eV/T]
M_{xy} / M_z	transversal / longitudinal component of magnetization [eV/T]
m	magnetic quantum number
$\boldsymbol{\mu}$	magnetic moment [eV/T]
N	matrix size
N_- / N_+	spin population of higher / lower energy level
NA	Number of Averages
N_{PE}	number of phase encoding steps
N_{RARE}	RARE factor
N_{slice}	number of slices or secondary phase encoding steps
N_{VE}	number of velocity encoding steps
ν_0 / ω_0	resonance frequency [Hz] / angular resonance frequency [Rad/s]
P	propagator [m^{-1}]
$\boldsymbol{q}$ / q	q-space vector / its magnitude [m^{-1}]
$\boldsymbol{r}$ / r	real space vector / its magnitude [m]
d_{SS} / r_{SS}	slice thickness / position [m]
T	temperature [K]
T_1	spin-lattice relaxation time [s]
T_2 / T_2^*	spin-spin relaxation time [s] / effective transversal relaxation time [s]
TE	Echo Time [s]
TR	Repetition Time [s]
t_d	dwell time [s]
t_{dead}	dead time [s]
t_Δ	delay between velocity encoding gradients [s]
t_δ	duration of velocity encoding gradient [s]
t_g	gradient duration [s]
t_p	pulse duration [s]
t_{total}	total measurement time
θ	pulse phase
$\boldsymbol{v}$	velocity [m/s]
$VENC$	Velocity ENCoding range [m/s]
VFR	Volumetric Flow Rate [m^3/s]
x, y, z / x', y', z'	Cartesian coordinates in the laboratory / rotating frame of reference [m]

Acknowledgement

First of all, I would like to sincerely give great thanks to my primary supervisor, Mr. PD Dr. Wolfgang Dreher. Wolfgang has not only supervised my PhD training within research work for the project "Nuclear magnetic Resonance methods for characterization of mass transport in porous materials" in his group, but also always guided my research work as well as the scientific output like journal articles and thesis, taught me the life in academia, and helped me through all kinds of difficulties. He is an excellent tutor with kindness, patience, and wisdom.

For all the funs in the group "In-vivo-MR", Faculty 02, University of Bremen, I also would like to thank all the colleagues: the senior scientists, Mr. Dr. Ekkehard Küstermann and Mr. Dr. Peter Erhard; the PhD students, Ms. Felizitas Wermter and Mr. Mojtaba Mirdrikvand; the secretary, Ms. Marion Schilling; and all other BSc and MSc students in the group. Moreover, I sincerely appreciate their valuable support for my work, particularly useful suggestions from Ekkehard, Peter, and Mojtaba for oral talks and written contributions, knowledge transfer and trouble shooting by Ekkehard for experiments.

Thanks to the fact that my PhD project is within the Graduate School / Research Training Group "MIMENIMA" ("Micro-, meso-, and macroporous non-metallic materlais: Fundamentals and Applications") funded by the German Research Foundation, I have gained practical experiences in such a multi-cultural and interdisciplinary research cluster. The experiences include: collaborations; communications, particularly with my secondary supervisor as well as an examiner in my defense, Mr. Prof. Dr. Marcus Bäumer; financially supported scientific activities, particularly workshops, courses, and the research visit abroad. Though some collaborations have not reached complete results, special thanks are still given here to all collaborators: Mr. Gerd Mikolajczyk, Ms. Gesa Hollermann, Mr. Jürgen Ulpts, Mr. Lars Kiewidt, Mr. Dr. Benjamin Besser, Ms. Laura Luhede, Mr. Prof. Dr. Jorg Thöming, Mr. Prof. Dr. Stefan Odenbach, Ms. Dr. Michaela Wilhelm, Mr. Prof. Dr. Kurosch Rezwan, Ms. Dr. Laura Treccani, Mr. Dr. Stephen

Kroll, and Mr. Prof. Dr. Udo Fritsching.

Except for the above colleagues, I devote my special thanks to Mr. Prof. Dr. Matthias Günther as one of the two reviewers of my thesis. Besides, I would like to thank Mr. Prof. Dr. Peter Spiteller and Ms. Marilena Hnida for being part of my Examination Board.

There are still many persons in University of Bremen deserving my gratitudes, such as the colleagues in production workshops for construction of samples and coils. Though unable to figure all of them out, I still express my grateful attitudes here.

Finally, I would like to write down the great thanks to my family including my parents, my parents-in-law, and my wife, Lai Peng, most importantly. Lai is always accompanying me, sharing happiness and pain with me, encouraging me, and spurring me. Especially, I will never forget the hard time we have gone through together.

Bremen is the place where I started the life as a researcher as well as a husband. Thank God for the nearly four years I have spent here. I do not know whether I will have the chance to live in Bremen or other places in Germany again, but I will remember the life here forever.